RICE UNIVERSITY

# Coated Carbon Nanotubes and Carbon Fibers: Synthesis and Applications

by

**Huma Rahim Jafry**

A THESIS SUBMITTED
IN PARTIAL FULFILLMENT OF THE
REQUIREMENTS FOR THE DEGREE

**Doctor of Philosophy**

APPROVED, THESIS COMMITTEE:

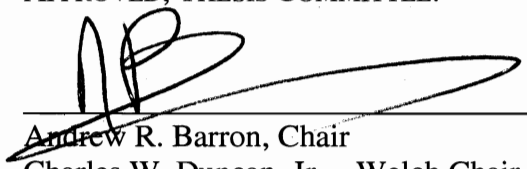

Andrew R. Barron, Chair
Charles W. Duncan, Jr. – Welch Chair of Chemistry and Professor of Materials Science

Kenton H. Whitmire
Professor of Chemistry
Associate Dean for Academic Affairs for Weiss School of Natural Science

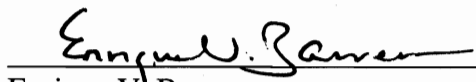

Enrique V. Barrera
Professor of Mechanical Engineering and Material Science

HOUSTON, TEXAS
SEPTEMBER 2010

**Abstract**

Coated Carbon Nanotubes and Carbon Fibers: Synthesis and Applications

by

Huma R. Jafry

Carbon nanotubes have been of great interest given their unique electronic and mechanical properties. Scholars have focused on the addition of carbon nanotubes to various matrices in order to develop novel materials. These new hybrid materials would combine the properties of both the nanotubes and the matrix of choice, which can both enhance the mechanical and electronic properties of the matrix material, and allow for the matrix to be used for other applications. In order to take advantage of the properties of the nanotubes, it is vital for them to be well dispersed in a solution or matrix as individual tubes, rather than as bundles. Additionally, it is cost effective to have individually dispersed tubes in a matrix. In order to individually disperse the tubes in the matrix, they can be pre-treated or functionalized via both covalent and non covalent processes. Subsequent to functionalization, the nanotubes can be coated with the matrix material or other metal compounds. This can help with the dispersion and interface interaction with the matrix material, or create materials with novel properties.

This thesis focuses on conditions of growing various metal compounds or metal oxides on nanotubes using chemical bath deposition (CBD) and liquid phase deposition (LPD) methods. CBD and LPD use aqueous mediums for growth and deposition of compounds, which makes it both environmentally friendly and cost effective. Different pre-treatments are first employed on the nanotubes in order for them to be both well dispersed in solution and provide nucleation sites for the deposition and growth of various metal and metal oxides on the surface of the nanotubes. Once an ideal deposition is achieved, applications of the coated tubes are studied, tested and discussed.

"...Hazrat Ali emphasized that '*No honour is like knowledge...No belief is like modesty and patience, no attainment is like humility, no power is like forbearance, and no support is more reliable than consultation.*' Notice that the virtues endorsed by Hazrat Ali are qualities which subordinate the self and emphasize others – modesty, patience, humility, forbearance and consultation. What he thus is telling us, is that we find knowledge best by admitting first what it is we do not know, and by opening our minds to what others can teach us.... But accessing knowledge is only the first step. The second step – the application of knowledge, is also demanding. Knowledge, after all, can be used well or poorly – for good or evil purposes. Once we have acquired knowledge, it is important that the ethical guidelines of faith be invoked, helping us apply what we have learned to the highest possible ends. And it is also important that those ends be related to the practical needs of our peoples." – *His Highness the Aga Khan IV*

**Acknowledgements**

During this journey of graduate school, I have met many people who have influenced me in ways which have allowed me to grow both professionally and personally. These years at Rice have been one of the most valuable years for me, and I am very glad to have had the opportunity to be under the guidance of my advisor, Dr. Andrew Barron. I would like to take this opportunity to thank him for providing me with all the guidance, support, and encouragement throughout the years. He has fostered an environment in his lab which allows for independent thinking, creativity, hard work, career building, and lots of fun for his group members, especially during group lunches, his home parties, and speed driving on the race track in his new cars. Additionally, I would like to thank him for allowing me to work on certain independent ideas I had, and help me turn those ideas into projects and eventually into a successful venture. I certainly could not have accomplished all this without him.

I would like to thank all my friends and co-workers at Rice for making this into a wonderful journey. In particular, I would like to thank Dr. Robin Anderson, Dr. Elizabeth Whitsitt, and Dr. Ramon Colorado for helping me get started on experiments, answering my questions, and initially running the SEM instrument for me. I would also like to thank the five group members who started the same year as myself, Amanda, Nadjmeh, Chris C, Chris H, and Johnathan, and made it a fun filled experience. Additionally, thanks to the SEA instrument managers, Dr. Bo Chen, Dr. Whenhua Gua, Dr. Larry Alemany, and Dr. Angelo Benedetto for training me and answering the innumerable questions I had regarding data results and the various instruments I used over the years.

Finally, I would like to thank my family for being my backbone and support system during these years. My husband and best friend Irfan Lalani, who has had to patiently put up with a wife in school, and has constantly encouraged me to pursue excellence in my career. Additionally, I would also like to thank him for the initial X-ray

tests he ran on my samples at his work. My deepest gratitude and thanks to my parents, Hamida and Rahim Jafry, who always gave me the moral support and encouragement to face challenging situations at hand, work hard, and to give my best at every endeavor I undertook. Additionally, to all the Jafry siblings and their families, Adil, Sarwat, Rahil, Saleena, Shehrezade and Shehryar for their exceptional support.

Finally, Irfan and I along with my family are looking forward our new bundle of joy, my first baby, due in November 2010.

## Table of Contents

**Introduction** 1

**Chapter 1. Silica Coatings on Vapor Grown Carbon Fibers**

Introduction 13

Results and Discussion 18

Conclusions 30

Experimental 31

References 33

**Chapter 2. Effect of Functionalized Nanomaterials on the Rheology of Borate Cross-Linked Guar Gum**

Introduction 36

Results and Discussion 38

Conclusions 49

Experimental 50

References 51

**Chapter 3. Role of Silica in Titania Coatings and Photocatalysis**

Introduction 53

Results and Discussion 55

Conclusions 79

Experimental 80

References 83

**Chapter 4. Coating Carbon Nanotubes with Lead Sulfide and Bismuth Sulfide**

Introduction 85

Results and Discussion 88

Conclusions 104

Experimental 105

References 108

**Overall Conclusions** 111

**Appendix. A. List of Publications** 113

## List of Figures

### Introduction

**Figure I.1.** Schematic illustration of silica LPD film deposition mechanism. 2

**Figure I.2.** Cartoon showing the proposed interaction of surfactants sodium dodecylbenzene sulfomate (NaDDBS) and sodium dodecyl sulfate (SDS) with nanotubes. 4

**Figure I.3.** Gold nanoparticle coatings on CNT treated with nitric acid, showing minor changes in procedure which alter the nanoparticle sizes. 7

**Figure I.4.** SEM (a) and TEM (b) image of $MoO_2$ nanorods obtained after the removal of CNT which is used as a scaffold. 8

**Figure I.5.** Schematic illustration of the addition of molten metal inside the CNT. 8

### Chapter 1

**Figure 1.1.** IR spectra showing the presence of Si-O-Si present around the VGCFs. 19

**Figure 1.2.** Raman spectra (using 532 nm excitation) of silica coated VGCFs showing the presence of VGCFs and the F-containing silica. Band assignments are provided. 19

**Figure 1.3.** SEM image of Type II treated VGCFs (Pyrograph III) treated with silica LPD solution without any acid pretreatment of the VGCFs showing the presence of uncoated VGCFs and silica particles. 20

**Figure 1.4.** SEM image of Type II treated VGCFs (Pyrograph III) coated with silica for (a) 4 hours, (b) 8 hours, (c) 20 hours, and (d) 24 hours. 21

**Figure 1.5.** SEM image of Type II treated VGCFs (Pyrograph III) (a) before and (b) after silica LPD for 4 hours showing the presence of a 90-100 nm silica coating. 22

**Figure 1.6.** SEM image of VGCFs (Pyrograph III) in DTAB coated with silica for 4 hours, showing the presence of silica spheres resulting from the interaction of the silica LPD solutions with the DTAB micelles. 23

**Figure 1.7.** SEM image of Type I treated VGCFs (Pyrograph III) coated with silica for 4 hours. 26

**Figure 1.8.** SEM image of Type III acid treated VGCFs (Pyrograph III) coated with silica for 3 hours. 26

**Figure 1.9.** High resolution $C_{1S}$ XPS spectrum for Type II acid treated MER VGCFs showing the presence of different carbon species. 27

**Chapter 2**

**Figure 2.1.** The repeat unit of guaran, a naturally occurring polysaccharide, consisting of (1→4)-β-D-mannopyranosyl units with α-D-galactopyranosyl side chains attached to about every other mannose via (1→6) linkages. 37

**Figure 2.2.** Schematic representation of the conversion of VGCFs to $SiO_2$-VGCFs and ODS-$SiO_2$-VGCFs. 38

**Figure 2.3.** High resolution Si2p XPS of ODS-$SiO_2$-VGCF showing the presence of both silica (103.13 and 103.79 eV) and organosilane substituent (102.23 eV). 39

**Figure 2.4.** IR spectra of $SiO_2$-VGCF and ODS-$SiO_2$-VGCF showing the presence of aliphatic $\nu_{C\text{-}H}$ bands due to the octadecyl substituents. 39

**Figure 2.5.** Viscosity with respect to frequency for boric acid cross-linked guar gel (▫) in comparison with boric acid cross-linked guar gel with 1 wt% (compared to

guar) of unfunctionalized VGCFs (▪), $SiO_2$-VGCFs (▪), and ODS-$SiO_2$-VGCF (▪). All measurements were taken at pH = 8.6. 40

**Figure 2.6.** Viscosity with respect to frequency for boric acid cross-linked guar gel (▫) in comparison with boric acid cross-linked guar gel with 1 wt% (▪) and 2 wt% (▪) of ODS-$SiO_2$-VGCF. All measurements were taken at pH = 8.6. 41

**Figure 2.7.** Viscosity with respect to frequency at pH = 8.6 (a), 9.3 (b), and 10.3 (c) for boric acid cross-linked guar gel (▫) in comparison with boric acid cross-linked guar gel with 2 wt% of ODS-$SiO_2$-VGCF (▪). 42

**Figure 2.8.** Storage modulus with respect to frequency at pH 8.6 (a), 9.3 (b), and 10.3 (c) for boric acid cross-linked guar gel (▫) in comparison with boric acid cross-linked guar gel with 2 wt% of ODS-$SiO_2$-VGCF (▪). 44

**Figure 2.9.** Viscosity with respect to shear rate at pH 8.6 for boric acid cross-linked guar gel (▫) in comparison with boric acid cross-linked guar gel with 1 wt% of $SiO_2$-VGCF (▪) and ODS-$SiO_2$-VGCF (▪). 45

**Figure 2.10.** Viscosity with respect to shear rate at pH 8.6 for boric acid cross-linked guar

gel (▫) in comparison with boric acid cross-linked guar gel with 1 wt% of ODS-$SiO_2$-VGCF (▪) and 2 wt% ODS-$SiO_2$-VGCF (▪). 45

**Figure 2.11.** Viscosity with respect to forward and reverse shear rates at pH 9.3 (a) and 10.3 (b) for boric acid cross-linked guar gel (forward, ▫ and reverse, ×) in comparison with boric acid cross-linked guar gel with 2 wt% of ODS-$SiO_2$-VGCF (forward ▪ and reverse ×). 48

**Chapter 3**

**Figure 3.1** TEM image of (a) $TiO_2$-SWNT-PP-21 (scale = 50 nm) and (b) $TiO_2$-SWNT-PP-48 (scale = 0.1 μm). 56

**Figure 3.2.** TEM images of (a) $TiO_2$-SWNT-glass-21 (scale = 100 nm) and (b) $TiO_2$-SWNT-glass-10 (scale = 50 nm). 58

**Figure 3.3** TEM image of $TiO_2$-SWNT-$SiO_2$-21 (scale = 0.2 μm). 59

**Figure 3.4.** XRD showing the anatase (A) and rutile (R) phases commercial P25-$TiO_2$ (——) as compared to $TiO_2$-SWNT-PP-21 (——), $TiO_2$-SWNT-glass-21 (——), and $TiO_2$-SWNT-$SiO_2$-21 (——). 60

**Figure 3.5.** Chemical structure of Congo red dye. 61

**Figure 3.6.** Percent removal of Congo red after 1 hour dark stiring by P25-$TiO_2$, $TiO_2$-SWNTs-PP-21 (PP-21), $TiO_2$-SWNTs-PP-48 (PP-48), and $TiO_2$-SWNTs-glass-10 (glass-10) with a catalyst concentration of 500 mg/L and an initial dye concentration 250 mg/L. 62

**Figure 3.7.** Percent removal of Congo red after 1 hour dark stiring by P25-$TiO_2$, SWNTs, $TiO_2$-SWNTs-glass-10 (glass-10), and $TiO_2$-SWNTs-glass-21 (glass-21) with a catalyst concentration of 250 mg/L and an initial dye concentration 150 mg/L. 63

**Figure 3.8.** Normalized photocatalytic degradation of Congo red by $TiO_2$-SWNTs-PP-21 (■), $TiO_2$-SWNTs-PP-48 (■) and P25-$TiO_2$ (■). $C_0$ is the dye concentration after dark stirring. 64

**Figure 3.9.** Normalized photocatalytic degradation of Congo red by $TiO_2$-SWNTs-glass-10 (■), $TiO_2$-SWNTs-glass-21 (■), and P25-$TiO_2$ (■). $C_0$ is the dye concentration after dark stirring. 65

**Figure 3.10.** Normalized photocatalytic degradation of Congo red by a physical mixture of P25-$TiO_2$ with SWNTs (■) or

MWNTs (■) in comparison with P25-$TiO_2$ (■). $C_0$ is the dye concentration after dark stirring. 66

**Figure 3.11.** MS2 inactivation by untreated $TiO_2$(P25) (■, $R^2 = 0.935$) and treated by refluxing in toluene with silicone grease sealing the glass apparatus (▫, $R^2 = 0.971$). 67

**Figure 3.12.** MS2 inactivation by untreated $TiO_2$(P25) (■, $R^2 = 0.935$) and treated by refluxing in toluene with non-silicone (hydrocarbon-based) grease sealing the glass apparatus (▫, $R^2 = 0.917$). 68

**Figure 3.13.** Adsorptive removal/dark inactivation of MS2 by $TiO_2$(P25) (■), $TiO_2$(P25) refluxing in toluene with non-silicone grease (■), and $TiO_2$(P25)-$SiO_2$ formed by stirring (■) or refluxing (■). 69

**Figure 3.14.** Photocatalytic inactivation of MS2 by $TiO_2$(P25) (■, $R^2 = 0.935$), $TiO_2$(P25) refluxing in toluene with non-silicone grease (■, $R^2 = 0.917$), and $TiO_2$(P25)-$SiO_2$ formed by stirring (■, $R^2 = 0.907$) or refluxing (■, $R^2 = 0.970$). 70

**Figure 3.15.** TEM of $TiO_2$(P25) reacted with fumed silica with (a) stirring in comparison with (b) as-received P25 $TiO_2$. 73

**Figure 3.16.** O1s X-ray photoelectron spectrum for $TiO_2$(P25)-$SiO_2$(2.5%) formed by refluxing $TiO_2$(P25) in toluene in the presence of silica. 74

**Figure 3.17.** $^{29}$Si MAS NMR of $TiO_2$(P25)-$SiO_2$(5%). showing the presence of "$SiO_4$" coordination environment. 75

**Figure 3.18.** Photocatalytic inactivation of MS2 by $TiO_2$(P25)-$SiO_2$ formed by stirring (■, $R^2 = 0.907$) or refluxing (■, $R^2 = 0.970$) as compared to the values when run in the presence of methanol, a scavenger for hydroxyl free radical (□, $R^2 = 0.479$ and □, $R^2 = 0.571$, respectively). 77

**Figure 3.19.** UV-vis absorbance curves for $TiO_2$(P25) (—) and $TiO_2$(P25)-$SiO_2$ formed with 2.5% (—), 10% (—) and 20% (—) $SiO_2$, respectively. 78

**Chapter 4**

**Figure 4.1.** TEM images of plain VGCFs (a) and (b), and VGCFs treated with *in situ* method for the addition of Pb salts (c) and (d). 89

**Figure 4.2.** X-ray absorption by (a) VGCF treated with *in situ* method of adding Pb

salts (b) lead nitrate salts and (c) plain VGCFs. 90

**Figure 4.3.** SEM image showing spheres present on the outside of the VGCFs treated with *in situ* method for the addition of Pb salts. 90

**Figure 4.4.** XPS showing (a) plain VGCFs and (b) VGCFs treated with *in situ* method of adding Pb salts. 91

**Figure 4.5.** TEM image showing the presence of Pb salts on the outside walls of the MWNT. 92

**Figure 4.6.** X-ray absorption by (a) plain MWNTs and (b) MWNTs treated with *in situ* method for the addition of Pb salts. 92

**Figure 4.7.** TEM images showing the presence of Pb salts inside the VGCFs via the two step method. 93

**Figure 4.8.** TEM image of MWNT treated using two step method, showing the etching of the sidewalls and miniscule (if any) presence of Pb salts. 94

**Figure 4.9.** SEM image showing PbS coatings of MWNTs obtained using SDS. A "petal like" fused structure in between the MWNTs. 95

**Figure 4.10.** EDX showing the presence of Pb and S on MWNTs coated using SDS. 96

**Figure 4.11.** SEM image of SWNTs coated with PbS compounds with the aid of CTAB. 97

**Figure 4.12.** X-ray absorption by SWNTs in 2-step method using CTAB.for coating with PbS. 98

**Figure 4.13.** SEM image of acid treated VGCFs coated with PbS compounds: 2 hour reaction with high concentration of reactants (a), and 2 hour reaction with low concentration of reactants (b) and (c). 99

**Figure 4.14.** SEM image of acid treated VGCFs coated with PbS compounds: (a) 4 hour reaction with high concentration of reactants and (b) 4 hour reaction with low concentration of reactants. 100

**Figure 4.15.** XPS of acid treated VGCFs coated with Pb compounds for a sample with 2 hour reaction time with low concentration of reactants. 101

**Figure 4.16.** SEM image showing the coatings of VGCFs with $Bi_2S_3$ in the presence of SDS. 102

**Figure 4.17.** XPS of VGCFs coated with $Bi_2S_3$ using SDS, Bi4f and S2p peaks. 102

**Figure 4.18.** SEM image of acid treated VGCFs coated with $Bi_2S_3$. 103

**Figure 4.19.** XPS of acid treated VGCF coated with $Bi_2S_3$ with overlapping Bi4f and S2p peaks. 104

## List of Tables


**Chapter 1**

**Table 1.1.** Summary of coating experiments showing the affect of pre-treatment and deposition time on silica coatings of VGCFs. 23

**Table 1.2.** Atomic concentration of $C_{1s}$ and $O_{1s}$ obtained from XPS. 29

**Table 1.3.** Percentage area of functional groups in $C_{1s}$ spectra (%). 30

**Chapter 2**

**Table 2.1.** XPS spectra analysis of $SiO_2$-VGCF after reaction with boric acid. 41

**Chapter 3**

**Table 3.1** XPS analysis (%) for $TiO_2$-coated SWNTs. 59

**Table 3.2.** First order rate constants for MS2 inactivation [$Log(N/N_0) = -kt$]. 72

**Table 3.3** XPS analysis on $TiO_2$(P25) and $TiO_2$(P25) refluxed and stirred with fumed $SiO_2$. 74

**Table 3.4.** BET surface area measurements of $TiO_2$(P25) and $TiO_2$(P25)-$SiO_2$ powders. 76

**Table 3.5.** Band gap calculations based on UV-vis absorbance spectrum of $TiO_2$(P25) and $TiO_2$(P25)-$SiO_2$ powders. 79

## Abbreviations

| | |
|---|---|
| Bi | bismuth |
| $Bi_2S_3$ | bismuth sulfide |
| BET | Branauer Emmett Teller surface area analysis |
| $C_{60}$ | fullerene |
| CTAB | cetyl trimethylammonium bromide |
| CBD | chemical bath deposition |
| ºC | degrees centrigrade |
| $C_0$ | initial concentration |
| CNT | carbon nanotubes |
| cm | centimeters |
| Da | Dalton |
| DI water | deionized water |
| DTAB | dodecyl trimethyl ammonium bromide |
| eV | electron volt |
| EDX | energy-dispersive X-ray spectroscopy |
| EtOH | ethanol |
| GPa | giga Pascal |
| G' | storage modulus |
| G" | loss modulus |
| g | gram |
| HF | fluoric acid |
| hr | hour |
| $H_2SiF_6$ | hydrofluosilicic acid |
| $HO^{\cdot}$ | hydroxyl radical |
| IR | infrared spectroscopy |

| | |
|---|---|
| $\lambda$ | lamda, wavelength |
| L | liter |
| LPD | liquid phase deposition |
| m | meters |
| M | molar concentration |
| MeOH | methanol |
| $\mu$m | micrometers |
| mg | milligram |
| mL | milliliters |
| min | minutes |
| mol | moles |
| mmol | millimol |
| $M_w$ | molecular weight |
| MS2 | name of bacteriophage |
| MWNT | multi walled carbon nanotubes |
| nm | nanometers |
| NMR | nuclear magnetic resonance |
| ODS | octadecyltrichlosilane |
| ODS-$SiO_2$-VGCF | ocatdecyltrichlorosilane functionalized silica coated vapor grown carbon fibers |
| $\Omega$ | ohms |
| OH | hydroxyl |
| Pb | lead |
| PbS | lead sulfide |
| PP | polypropylene |
| ppm | parts per million |
| rad | radians |

| | |
|---|---|
| ROS | reactive oxygen species |
| rpm | revolutions per minute |
| SDBS | sodium dodecyl benzene sulfate |
| SDS | sodium dodecyl sulfate |
| SEM | scanning electron microscopy |
| s | second |
| $SiO_2$ | silica |
| $SiO_2$-VGCFs | silica coated vapor grown carbon fibers |
| SWNT | single walled carbon nanotubesl |
| TEM | transmission electron microscopy |
| TPa | terapascal |
| $TiO_2$ | titania, titanium dioxide |
| $TiO_2$(P25) | P25 titania nanoparticles |
| $TiO_2$-SWNT-PP | titania coated single walled nanotubes in a polypropylene beaker |
| $TiO_2$-SWNT-glass | titania coated single walled nanotubes in a polypropylene beaker |
| $TiO_2$-SWNT-$SiO_2$ | titania coated single walled nanotubes with fumed silica |
| UV | ultra violet radiation |
| VGCF | vapor grown carbon fibers |
| $W \cdot m^{-1} \cdot K^{-1}$ | watts per meter per Kelvin |
| wt. | weight or ratio of parts by mass |
| XPS | X-ray photoelectron spectroscopy |
| XRD | X-ray diffractometry |

# Introduction

Carbon nanotubes (CNTs) have received considerable amounts of attention since the discovery by Ijima.[1] The family of CNTs includes single walled carbon nanotubes (SWNTs), multi walled carbon nanotubes (MWNTs), and vapor grown carbon fibers (VGCFs). CNTs are cylindrical, extended fullerene structures of rolled up hexagonal carbon networks that are capped with pentagonal carbon rings.[2,3] Depending on the tube diameter and chirality, SWNTs exhibit metallic or semiconducting properties with enhanced mechanical properties. SWNTs have a tensile strength of 200 GPa, and a Young's modulus of 1 TPa, while the MWNTs have a Young's modulus of up to 950 GPa. VGCFs are of much larger diameters ranging from 100 – 300 nm, are between 3-10 μm in length, and have a Young's modulus of 88 - 240 GPa.[4,5,6] Given the unique electronic and high mechanical properties, research has been devoted to the addition of CNTs within polymers and ceramics, or decorating and filling them metals or metal compounds; this would allow for the development of a whole new class of materials at the nanoscale, with applications in many fields. The addition of small amounts of CNTs to ceramic powders has been shown to produce tougher ceramic materials,[7,8] by which the CNTs serve as sites for fracture energy dissipation through mechanisms such as crack deflection or CNT breakage/debonding.[8] For example, the addition of CNTs to a silicon carbide (SiC) composite showed an increase of 10% in the strength of the composite,[9] while the addition of SWNTs to an alumina composite increased the toughness of the ceramic by three times, as compared to that of pure alumina.[10] An and co-workers show the in-situ growth and coatings of CNTs within an alumina matrix. They synthesize the alumina-CNT powders by the catalytic decomposition of acetylene over an iron catalyst supported alumina powder, thereby, growing the CNTs within the alumina powders. After the CNT growth, the alumina-CNT powder is hot-pressed and tested. It is found

that the hardness of the alumina composite reaches its maximum when there is 4% of CNTs present.[11]

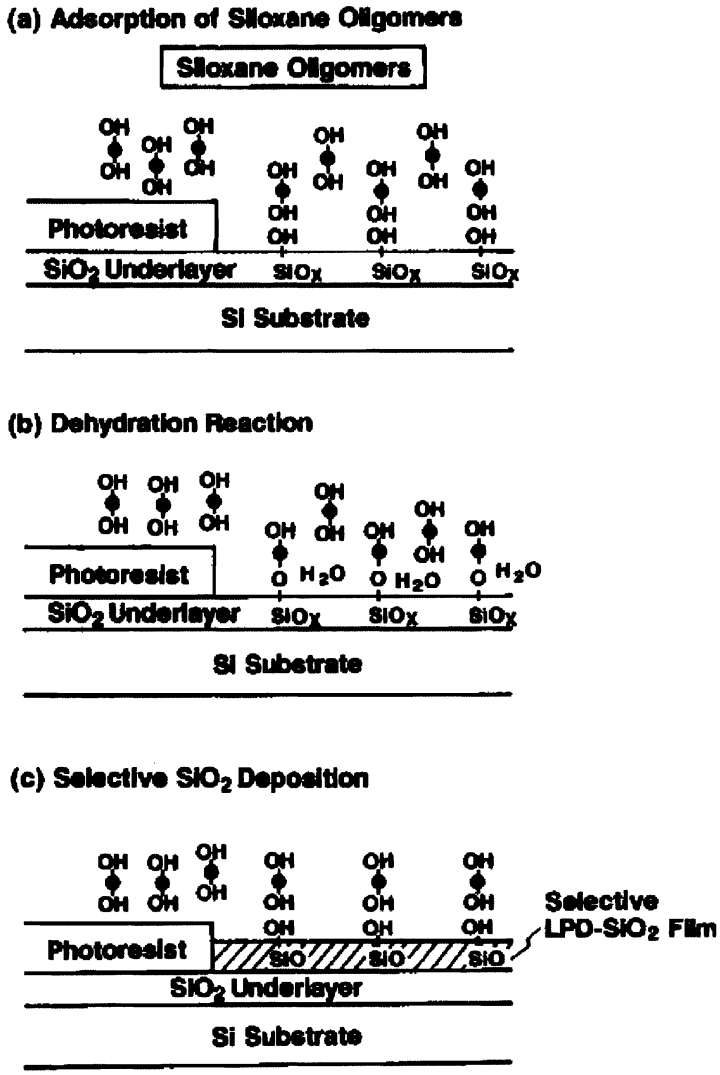


**Figure I.1.** Schematic illustration of silica LPD film deposition mechanism.[14]

Due to van der Waals interaction, CNTs tend to form bundles. In order to the get the best mechanical and electronic properties from CNTs, it is important that they be dispersed as individual nanotubes than as bundles within the matrix.[12] Additionally, a

good dispersion within a matrix would also be cost effective. Generally speaking, the ways to disperse individual nanotubes within a solvent or matrix is by functionalizing the side walls by either covalent or non covalent means. Covalent means includes performing oxidative treatments to the CNT side walls and/or attaching functional groups to the side walls of the CNTs. Treating nanotubes with acids form carboxyl and hydroxyl groups on the sidewalls, allowing the hydrophobic nanotubes to disperse well into an aqueous medium; the hydroxyl and carboxyl groups also can act as nucleation sites for the growth of the metal oxides.[13] A related example of the presence of hydroxyl groups acting as nucleation sites can be seen in Figure I.1, where the deposition of silica is taking place on a substrate which contains hydroxyl groups.[14] However, this approach has its disadvantages as acid treatments can lead to a disruption in the π-networks and therefore, a loss in the mechanical and electronic properties of the CNTs. A second, non covalent method is to treat the nanotubes with surfactants. The surfactants are used to encapsulate the individual nanotubes, as can be seen in Figure I.2.[15] Once the nanotubes are either chemically functionalized or surfacted, they can be coated with metal oxides or other metal compounds. While there are many ways to coat tubes, chemical bath deposition (CBD) and liquid phase deposition (LPD) are processes which use aqueous solvents for coating substrates at low temperatures. A CBD method refers to deposition from a solution (usually aqueous) where the deposit required is both generated and deposited at the same time.[16] LPD is just like CBD, but refers to oxide films formed from an aqueous solution of a metal-fluoro complex.[17] Anderson and co-workers show the growth of metals on hydroxyfullerenes, where the metal nanoparticle adheres to the hydroxyl group on the fullerene.[18] The aid of surfactants to grow silica on SWNTs has also been used, whereby, the SWNTs are individually dispersed in surfactants in basic and acidic mediums, and the deposition of silica takes place around the micelles which wrap the

tubes.[19,20] Similarly, the CBD of cadmium selenide on SWNTs is examined using surfactants.[21] Thus, CBD and LPD is a nice, low temperature way to coat substrates.

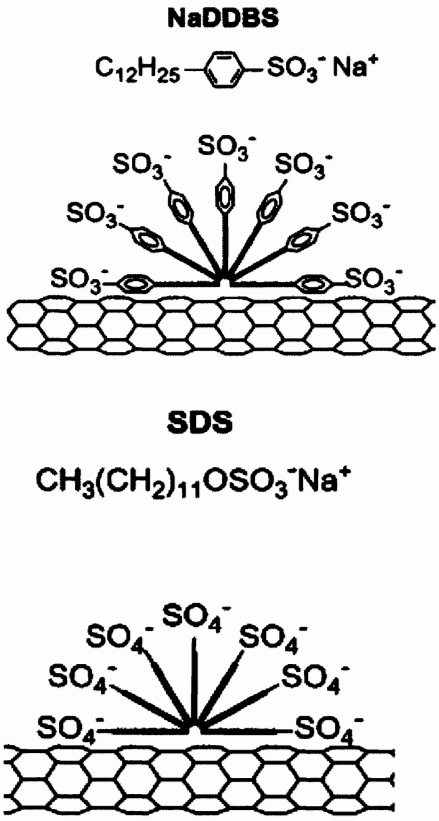


**Figure I.2.** Cartoon showing the proposed and simplistic interaction of surfactants sodium dodecylbenzene sulfomate (NaDDBS) and sodium dodecyl sulfate (SDS) with nanotubes.[15]

There are many published studies on incorporating CNTs within a polymer matrix. CNTs are generally added to improve the conductivity of polymers by reaching the percolation threshold, and increase the toughness of the polymer matrix. CNTs within polymers have found applications in the areas of nanoelectrodes, nanowires in nanoelectronics, insulated atomic force microscopy (AFM) tips, nanosensors, and adsorption of $CO_2$.[22,23] There have been various ways of incorporating or coating CNTs

with polymers and a generalization of the methods is as follows:[24] 1) CNTs are ultrasonicated or surface functionalized in the presence of matrix polymers, 2) an in-situ polymerization of monomers takes place in the presence of CNTs, and 3) the CNT surface is used for the polymerization of the monomer. Polymers are attached or coated to CNTs via covalent bonding, hydrogen bonding, and polymer wrapping around the nanotubes. Our lab has previously shown the addition of polyethyleneimine (PEI) to SWNTs by first fluorinating the side walls of the SWNTs and then forming a covalent bond with the PEI.[23] Studies show that the PEI-SWNTs are very good at adsorbing $CO_2$ and therefore, is a promising technology for green energy. Pumera et al.[22] show a new method of coating MWNTs with polypyrrole (PPy) which gives even coatings on nanotubes. They first acid treat the nanotubes to get carboxyl groups, followed by the addition of pyrrole into a solution with acid treated nanotubes. This method gave even coatings of PPy on CNTs. Previous studies have shown coating CNTs with PPy using chemical and electrochemical methods; however, these methods have given uneven and agglomerated PPy coatings on CNTs.[25,26] The PPy coated MWNTs prevents the electron transfer between the individual carbon nanotubes, and thus can be used in electronics. MWNTs are also added to conducting polymers such as poly[3-(2-hydroxyethyl)-2,5-thienylene] (PHET) via covalent and non-covalent funationalization.[24] It is found that at room temperature, the conductivity of the covalently functionalized CNT-PHET is 28 times higher than the non-covalent CNT-PHET. The authors believe this is because the addition of CNTs acts as a dopant to the polymer and therefore charge transfer between CNT and PHET takes place and is better via a covalent bond. In the biological field, scientists have used DNA oligomers and immobilized them on CNTs, with an eventual application in using it for biochemical sensing for the study of molecular recognition.[27] Therefore, the field of polymer coated CNTs is huge with varying applications in fields of electronics, energy, and biotechnology.

Using CNTs as vessels for containing or decorating metal nanoparticles has been of great interest in order to develop novel materials with unique electronic and mechanical properties. It has been reported that hydrogen sensors can be created by coating SWNTs with palladium nanoparticles,[28] gold coated MWNTs can be used for glucose biosensors,[29] and SWNT supported platinum nanoparticles allows for selective partial hydrogenation of α,β-unsaturated aldehydes.[30] Besides these, depending on the type of metal coating on CNTs, the end product can be used for catalysis of various chemicals and gases, and be used in microscopy instruments such as producing tips for AFM and scanning tunneling microscope (STM).[31,32] Many different coating methods have been used to attach metal nanoparticles to the CNTs. For example, treating CNTs with nitric acid or a mixture of nitric and sulfuric acid, small platinum metal spheres can be attached to the substrate,[33] while gold nanoparticles can be attached to CNTs when exposed to mild sonication during deposition (Figure I.3); an intense sonication has led to the nanoparticles entering the nanotubes.[34] Other groups have chemically functionalized nanotubes with cationic electrolytes and then reacted them with negatively charged gold particles, while hydrophobic interactions have also been used to attach nanoparticles to the CNT surfaces.[35] In order to create a probe for STM, glued tungsten tips have been glued to the tip of CNTs using an electron beam, and coated the sidewalls of the CNTs with tungsten using pulsed laser deposition.[36] Tripathi *et al.* have coated nanotubes with iron nanoparticles using electron beam physical vapor deposition. Given that it is difficult to control the production of only metallic or semiconducting SWNTs, coating SWNTs with iron nanoparticles will make them conductive and therefore, any batch or process of producing SWNTs can be used for applications where SWNTs are needed for conductive purposes. These iron coated SWNTs can be used as interconnects and wires in electronic applications, or for magnetic recording devices.[37]

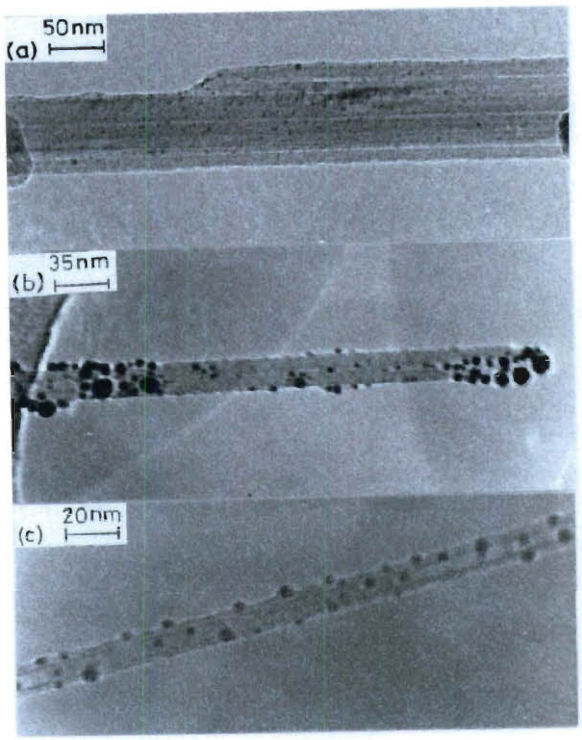


**Figure I.3.** Gold nanoparticle coatings on CNT treated with nitric acid, showing minor changes in procedure which alter the nanoparticle sizes.[34]

While CNTs have been coated for applications where both the presence of CNTs and metal coatings are important, many researchers have used CNTs as templates to either fill CNTs with metals or grow a coating of metals around it. This is followed by oxidizing and removing the CNTs from the metal wire/rods or scaffold. nanorods of $V_2O_5$, $WO_3$, $MoO_2$, $Sb_2O_5$, $MoO_2$, $RuO_2$, and $IrO_2$ have been prepared by first oxidizing the MWNTs in nitric acid, followed by treating with the CNTs acids of the metal oxides.[38] Once the MWNTs were coated, the nanotubes were heated in air at 700 °C to decompose the carbon nanotubes in order to obtain the metal oxide nanorods (Figure I.4). Other groups have acid treated the CNTs to open up the ends; this is followed by the mixing of treated nanotubes with $V_2O_5$ powder, and are heated at high temperatures where metal is molten and enters the insides of the nanotubes via capillary action (Figure

I.5).[39] However, given that there are carboxyl groups present on the surface of the nanotubes because of acid treatment, there are also $V_2O_5$ coatings present on the outside of the tubes. The group also oxidized the filled/coated tubes to decompose the CNTs.

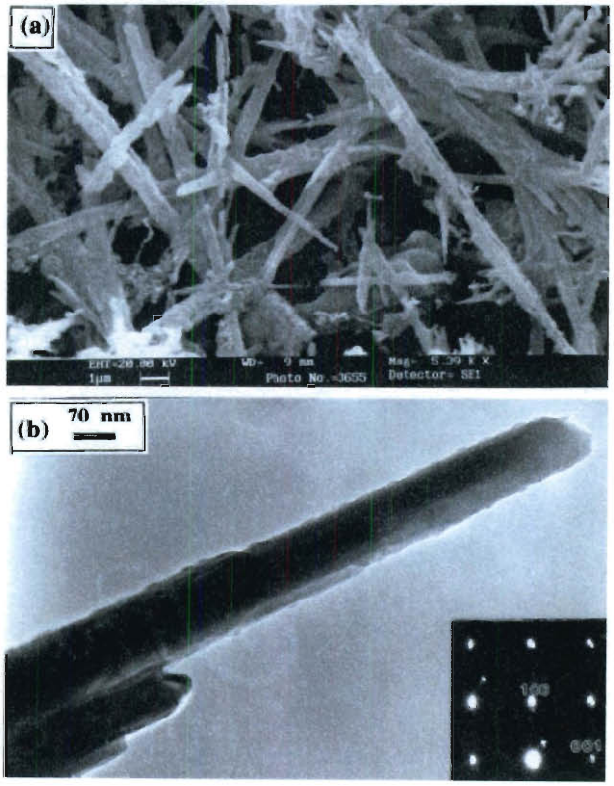


**Figure I.4.** SEM (a) and TEM (b) image of $MoO_2$ nanorods obtained after the removal of CNT which is used as a scaffold.[38]

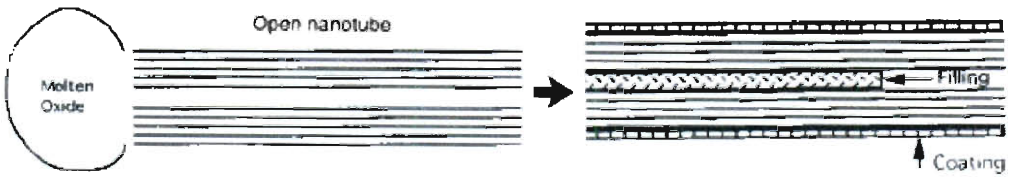


**Figure I.5.** Schematic illustration of the addition of molten metal inside the CNT.[39]

There many different methodologies used to coat nanotubes with ceramics, polymers and metals or metal oxides. These materials, as explained above have applications in various fields and opens up a whole new class of nanomaterials to be studied. The following chapters explain our efforts of coating nanotubes with ceramics, metal oxides and metal compounds. We demonstrate different techniques of coating nanotubes using LPD and CVD, and explain factors that influenced different growth morphologies. Furthermore, we discuss the role and results of these coated nanotubes in potential industrial applications. In Chapter 1, we look at different pre-treatments of VGCFs for the coatings of fibers with $SiO_2$, and discuss the differences in the growth due to the various pre-treatments employed. In Chapter 2, we take the VGCFs coated with $SiO_2$ and further functionalize it with silane groups. The functionalized coated fibers are then added to guar gum gels, and the rheological behavior is studied for applications in the oil and gas reservoirs. In Chapter 3, we look at using SWNTs as templates for the coatings of titania ($TiO_2$) and explore the role of $SiO_2$ in the growth and of $TiO_2$ coatings Furthermore, we also look at the $TiO_2$ coated SWNTs and $TiO_2$ nanoparticles doped with $SiO_2$ in the field of catalysis. Finally, in Chapter 4, we explore the different fillings and coating of lead and bismuth compounds on VGCFs, MWNTs, and SWNTs and show the best pre-treatments for growths of these compounds. We also try some initial tests for the role these coated tubes play in the absorption of X-rays.

## References

1. S. Ijima, *Nature*, 1991, **354**, 56.

2. T.W. Odom, *Aust. J. Chem.*, 2001, **54**, 601.

3. M. Terrones, *Annu. Rev. Mater. Res.*, 2003, **33**, 419.

4. F. Lupo, R. Kamalakaran, C. Scheu, N. Gobert, and M. Ruhle, *Carbon*, 2004, **42**, 1995.
5. S.R. Dhakate, R.B. Mathur, T.L. Dhami, *J. Mater. Sci.*, 2006, **41**, 4123.
6. M. Shibuya, M. Sakurai, and T. Takahashi, *Compos. Sci. Technol.*, 2007, **67**, 3338.
7. R. H. Baughman, A. A. Zakhidov, and W. A. de Heer, *Science*, 2002, **297**, 787.
8. E. T. Thostenson, Z. Ren, and T. W. Chow, *Comp. Sci. Technol.*, 2001, **61**, 1899.
9. R. Z. Ma, J. Wu, B. Q. Wei, J. Liang, and D. H. Wu, *J. Mater. Sci.*, 1998, **370**, 5243.
10. G-D. Zhan, J. Kuntz, J. Wan, and A. K. Mukerjee, *Nat. Mat.*, 2003, **2**, 38.
11. J-W An, and D-S Lim, *J. Ceram. Process. Res.*, 2002, **3**, 201.
12. F. Bonaccorso, *Int. J. Photoenergy*, 2010, **2010**, 1.
13. H. R. Jafry, E. A. Whitsitt, and A. R. Barron, *J. Mater. Sci.*, 2007, **42**, 7381.
14. T. Homma, T. Katoh, Y. Yamada, and Y. Murao, *J. Electrochem. Soc.*, 1993, **140**, 2410.
15. M. F. Islam, E. Rojas, D. M. Bergey, A. T. Johnson, and A. G. Yodh, *Nano Lett.*, 2003, **3**, 269.
16. G. Hodes, *Phys. Chem. Chem. Phys.*, 2007, **9**, 2181.
17. E. A. Whitsitt, *Liquid Phase Deposition of Silica: Thin Films, Colloids, and Fullerenes*, Ph.D., Rice University, Houston, TX, 2005.
18. R. Anderson, and A. R. Barron, *J. Am. Chem. Soc.*, 2005, **127**, 10458.
19. R. Colorado, and A. R. Barron, *Main Group Chem.*, 2005, **4**, 279.
20. E. A. Whitsitt, and A. R. Barron, *Nano. Lett.*, 2003, **3**, 775.
21. R. Loscutova, and A. R. Barron, *J. Mater. Chem.*, 2005, **15**, 4346.

22. M. Pumera, B. Smid, X. Peng, D. Goldberg, J. Tang, and I. Ichinose, *Chem. Eur. J.*, 2007, **13**, 7644.

23. E. P. Dillon, C. A. Crouse, and A. R. Barron, *ACS. Nano,* 2007, **2**, 156.

24. B. Philip, J. Xie, A. Chandrasekhar, J. Abraham, and V. K. Varadan, *Smart Mater. Struct.*, 2004, **13**, 295.

25. J. Wang, J. Dai, and T. Yarlagadda, *Langmuir*, 2005, **21**, 9.

26. M. Huges, M. S. P. Shaffer, A. C. Renouf, C. Singh, G. Z. Chen, D. J. Fray, and A. H. Windle, *Adv. Mater.*, 2002, **14**, 382.

27. S. C. Tsang, Z. Guo, Y. K. Chen, M. L. H. Green, H. A. O. Hill, T. W. Hambley, and P. J. Sadler, *Angew. Chem. Int. Ed. Engl.*, 1997, **36**, 2197.

28. J. Kong, M. G. Chapline, and H. Dai, *Adv. Mater.*, 2001, **13**, 1384.

29. S. G. Wang, Q. Zhang, R. Wang, S. F. Yoon, J. Ahn, D. J. Yang, J. Z. Tian, J. Q. Li, and Q. Zhou, *Electrochem. Commun.*, 2003, **5**, 800.

30. V. Lordi, N. Yao, and J. Wei, *Chem. Mater.*, 2001, **13**, 733.

31. Y. Yang, J. Zhang, X. Nan, and Z. Liu, *J. Phys. Chem. B.*, 2002, **106**, 4139.

32. T. Nishino, T. Ito, and Y. Umezawa, *Anal. Chem.*, 2002, **74**, 4275.

33. R. Yu, L. Chen, Q. Liu, J. Lin, K. Tan, S. C. Ng, H. S. O. Chan, G. Q. Xu, and T. S. A. Hor, *Chem. Mater.*, 1998, **10**, 718.

34. B. C. Satishkumar, E. M. Vogl, A. Govindraj, and C. N. R. Rao, *J. Phys. D*, 1996, **29**, 3173.

35. R. Zanella, E. V. Basiuk, P. Santiago, V. A. Basiuk, E. Mireles, I. Puente-Lee, and J. M. Saniger, *J. Phys. Chem. B*, 2005, **109**, 16290.

36. Y. Murata, S. Yoshimoto, M. Kishida, D. Maeda, T. Yasuda, T. Ikuno, S. Honda. H. Okado, R. Hobara, I. Matsuda, S. Hasegawa, K. Oura, and M. Katayama, *Jpn. J. Appl. Phys.*, 2005, **44**, 5336.

37. S. M. Tripathi, T. S. Bholanath, and S. Shantkriti, *Int. J. Control Autom.*, 2010, **3**, 53.

38. B. C. Satishkumar, A. Govindaraj, M. Nath, and C. N. R. Rao, *J. Mater. Chem.*, 2000, **10**, 2115.

39. P. M. Ajayan, O. Stephan, P. Redlich, and C. Colliex, *Nature*, 1995, **375**, 6532.

# Chapter 1

# Silica Coatings on Vapor Grown Carbon Fibers

## Introduction

Silica ($SiO_2$) is a very important material for the fabrication of semiconducting devices. For example it is used as gate insulators in metal-oxide semiconductor devices, the isolation layer between conductive lines, and the mask in the very large scale integrated circuit processes. As explained in the Introduction, many techniques of growing $SiO_2$ have been developed. Some of these older techniques include chemical vapor deposition (CVD), thermal oxidation, E-gun evaporation, spin-on glass, and RF reactive sputtering. However, the LPD method of depositing $SiO_2$ has many advantages over traditional methods; these include low reaction temperatures (20 - 50 °C), no necessity for a vacuum system, lower processing costs, higher throughput, selective deposition on substrates, and high-quality films. With the non LPD systems, the high processing temperatures (> 60 °C) often lead to the interdiffusion of the constituent atoms between the $SiO_2$ layer and that of the substrate, exhibit high thermal stress on the deposited layers, and redistribute the dopants within the system.[1,2,3] Therefore, with the advantages of LPD, many researchers have focused their efforts on growing $SiO_2$ films using this method. In a typical LPD system for $SiO_2$ deposition, a supersaturated solution of hydrofluosilicic acid ($H_2SiF_6$) is made by saturating it with a $SiO_2$ source such as fumed silica, silica gel, or silicic acid.[4] The supersaturated solution of $H_2SiF_6$ is reacted with water, and the deposition of $SiO_2$ occurs on the substrate (Eq 1.1).

$$H_2SiF_6 + 2H_2O \longrightarrow SiO_2 + 6HF \qquad (1.1)$$

According to this equation, deposition of $SiO_2$ can be increased by either increasing the concentration of the reactants ($H_2SiF_6$ or $H_2O$) or by decreasing the concentration of HF. Popular methods include increasing the concentration of the reactants by saturating $H_2SiF_6$ with $SiO_2$ additives and/or increasing $H_2O$, or decreasing the concentration of HF by the addition of boric acid ($H_3BO_3$) or aluminum (Al). Boric acid and aluminum react with HF to form $BF^-_4$ and $AlF_3$. As mentioned earlier, the concentration of $H_2SiF_6$ is saturated by the addition of $SiO_2$ additive. The order in which the $SiO_2$ additive and $H_2O$ is added to the growth solution is of high importance when it comes to the deposition rate of $SiO_2$. As shown by equation 1.1, deposition of $SiO_2$ occurs, but only in the presence of a substrate. According to studies by Chou *et al.*, the presence of $SiO_2$ additives can either react with any free HF in the starting $H_2SiF_6$ solution, making it a saturated $H_2SiF_6$ solution, or can act as $SiO_2$ surface which brings down the activation barrier for the $SiO_2$ precipitation from an LPD growth solution.[1] Thus, if the $H_2O$ is added to the $H_2SiF_6$ solution prior to the addition of $SiO_2$ additive, then the reaction between the two species is about to occur (Eq. 1.1) and is maintained in a metastable state without deposition until a substrate is added. If the $SiO_2$ additive is added at this point, it acts as a substrate for the LPD of $SiO_2$ to occur from the growth solution. However, if the $SiO_2$ additive is added prior to the addition of $H_2O$ into the growth solution, then as mentioned earlier, it will react with the extra HF ions to saturate the growth solution for deposition.

Another important factor to get a good $SiO_2$ growth from a LPD reaction is to have a proper substrate for the $SiO_2$ deposition. Studies have proven that $SiO_2$ growth occurs best in the presence of groups such as Si-OH or native oxide groups present on the surface of the substrate. $SiO_2$ LPD experiments performed on various substrates by Homma et al. demonstrate that substrates which contained a native oxide layer, or a Si-OH layer grew $SiO_2$ layers from a LPD reaction; however, under the same reaction

conditions on substrates which had photoresist or Teflon, no $SiO_2$ deposition occurred.[5] Yeh *et al.*[2] describe this mechanism of $SiO_2$ deposition and growth in detail as shown by the equations 1.2 – 1.4. They explain that in concentrated $H_2SiF_6$ solutions, the concentration of $SiO_2$ is sometimes beyond its solubility, forming fluorosilicon complexes such as $[SiF_6.SiF_4]^{2-}$.

$$5\ H_2SiF_6 + SiO_2 \rightarrow [SiF_6{\cdot}SiF_4]^{2-} + 2\ H_2O + 6\ H^+ \quad (1.2)$$

$$[SiF_4(OH)_2]^{2-} + 2H^+ \rightarrow SiF_4 + 2\ H_2O \quad (1.3)$$

$$3\ SiF_4 + 4\ H_2O \rightarrow 2\ SiF_6^{2-} + Si(OH)_4 + 4H^+ \quad (1.4)$$

The sililic acid is adsorbed onto the surface of the substrate which contain the Si-OH groups; a condensation reaction occurs between sililic acid and the surface silanol groups, forming Si-O-Si bonds. Following this initial formation of the Si-O-Si layer on the substrate, additional $SiO_2$ deposition occurs from the growth solution onto this layer.

Previously, SWNTs and buckminister fullerenes have been used as substrates for coatings of metal oxides via LPD.[6,7,8] In order to coat individual SWNTs with $SiO_2$, surfactants are used to aid in the dispersion of SWNTs. In an acidic medium such as $H_2SiF_6$ saturated with fumed $SiO_2$, cationic surfactants such as dodecyl trimethyl ammonium bromide (DTAB) is used to disperse the SWNTs; however, in a basic medium such as sodium silicate, anionic surfactants such as sodium dodecyl benzene sulfate (SDBS) is used for SWNT dispersion. It has been shown that in the growth solution, the presence of the surfactant micelles are in equilibrium with the surfacted SWNTs, and therefore produce silica colloids along the coated tubes. However, by keeping a low concentration of the surfactant, high concentration of SWNTs, and a low

concentration of growth solution, followed by meticulous cleaning of the coated SWNTs with ethanol (EtOH), the excessive production of colloids can be controlled and washed off. Further studies on the mechanism of LPD $SiO_2$ growth in both surfactant solutions with and without a substrate show that the micelles act as a substrate for the LPD $SiO_2$ deposition and growth. In the case of nanotubes dispersed in a surfactant solution, the water around the nanotubes is extracted as it participates in the reaction shown by Eq 1.1; this allows for the alkyl surfactant chains to get adsorbed more efficiently onto the tubes, allowing for the growth of $SiO_2$ onto the individual SWNTs.[9]

VGCFs are carbon fibers produced by depositing layers of polycarbon from the vapor phase on a catalytically grown carbon filament.[10] The fibers are approximately 100 - 300 nm in diameter, and between 3 - 10 μm in length. While much larger in diameters from SWNTs and MWNTs, VGCFs exhibit many important properties and have attracted much attention for being used as filler materials within ceramics. Mechanical tests show that VGCFs have a tensile strength value between 1.7 – 3.38 GPa, and tensile modulus between 88 – 240 GPa; they exhibit a very low electrical resistivity of $10^{-3}$ Ω cm, and a thermal conductivity of 20 $W.m^{-1}.K^{-1}$.[11,12] Various journal articles have been published on incorporating VGCFs into composite materials to enhance the properties of the composite; for example, a 5 wt.% of VGCF to the polymer matrix polymethyl methacrylate (PMMA) increases the electrical conductivity and mechanical properties of the matrix.[12] The addition of VGCFs to thermoplastic polymers allows for an enhancement of mechanical properties providing more security for goods during transportation. Additionally, VGCFs have been added to various polymers to make materials sensitive to electrostatic discharge (ESD), electromagnetic interference (EMI), and radio-frequency interference (RFI).[13] With a variety of applications, research has shown that the properties of the composite matrix is highly dependent on the dispersion and the contact of the fiber-matrix interface. Thus, VGCFs sidewalls have been

functionalized with different functional groups for better dispersion within the polymer matrix.[12,14] One possible way to achieve a better dispersion or incorporation of VGCFs into the matrix is to coat it with ceramics or metal oxides; either the coating itself can allow for an enhanced dispersion, or various chemical groups/moieties can be attached to the coatings which can help enhance the VGCF dispersion within the matrix.

As mentioned earlier, metal oxides coatings have been demonstrated on buckyballs and SWNTs, which are used as substrates for LPD coatings. In the present case, we functionalize and coat VGCFs with $SiO_2$ via LPD to obtain the most even coating/growth of $SiO_2$. These $SiO_2$ coated VGCFs ($SiO_2$-VGCFs) can be potentially used as fillers in the pores of the space shuttle tiles to absorb radiation heat.

Standard space shuttle tiles (LI-2200) are made of silica fibers that have a density of approximately 3.52 $kg.m^{-3}$ and low thermal conductivity (thru-the thickness) of 7.443 x $10^{-2}$ $W \cdot m^{-1} \cdot K^{-1}$ at low temperatures.[15] The ceramic fibers are made by combining constituent silica fibers into a water-based slurry, which is then axially compressed in a casting tower and fired in a high temperature furnace. The result is a three dimensional, highly complex, anisotropic fiber that is aligned normal to the pressing direction.[16] The silica fibers are then combined in an amorphous assembly of fibers held together with a colloidal silica binder. The diameter of the silica fiber is approximately 10 μm, and the overall porosity of the tile is close to 90%.[17] It is generally assumed that the pore size between fibers is three times the diameter of the fibers. The high porosity helps keep the thermal conductivity down at lower temperatures; however, at temperatures above 1093 °C radiative transfer of heat occurs that is directly proportional to the pore size of the ceramic material used since the pores are transparent to radiation.[18] The photons go through the pores and are absorbed and reradiated by the fibers. In order for the space shuttle tiles to stay thermally insulating at higher temperatures, the porosity of the ceramic tile could to be reduced by closing the pores of the material through which the

radiative heat transfer can take place. This could be achieved by adding more silica fibers which would lead to an undersirable increase in tile density, and more significantly the ceramic forms a conductive path through the solid phase specially at lower temperatures. Thus, filling the pores with silica fibers increases conduction heat at low temperatures and not doing so creates radiation heat at high temperatures.[19] Our hypothesis is that filling the pores with nanoscale carbon fibers coated with silica will allow for a greater surface area for absorption and re-radiation of photons, without affecting the density of the silica tile significantly. In our lab, it has been previously demonstrated that single walled carbon nanotubes (SWNTs) can be coated with silica, thus creating nanoscale silica fibers;[6] unfortunately at present the use of silica coated SWNTs would not be economically advantagous since the pore size is large. However, it would be cost effective to use VGCFs as a template. Our goal is therefore to develop smooth and even silica coating on VGCFs. These silica coated VGCFs ($SiO_2$-VGCFs) could then be employed in composite applications and as silica fiber templates.

## Results and Discussion

**Synthesis and characterization of silica coated VGCFs ($SiO_2$-VGCF).** It has been reported that the LPD of silica from fluorosilicic acid/fumed silica solutions yield silica coatings containing fluorine.[20] The coatings on the VGCFs contain similar levels of fluorine as indicated by IR and Raman spectroscopy (Figures 1.1 and 1.2). In addition, the Raman spectrum (Figure 1.2) shows the presence of VGCFs within the silica coating. If no acid pretreatment is employed then the VGCFs show little or no coating. Instead they appear to be incorporated into particulate silica (Figure 1.3).

Previously, similar results have been obtained with the LPD of silica in the presence of $C_{60}$.[9] In our case, the most uniform coatings were obtained with the Type II acid treatment (see Experimental). Figure 1.4a shows an SEM image of the silica-coated

VGCFs. As may be seen under optimum conditions each VGCF appears uniformly coated with an essentially featureless coating.

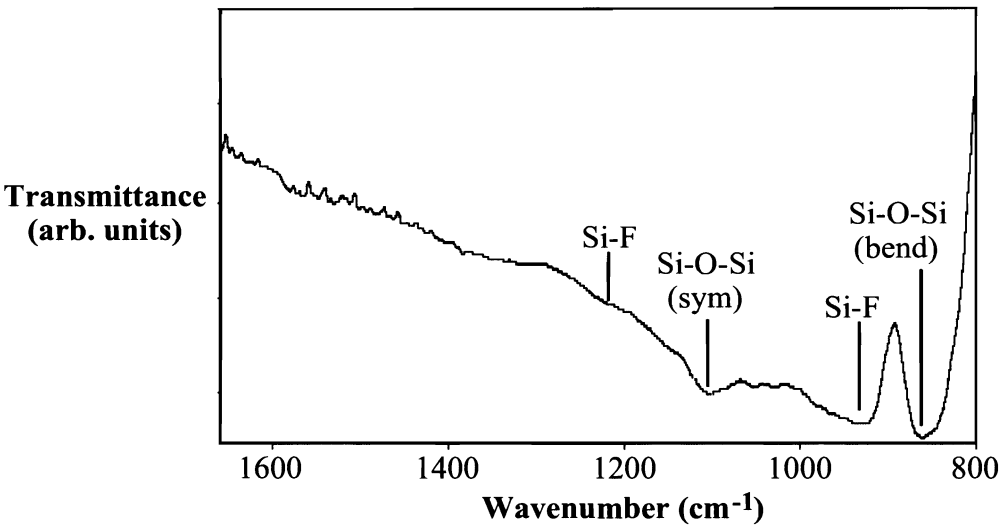


**Figure 1.1.** IR spectra showing the presence of Si-O-Si present around the VGCFs.

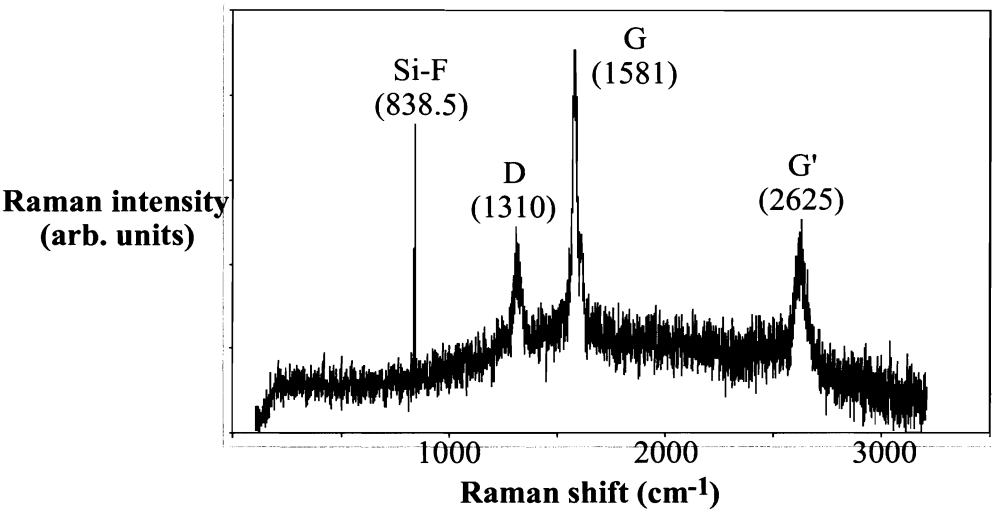


**Figure 1.2.** Raman spectra (using 532 nm excitation) of silica coated VGCFs showing the presence of VGCFs and the F-containing silica. Band assignments are provided.

EDX analysis showed that each of the VGCFs was coated with silica. Based upon a comparison with the untreated VGCFs (Figure 1.5a) the coating is approximately 90 - 100 nm after 4 hours treatment (Figure 1.5b).

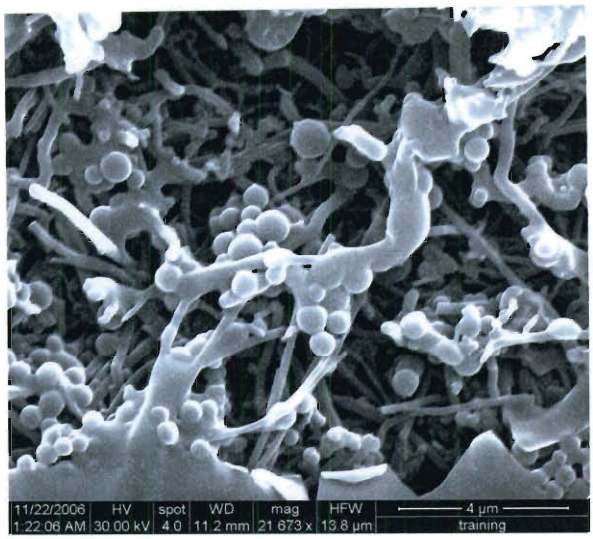


**Figure 1.3.** SEM image of Type II treated VGCFs (Pyrograph III) treated with silica LPD solution without any acid pretreatment of the VGCFs showing the presence of uncoated VGCFs and silica particles.

In order to compare the conformality of the silica coatings in comparison to that previously reported for SWNTs the use of DTAB surfactant was investigated.[16] Adding surfactant to the VGCF/$H_2O$ solution and then exposing the suspension to the LPD solution gave a very uneven and colloidal growth on the tubes (Figure 1.6). Previously in our lab, it has been demonstrated that adding DTAB to the LPD silica solution creates individual spheres as a result of the micelles in solution.[21] The presence of surfactant on the VGCF reaction appears to have had the same templating effect and encourages growth of silica spheres. It is interesting to note that the majority of the spheres are attached to the sidewalls of the VGCFs and that there does appear to be a coating on the fibers under the spheres. Thus, the presence of the DTAB results in a competition

between deposition on the VGCF surface and the micelle. We can conclude that, in contrast to the $SiO_2$ coating results with SWNTs, we have found that in the case of VGCFs, acid treatment rather than a surfactant promotes uniform coatings.

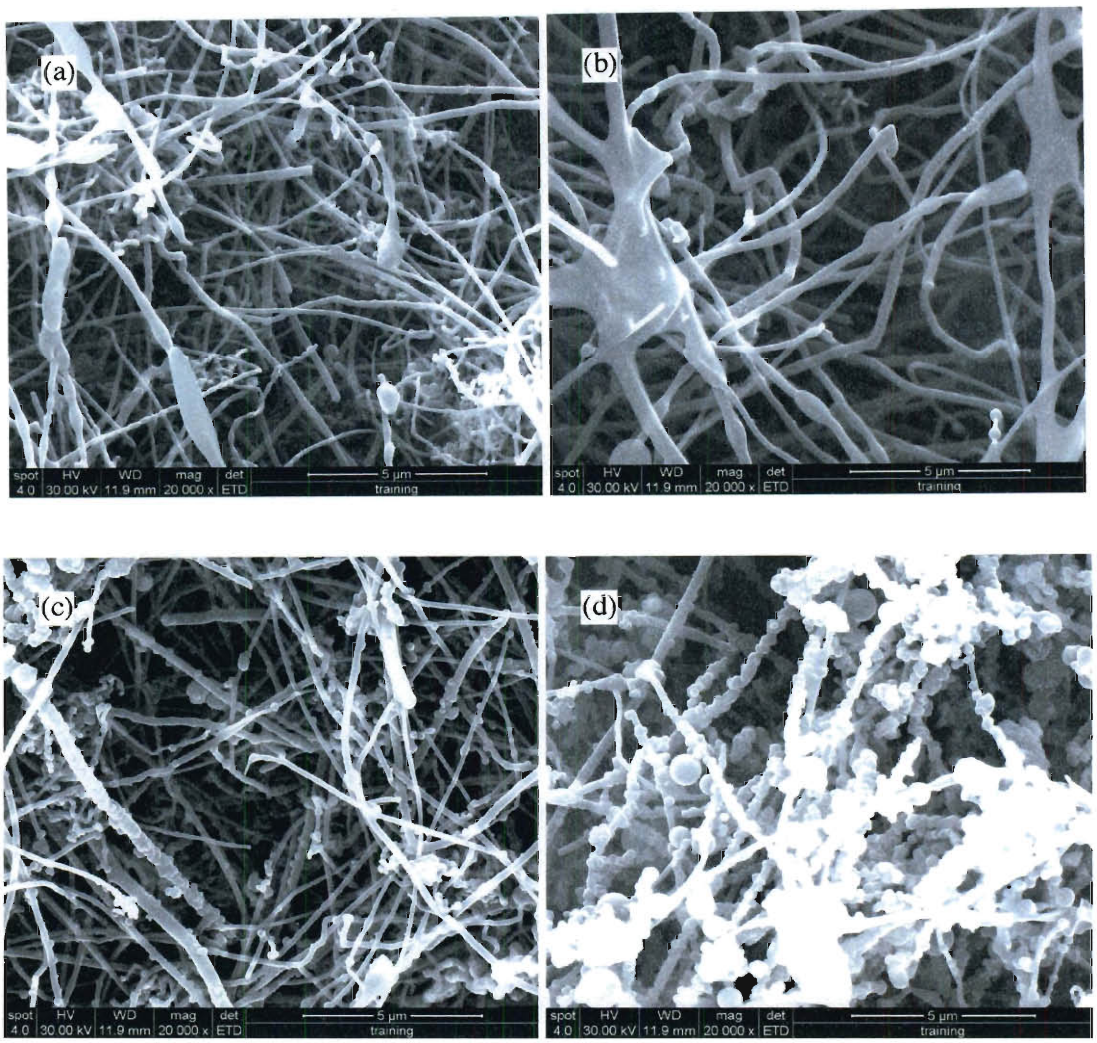


**Figure 1.4.** SEM image of Type II treated VGCFs (Pyrograph III) coated with silica for (a) 4 hours, (b) 8 hours, (c) 20 hours, and (d) 24 hours.

**Effect of VGCF pretreatment.** Amongst the three different acid treatments that have been performed on the VGCFs, the Type II method developed in our laboratory (involving heating VGCFs in nitric acid in open air for five days) gave the best coating

for the VGCFs irrespective of the source (Table 1.1). The Type I treatment developed by NASA Johnson Space Center gave a comparable silica coating for fibers treated from MER Corp., but gave worse results for Pyrograph III VGCFs that were obtained from NASA. In general acid treatment Type I resulted in lumpy coatings, although all the VGCFs appeared coated (Figure 1.7). In contrast, Type III treatment resulted in the VGCFs becoming imbedded in large silica particles (Figure 1.8).

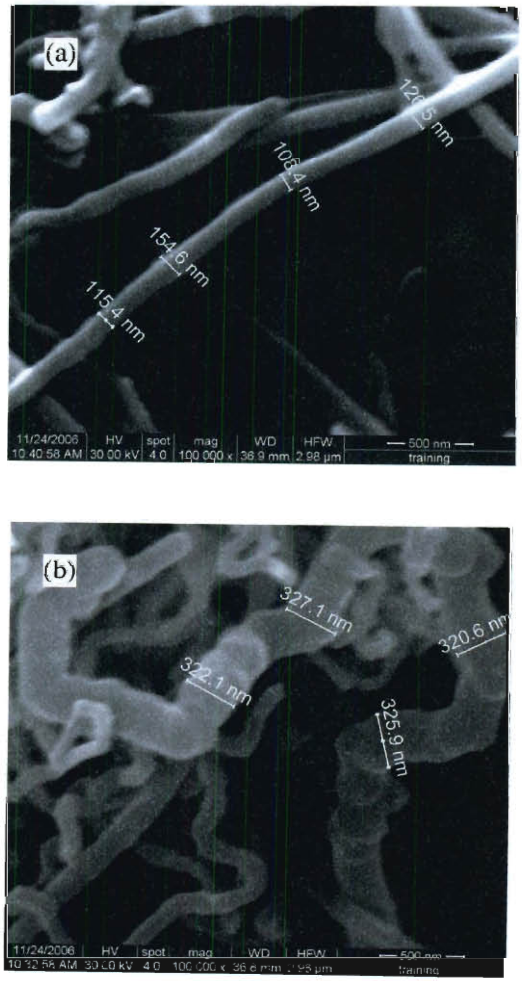


**Figure 1.5.** SEM image of Type II treated VGCFs (Pyrograph III) (a) before and (b) after silica LPD for 4 hours showing the presence of a 90 - 100 nm silica coating.

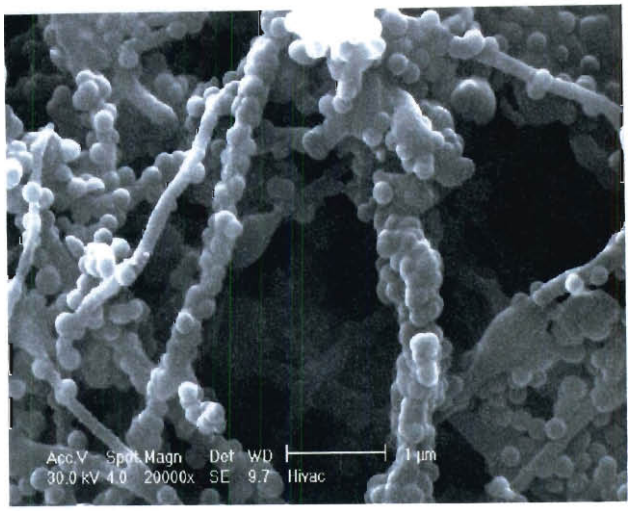


**Figure 1.6.** SEM image of VGCFs (Pyrograph III) in DTAB coated with silica for 4 hours, showing the presence of silica spheres resulting from the interaction of the silica LPD solutions with the DTAB micelles.

**Table 1.1.** Summary of coating experiments.

| VGCFs | Acid Treatment | Surfactant | Deposition time (h) | Appearance |
|---|---|---|---|---|
| Pyrograph III (NASA) | I | none | 4 | thick overlapping colloidal growth along the VGCFs |
| Pyrograph III (NASA) | I | none | 20 | colloidal growth on agglomerated VGCFs |
| Pyrograph III (NASA) | I | none | 24 | thin coating, sparse Colloids |
| Pyrograph III (NASA) | II | none | 4 | thin and even growth; regions of thicker growth |

Table 1.1. cont'd

| VGCFs | Acid Treatment | Surfactant | Deposition time (h) | Appearance |
|---|---|---|---|---|
| Pyrograph III (NASA) | II | none | 8 | thicker growth than 4 h; uniform growth with few very small colloids |
| Pyrograph III (NASA) | II | none | 20 | sparse but bigger colloids along the VGCFs |
| Pyrograph III (NASA) | II | none | 24 | thick tightly packed colloids |
| Pyrograph III (Air Force) | II | none | 4 | uniform coating, few scattered colloids |
| Pyrograph III (Air Force) | II | none | 8 | uniform coating, with colloids |
| Pyrograph III (Air Force) | II | none | 20 | some uniform coating; significant colloids |
| Pyrograph III (Air Force) | II | none | 24 | mostly colloids, chunky covering VGCFs |
| Pyrograph III (Air Force) | II | DTAB | 4 | evenly spaced colloids along the VGCFs |
| Pyrograph III (Air Force) | II | DTAB | 8 | evenly spaced colloids along the VGCFs |
| Pyrograph III (Air Force) | II | DTAB | 20 | colloidal growth; colloids growing on top of one another |

Table 1.1. cont'd

| VGCFs | Acid Treatment | Surfactant | Deposition time (h) | Appearance |
|---|---|---|---|---|
| Pyrograph III (Air Force) | II | DTAB | 24 | colloidal growth; colloids growing on top of one another |
| Pyrograph III (Air Force) | III | none | 0.5 | - |
| Pyrograph III (Air Force) | III | none | 3 | VGCFs in a silica matrix |
| MER | I | none | 4 | even and thick silica growth; some sparsely spaced colloids |
| MER corp. | I | none | 8 | some fibers have thick uniform growth; colloids and thick silica growth |
| MER corp. | I | none | 20 | mostly colloidal growth |
| MER corp. | I | none | 24 | heavy colloidal growth; chunks of silica between or binding VGCFs |
| MER corp. | II | none | 4 | even, thin growth growth; sparse small colloids |
| MER corp. | II | none | 20 | even and thick growth; colloids and thick growth |
| MER corp. | II | none | 24 | thicker and more colloids than the 20 h. run; |

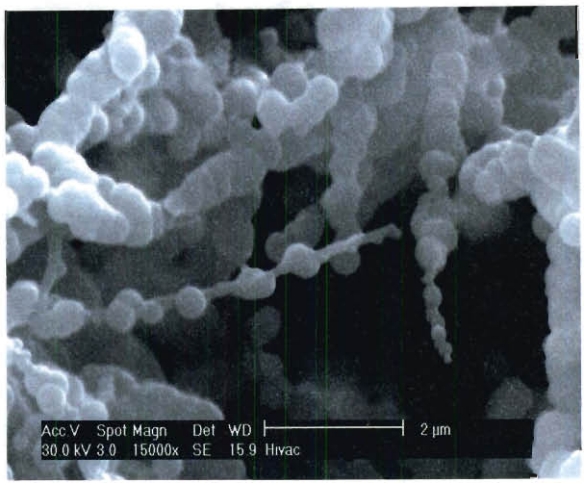


**Figure 1.7.** SEM image of Type I treated VGCFs (Pyrograph III) coated with silica for 4 hours.

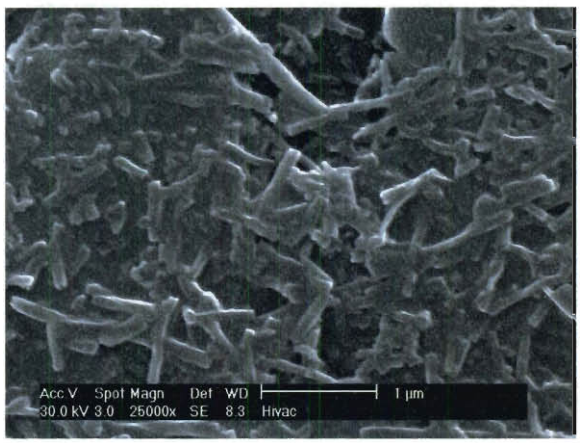


**Figure 1.8.** SEM image of Type III acid treated VGCFs (Pyrograph III) coated with silica for 3 hours.

In addition, SEM characterization was difficult to perform on tubes oxidized using Type III acid treatment, because after coating with silica the tubes are still highly dispersible in MeOH:EtOH (1:4) solution making it difficult to centrifuge them. These coated fibers would be ideal for applications in which silica-VGCFs are required to stay suspended in solution for to allow for further surface modification, i.e., reaction with an

organic silane to promote miscibility in organic matricies (e.g., visco-elastic surfactants or fracturing fluids).

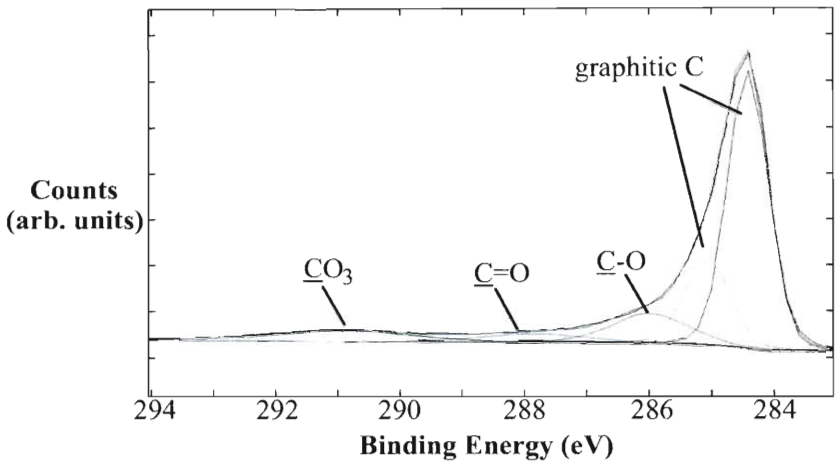


**Figure 1.9.** High resolution $C_{1S}$ XPS spectrum for Type II acid treated MER VGCFs showing the presence of different carbon species.

As we noted in the introduction, we have observed that LPD growth onto carbon nanomaterials requires surface activation of the material in order to ensure uniform deposition.[9,20] In the absence of surface hydroxides on the VGCFs, homogeneous nucleation occurs resulting in a particulate material rather than a coating. It would be expected therefore that the greater the hydroxylation of the VGCFs the greater the propensity for the formation of a contiguous coating. XPS results in Table 1.2 show that compared to all the different raw tubes as received, there is an increase in oxidation for each acid treatment. It has been reported[22,23,24] that the $C_{1S}$ spectra can be fitted for different carbon types (i.e., graphitic, C-O, C=O, and carbonate), e.g., Figure 1.9. Table 1.3 provides the relative hydroxyl content (as assigned to a peak at 286.0 – 286.9 eV) for each of the acid treated VGCFs. Irrespective of VGCF source, Type I treatment results in the smallest increase in oxygen (and hydroxyl) content as compared to the untreated

samples (see Tables 1.2 and 1.3). This is reflected in the non-uniform silica growth shown in Figure 1.7, where there is significant colloid formation. Compared to this, silica growth on tubes with a higher percentage of hydroxyl groups shown in Figure 1.4 shows a much more uniform and continuous coating. This colloidal growth is most likely because presence of hydroxyl groups allow for a heterogeneous growth of silica on surface, while a homogenous colloidal silica growth is seen when few or no hydroxyls are present.[25]

Also consistent with the quality of the observed coating and the oxygen content is that the Type II treatment has significantly greater oxygen content than the VGCFs treated with the Type I treatment (Tables 1.2 and 1.3). Type III acid treatment is comparable to Type II treatment in terms of percent oxidation and percent hydroxyl groups present suggesting the coating results should be comparable. However, for reasons not completely understandable, it is difficult for this solution to be centrifuged in the presence of alcohols compared to tubes treated with Type II oxidation. The only significant difference between the VGCFs exposed to Type II and III treatments is that XPS suggest the latter contain a higher percentage of carbonyl, quinine, and carboxyl (i.e., C=O) groups.

**Effect of deposition time.** The deposition time plays a very crucial role in growth of silica around the VGCFs. Comparing the 4-hour runs to the 8, 20 and 24 hour runs in Figure 1.4, one can easily tell of the excessive colloidal growth on the fibers (Table 1.1). One reason for this could be that heterogeneous silica growth occurs on the surface of the substrate due to the presence of the hydroxyl groups. However, once the silica film is formed around the tube, additional silica formed is in solution, which promotes a homogenous growth, leading to the formation of colloids.

For all the different treatments of acid performed on the VGCFs, colloidal growth was observed at 20 hours (and longer). All of the 4-hour growth runs gave the least colloidal growth with the exception of the Type I acid treatment performed on the Pyrograph fibers from NASA, which have low hydroxyl content. The best results were obtained by Type II acid treatment for both 4 and 8 hour runs on the Pyrograph III VGCFs obtained from NASA as well as from MER (Figure 1.4a and b). Interestingly the Type II acid treatment on Pyrograph III VGCFs received from the Air Force gave a very colloidal growth for the 8 hour run, despite the significant presence of hydroxyl groups.

**Table 1.2.** Atomic concentration of $C_{1s}$ and $O_{1s}$ obtained from XPS.

| VGF Sample ID | Treatment | $C_{1s}$ (%) | $O_{1s}$ (%) |
|---|---|---|---|
| Pyrograph III (NASA) | n/a | 95.59 | 4.41 |
| Pyrograph III (NASA) | Type I | 95.37 | 4.63 |
| Pyrograph III (NASA) | Type II | 90.2 | 9.8 |
| Pyrograph III (Air Force) | n/a | 94.9 | 5.1 |
| Pyrograph III (Air Force) | Type II | 72.63 | 27.37 |
| Pyrograph III (Air Force) | Type III | 79.59 | 20.41 |
| MER corp. | n/a | 99.23 | 0.77 |
| MER corp. | Type I | 97.23 | 2.77 |
| MER corp. | Type II | 96.18 | 3.82 |

**Table 1.3.** Percentage area of functional groups in $C_{1s}$ spectra (%).

| VGCF Sample | Treatment | graphitic[a] | C-O[b] | C=O[c] | $CO_3$[d] |
|---|---|---|---|---|---|
| Pyrograph III (NASA) | n/a | 90.21 | 2.82 | 4.60 | 2.37 |
| Pyrograph III (NASA) | Type I | 83.04 | 6.39 | 4.16 | 6.40 |
| Pyrograph III (NASA) | Type II | 76.99 | 11.02 | 6.5 | 5.48 |
| Pyrograph III (Air Force) | n/a | 80.91 | 9.85 | 4.94 | 4.3 |
| Pyrograph III (Air Force) | Type II | 70.75 | 15.23 | 9.92 | 4.1 |
| Pyrograph III (Air Force) | Type III | 65.14 | 15.04 | 15.22 | 4.6 |
| MER corp. | n/a | 78.61 | 8.55 | 5.42 | 7.43 |
| MER corp. | Type I | 79.22 | 10.26 | 3.29 | 7.23 |
| MER corp. | Type II | 75.5 | 12.84 | 5.56 | 6.38 |

[a] Graphitic carbon: 284.3 – 284.6 eV and 284.7 – 285.4 eV; error within 0.5 eV range, [b] Hydroxyl: 286.0 -386.9 eV; error within 0.5 eV range, [c] Carbonyl: 287.8 – 288.7 eV; error within 0.5 eV range, [d] Carbonate: 289.1 – 290.8 eV and 291.0 – 292.2 eV; error within 0.5 eV range.

## Conclusions

We have investigated three different acid treatments for the activation of VGCFs towards coating with silica via a LPD process. It was found that irrespective of the type of VGCF, heating a suspension of VGCFs in nitric acid to dryness (Type II) gave us the best results in terms of silica growth around the VGCF. We also found that there is a correlation between the percent of hydroxyls present on the VGCF surface and on the

type of growth that occurs on the VGCF. Between the three acid treatments, Type II and Type III treatments gave a higher hydroxyl oxidation percent that Type I. Silica coating fibers treated using Type III treatment was highly soluble in EtOH, and hence difficult to wash off excess silica that may be present, making it difficult to see individual silica fibers.

## Experimental

VGCFs are obtained from Wright Patterson Air Force Base (Pyrograph III, 450.19, Applied Science Inc), NASA Johnson Space Center (Pyrograph III, 513.08, Applied Science Inc.) and MER Corporation (MRCSD). Fluorosilicic acid (34% by weight, $H_2SiF_6$) and fumed silica (99% pure, $SiO_2$) were obtained commercially (Sigma-Aldrich) and were used without any further purification. Surfactants dodecyl tri-methyl ammonium bromide (DTAB) was used as received (Sigma-Aldrich). Nitric acid (69 - 71 wt. %), MeOH and acetone (Fisher), and EtOH (absolute 200 proof, Aaper) were used as received. Ultra pure (UP) water was obtained from a Millipore Milli-Q UV water filtration system. Solutions were filtered using Millipore Express PLUS Membranes made of polyethersulfone with 0.22 μm and 0.1 μm pore sizes and Cole Parmer PTFE filters with 0.20 μm pore size. All reactions were performed in polypropylene centrifuge tubes (50 mL, Corning) in a heated water bath. Centrifugation was performed on an IEC Centra MP4 centrifuge.

**Nitric acid oxidation.** Three different oxidation methods are employed to pre-treat the VGCFs in order to promote coating of silica. Type I treatment was performed at NASA Johnson Space Center from whom we received the treated VGCFs. Type III treatment is similar to previously published oxidation treatments where VGCFs are refluxed in concentrated nitric acid (69 - 71 wt.%) at 115 °C for different time intervals.[24]

Type I treatment performed on the VGCFs by NASA Johnson Space Center was achieved by refluxing VGCFs (~1 g) in concentrated nitric acid (27 wt.%,200 mL) in a round bottom flask for two days, after which the solution was cooled to room temperature and continually stirred for 5 days. The treated VGCFs were filtered and washed with DI water until a pH 6 was achieved. The fibers were washed with anhydrous EtOH and dried.

Type II acid treatment was achieved by reacting VGCFs (~50 mg) to dryness in concentrated nitric acid (50 - 70 wt.%, 50 mL) while stirring in a Pyrex beaker at 40 ºC for 5 days.[7]

Type III acid treatment involves refluxing VGCFs (~250 mg) in concentrated nitric acid (50 - 70 wt.%, 250 mL) for one day in a round bottom flask. The solution was allowed to cool to room temperature and was added slowly to DI water (375 mL); the mixture was allowed to cool for 20 minutes. At small intervals, acetone (500 mL) was added to this mixture, and the solution was vacuum filtered using a 0.2 μm Teflon filter. The filtrate was dried out in a beaker at 40 °C. Table 1.2 summarizes the relative increase in oxygen content of the VGCFs before and after the different acid treatments as determined by XPS.

**Silica coating on VGCFs.** Two silica-coating treatments are employed: with and without surfactant. Fumed silica (3 g) was added to fluorosilicic acid ($H_2SiF_6$, 50 mL, 2.10 M) in a Teflon cup and the mixture was stirred overnight. The concentrated solution was filtered through a 0.22 μm Millipore filter. Pre-treated VGCFs (25 mg) were added to DI water (100 mL) in a glass beaker and were bath sonicated for 20 minutes and heated overnight at 85 ºC. The VGCF/water mixture (17.2 mL) was added to the concentrated $H_2SiF_6$ solution (7.8 mL) in a plastic centrifuge tube and placed in a water bath at 40 °C. The addition of water diluted the $H_2SiF_6$ solution to 0.66 M. The solutions

were allowed to react for 4, 8, 20, and 24 hours. The reaction was then centrifuged and the supernatant was discarded. The solid left at the bottom was dispersed in a MeOH:EtOH (1:4) solution. The centrifugation/dispersion cycle was repeated four times.

VGCFs (25 mg) previously treated in nitric acid air for 5 days (Type II acid treatment) were mixed in DI water (100 mL), and were bath sonicated for 20 minutes and heated overnight at 85 °C. 1% by wt. DTAB (1 g) was added to the VGCF/water solution and pulse sonicated (3 seconds on/1 second off) in a probe sonicator for 20 minutes. VGCF/water mixture (17.2 mL) was added to the concentrated $H_2SiF_6$ solution (7.8 mL) in a plastic centrifuge tube and a stirrer placed in a water bath at 40 °C. The solutions were allowed to react for 4, 8, 20, and 24 hours. The reaction was then centrifuged and the supernatant was discarded. The solid left at the bottom was dispersed in a MeOH:EtOH (1:4) solution. The centrifugation/dispersion cycle was repeated four times. Table 1.1 summarizes the appearance of the silica coatings with different acid pretreatment, deposition times, and the effect of surfactant.

## References


1. J. S. Chou and S. C. Lee, *J. Electrochem. Soc.,* 1994, **141**, 3214.
2. C - F Yeh, C - L Chen, and G –H Lin, *J. Electrochem Soc.,* 1994, **141**, 3177.
3. N. F Wang, W. J Chang, M. P Houng, Y. H Wang, and C. J Huang, *J. Vac. Sci. Technol. A,* 1999, **17**, 102.
4. P – H Chang, C - T Huang, and J - S Shie, *J. Electrochem. Soc.,* 1997, **144**, 1144.
5. T. Homma, T. Katoh, Y. Yamada, and Y. Murao, *J. Electrochem. Soc.,* 1993, **140**, 2410.
6. E. A Whitsitt and A. R. Barron, *Nano Lett.,* 2003, **3**, 775.
7. R. Colorado, Jr. and A. R. Barron, *Chem. of Mater.,* 2004, **16**, 2691.

8. R. E. Anderson and A. R. Barron, *Main Group Chem.*, 2005, **4**, 279.

9. E. A Whitsitt, *Liquid Phase Deposition of Silica: Thin Films, Colloids, and Fullerenes,* Ph.D., Rice Univesity, Houston, TX, 2005.

10. G. G. Tibbetts, G. L. Doll, D. W. Gorkiewicz, J. J. Moleski, T. A. Perry, C. J. Dasch, and M. J. Balogh, *Carbon,* 1993, **7**, 1039.

11. S. R. Dhakate, R. B. Mathur, and T. L. Dhami, *J. Mater. Sci.,* 2006, **41**, 4123.

12. M. Shibuya, M. Sakurai, and T. Takahashi, *Compos.Sci.Technol.,* 2007, **67**, 3338.

13. K. Lozano, *J. Mater.*, 2000, **52**, 34.

14. G. G. Tibbetts, M. L. Lake, K. L. Strong, and B. P. Rice, *Compos.Sci.Technol.,* 2007, **67**, 1709.

15. NASA information on space shuttle tiles accessed on 8-16-2006; http://tpsx.arc.nasa.gov/index.html

16. J. Marschall and F. S. Milos, *J. Thermodyn. Heat Transfer*, 1998, **12**, 528.

17. T. W. Clyne, I. O. Golosnoy, J. C. Tan, and A. E. Markaki, *Phil. Trans. R. Soc. A.*,2006, **364**, 125.

18. R. W. Rice. *Porosity of ceramics*; Materials engineering 12; Marcel Dekker Inc: New York, NY, 1998; 315-368.

19. D. A. Stewart and D. B. Leiser, *Ceram. Eng. and Sci. Proc.*, 1985, **6**, 769.

20. E. A. Whitsitt, V. C. Moore, R. E. Smalley, and A. R. Barron, *J. Mater. Chem.*, 2005, **15**, 4678.

21. E. A. Whitsitt and A. R. Barron, *J. Colloid Interface Sci.*, 2005, **287**, 318.

22. Y. Xie and M. A. P. Sherwood, *Chem. Mater.*, 1990, **2**, 293.

23. P. V. Lakshminarayanan, H. Toghiani, and C. U. Pittman Jr., *Carbon.*, 2004, **42**, 2433.

24. J. F. Moulder, W. F. Stickle, P. E. Sobol, and K. D. Bomben. *Handbook of X-ray Photoelectron Spectroscopy*. Perkin-Elmer Group, Eden Prarie, MN, 1995.

25. E. A. Whitsitt and A. R. Barron, *Chem. Commun.*, 2003, **9**, 1042.

# Chapter 2

# Effect of Functionalized Nanomaterials on the Rheology of Boate Cross-linked Guar Gum

## Introduction

With an ever increasing global need for energy and declining production curves of many newly explored oil and gas wells, there is a need to maximize the recovery of oil and gas from subterranean formations or reservoirs. In order to accomplish this goal it is important to obtain information on the flow characteristics or porosity of the rock within the reservoir. Characterization has traditionally been accomplished using techniques such as seismic measurements and NMR well logging; however, these methods have severe limitations and new methods are being sought. Because of the low porosity and permeability of many oil and gas reservoirs even after hydraulic fracturing, any sensor or tracer material must be sufficiently small to allow for its transport through the rock formation. Therefore, nanoparticles represent a potential sensor material. However, while it is possible to prepare nanoparticles with suitable properties for detection, it is important to understand whether they are compatible with traditional downhole processes.

Hydraulic fracturing is a stimulation treatment routinely performed on oil and gas wells in low-permeability reservoirs, such as the shale gas fields that represent the largest potential source of natural gas in the US. Specially engineered fracture (*frac*) fluids are pumped at high pressure and flow rate into the reservoir causing a fracture to occur.[1] The wings of the fracture extend away radially from the wellbore according to the natural stresses within the formation. Proppant, such as sand or ceramic particles of a particular size, is mixed with the treatment fluid to keep the fracture open when the treatment is complete, thus creating a high-permeability path.[2,3] Guar gum cross-linked with borate to make a viscoelastic hydrogels is one of the

commonly employed fracturing fluids. The polysaccharide guaran ($M_w \approx 10^6$ Da) is the major (>85 wt.%) component of guar gum, and consists of a (1→4)-β-D-mannopyranosyl backbone with α-D-galactopyranosyl side chain units attached via (1→6) linkages. Although the exact ratio varies between different crops of guar gum the general structure is consistent with about one galactose to every other mannose (Figure 2.1).[4]

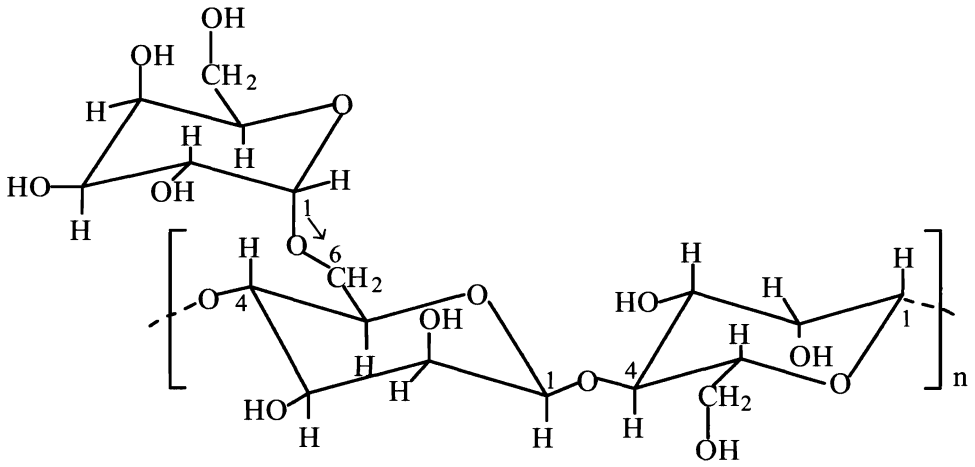

**Figure 2.1.** The repeat unit of guaran, a naturally occurring polysaccharide, consisting of (1→4)-β-D-mannopyranosyl units with α-D-galactopyranosyl side chains attached to about every other mannose via (1→6) linkages.

Given the interest in the potential of nanoparticles to be used as sensors during a fracturing job to determine the efficacy of the process, it is important to asses the effect of nanoparticles on the flow of a typical fracturing fluid. Here, we investigated the effects of added nanoparticles on the rheology of guar fluids. Rate-dependent viscosity is an important property of fracturing fluids, as the fracture creation, efficiency of fluid transport, and placement of the proppant depends upon the viscosity of the fracturing fluid.[5] For our initial studies we have chosen a particle that is larger than typical nanoparticles proposed for downhole use to represent a worse

case scenario. These are vapor grown carbon fibers (VGCFs) which we have previously shown may be coated by silica.[6] In addition, the silica can be readily functionalized by chemical modification.[7,8]

## Results and Discussion

Initially, three derivatives of nanoparticle were investigated: 1) unfunctionalized VGCFs, 2) silica coated VGCFs ($SiO_2$-VGCFs), and 3) octadecyltrichlorosilane (ODS) functionalized silica coated VGCFs (ODS-$SiO_2$-VGCFs). The unfunctionalized VGCFs were studied to gauge the effects of an inert nanoparticle, while the use of $SiO_2$-VGCFs was intended to allow for a comparison of the effects of a typical oxide nanoparticle with the VGCF. Finally, the reaction of the $SiO_2$-VGCFs with ODS results in a nanoparticle with an organic substituted surface that can simulate either a surfacted nanoparticle or a typical surface stabilized nanoparticle.[9]

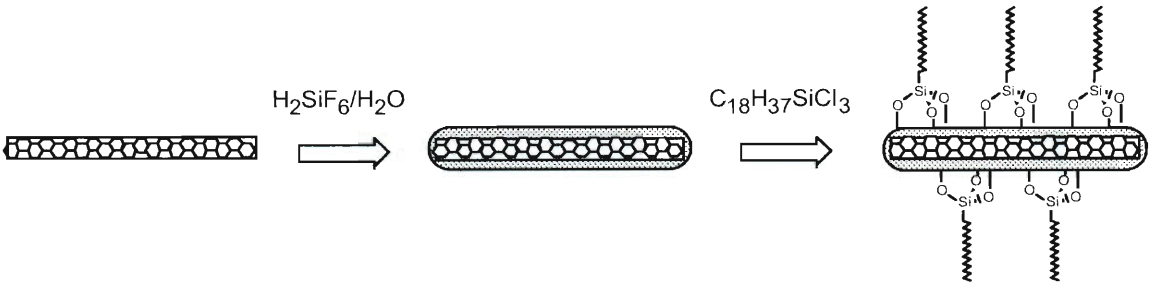


**Figure 2.2.** Schematic representation of the conversion of VGCFs to $SiO_2$-VGCFs and ODS-$SiO_2$-VGCFs.

The $SiO_2$-VGCFs were prepared by a liquid phase deposition process,[10] while the reaction of $SiO_2$-VGCFs with octadecyltrichlorosilane ($C_{18}H_{37}SiCl_3$) resulted in ODS-$SiO_2$-VGCFs (Figure 2.2). X-ray photoelectron spectroscopy (XPS) analysis of ODS-$SiO_2$-VGCFs (Figure 2.3) confirms the reaction (and surface functionalization) by the

presence of peaks assigned to both silica (103.13 and 103.79 eV) and an organosilane (102.23 eV).[11]

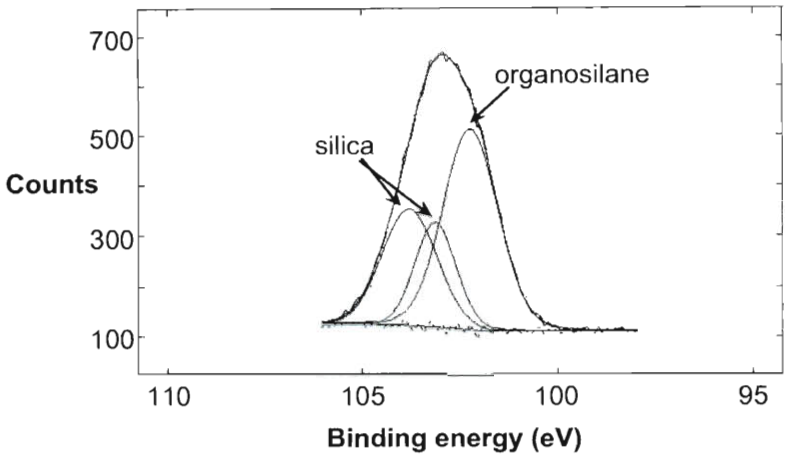


**Figure 2.3.** High resolution Si2p XPS of ODS-$SiO_2$-VGCF showing the presence of both silica (103.13 and 103.79 eV) and organosilane substituent (102.23 eV).

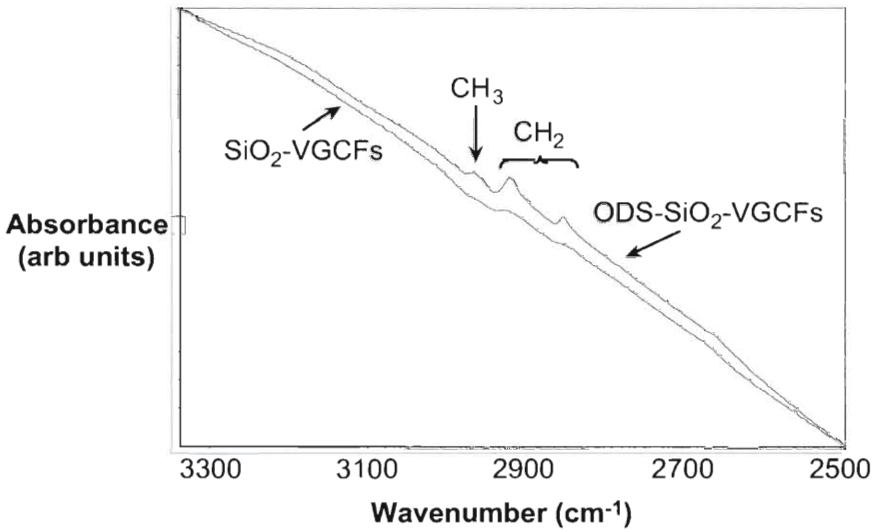


**Figure 2.4.** IR spectra of $SiO_2$-VGCF and ODS-$SiO_2$-VGCF showing the presence of aliphatic $\nu_{C\text{-}H}$ bands due to the octadecyl substituents.

In addition, the FT-IR spectroscopy (Figure 2.4) shows peaks representative of the stretching modes for the $CH_3$ (2962 $cm^{-1}$) and $CH_2$ (2917 and 2849 $cm^{-1}$) groups from the ODS.[12]

The addition of 1 wt.% (as compared to guar) of each of the three samples was compared to a baseline guar gel. In each case 41.6% of boric acid was used as a cross-linking agent and the pH was adjusted to 8.6, and the effect of each additive on the complex viscosity ($\eta^*$) was determined (Figure 2.5).

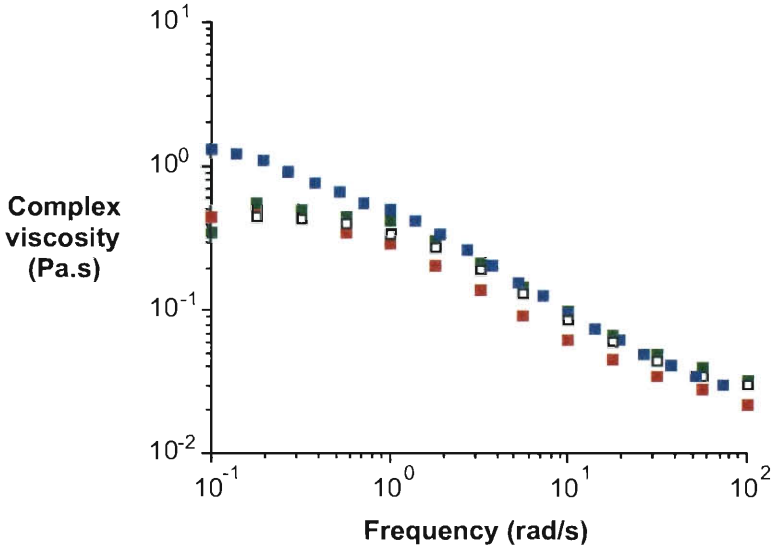


**Figure 2.5.** Viscosity with respect to frequency for boric acid cross-linked guar gel (▫) in comparison with boric acid cross-linked guar gel with 1 wt% (compared to guar) of unfunctionalized VGCFs (■), $SiO_2$-VGCFs (■), and ODS-$SiO_2$-VGCF (■). All measurements were taken at pH = 8.6.

The addition of plain VGCFs alters the slope of the viscosity vs. frequency curve of the guar gels, suggesting that the plain VGCFs might be having a networking effect with the guar polymer chains. However, it should also be noted that the unfunctionalized VGCFs show a propensity to agglomeration within the guar gel. In contrast, the presence of $SiO_2$-VGCF lowers the viscosity of the guar gels as

compared to the VGCF-free case. This decrease in viscosity could be attributed to two possible factors: 1) the hydroxyl groups on the guar chain binding directly to the $SiO_2$ coatings on the VGCF in competition with the borate ions, and 2) the borate ions get adsorbed onto the surface of the $SiO_2$-VGCF, thereby preventing the cross-linking between the borate ions and the guar chains by lowering the available borate.

**Table 2.1.** XPS spectra analysis of $SiO_2$-VGCF after reaction with boric acid.

| pH | C% | O% | B% | Si% | Na% |
|---|---|---|---|---|---|
| 8.6 | 65.9 | 24.8 | 2.4 | 6.9 | 0.1 |
| 9.3 | 68.2 | 25.8 | 1.3 | 4.1 | 0.6 |
| 10.3 | 61.0 | 28.7 | 4.4 | 1.9 | 4.0 |

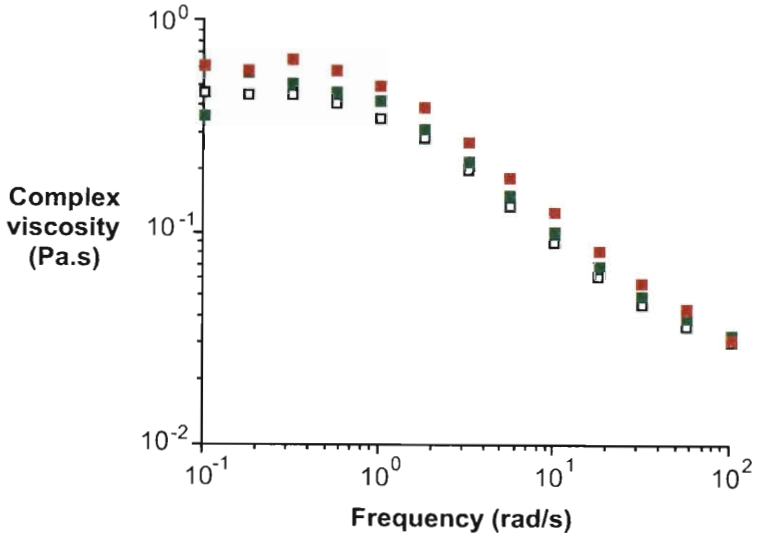


**Figure 2.6.** Viscosity with respect to frequency for boric acid cross-linked guar gel (▫) in comparison with boric acid cross-linked guar gel with 1 wt% (■) and 2 wt% (■) of ODS-$SiO_2$-VGCF. All measurements were taken at pH = 8.6.

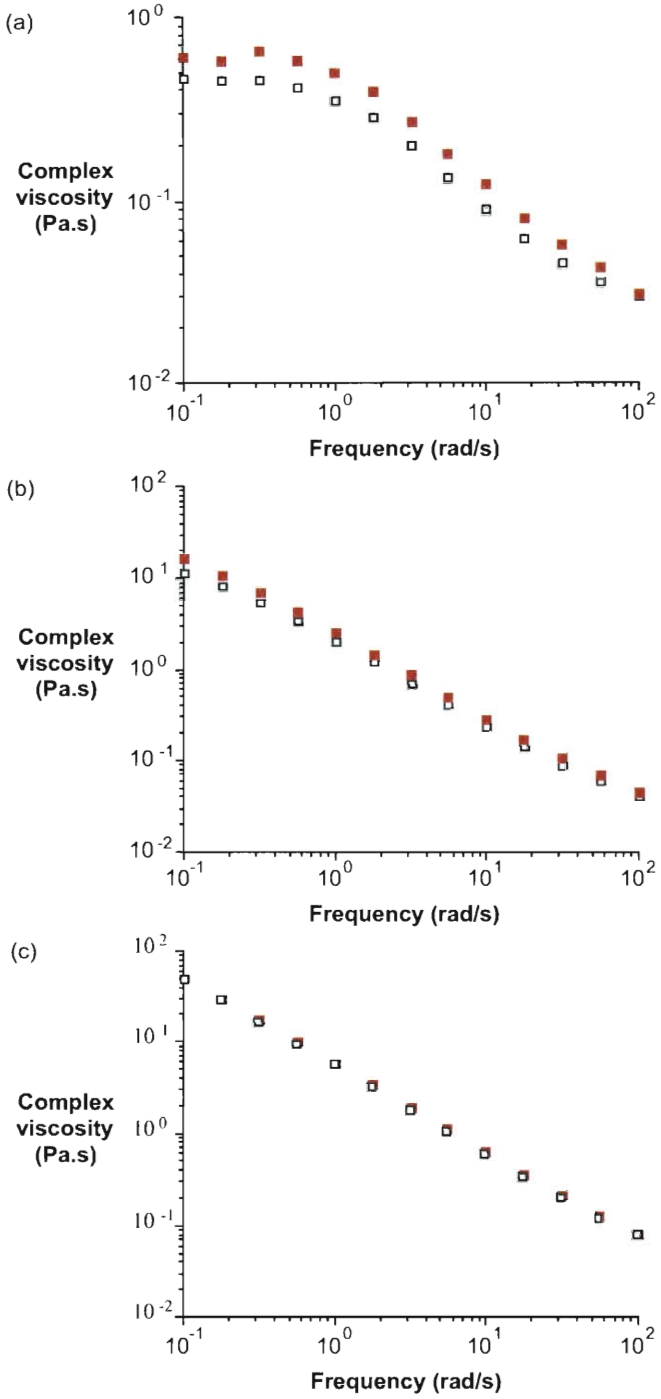


**Figure 2.7.** Viscosity with respect to frequency at pH = 8.6 (a), 9.3 (b), and 10.3 (c) for boric acid cross-linked guar gel (▫) in comparison with boric acid cross-linked guar gel with 2 wt% of ODS-$SiO_2$-VGCF (■).

In order to determine the possible interaction of boric acid/borate with the $SiO_2$-VGCFs, the two components were reacted in the absence of guar under similar conditions to that of the gel formation (see Experimental). The $SiO_2$-VGCFs were isolated and subjected to XPS analysis. Table 2.1 shows that the absorption of boron occurs at pH 8.6. Thus, the concentration of boric acid/borate available for guar cross-linking is decreased with a concomitant drop in the viscosity. There is also an increased absorption of both boron and sodium with increased pH.

The reaction of $SiO_2$-VGCFs with ODS appears to block any significant boron absorption onto the silica surface, since the addition of ODS-$SiO_2$-VGCFs (1 wt.%) maintains the same viscosity curve as plain guar gels (Figure 2.5). Increasing the concentration of ODS-$SiO_2$-VGCFs (2 wt.%) results in the maintenance of the curve, but a slight increase in viscosity (Figure 2.6). Thus, for all other tests, the addition of $SiO_2$-VGCF-octadecyltrichlorosilane to guar gels is maintained at 2 wt.%.

The effects of $SiO_2$-VGCF-ODS on complex viscosity ($\eta^*$) are shown in Figure 2.7. At pH 8.3 (Figure 2.7a), the effect of fiber content on viscosity is more pronounced than at higher pHs (Figure 2.7b and c), where the difference between guar gels with and without tubes decreases with increasing pH. This is probably because at a lower pH, the concentration of borate ions is low, forming fewer cross-links with the guar chains.[13] Thus, at lower pH, the interaction of guar chains with the ODS-$SiO_2$-VGCFs is more apparent, resulting in an increase in the complex viscosity. At pH 10.3 (Figure 2.7c), the effect of the ODS-$SiO_2$-VGCFs is barely noticeable; presumably it is outweighed by the cross-linking effects of the borate. Another observation made in Figure 2.7a is that the effect of the ODS-$SiO_2$-VGCF is higher at lower frequencies, and the difference in viscosity decreases with increasing frequency. This behavior is in accordance with other composites that are reinforced with fibers. All the gels exhibit a shear thinning effect with an increase in frequency; however, given that there is no change in the slope with addition of the functionalized

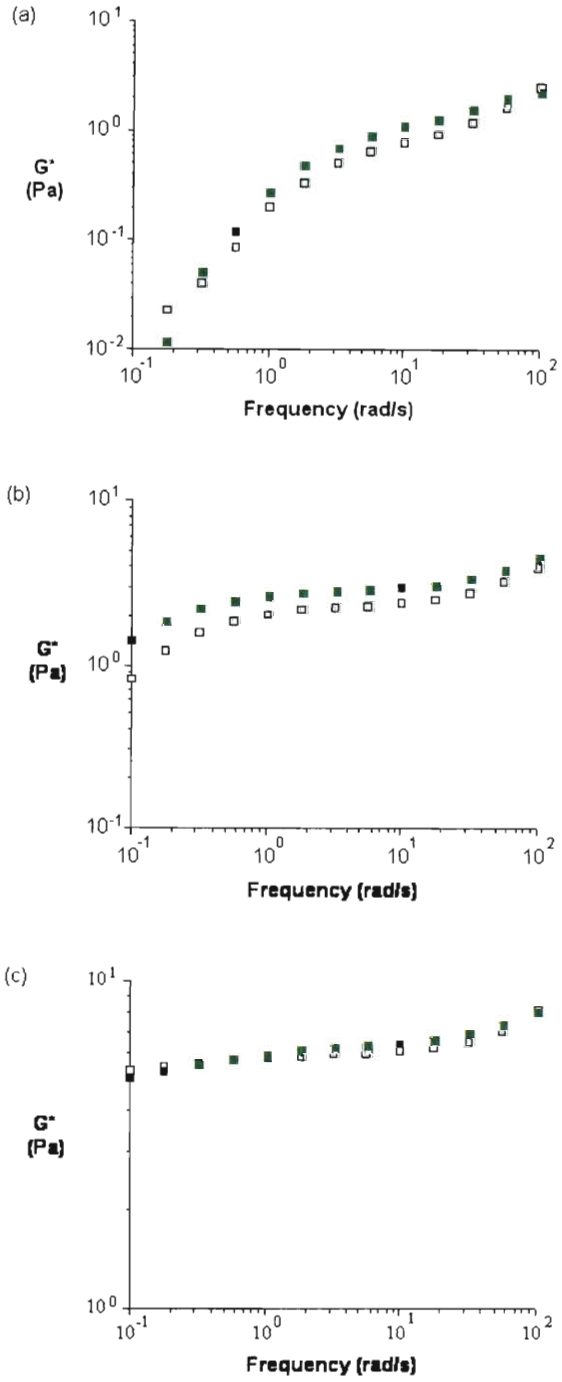


**Figure 2.8.** Storage modulus with respect to frequency at pH 8.6 (a), 9.3 (b), and 10.3 (c) for boric acid cross-linked guar gel (□) in comparison with boric acid cross-linked guar gel with 2 wt% of ODS-$SiO_2$-VGCF (■).

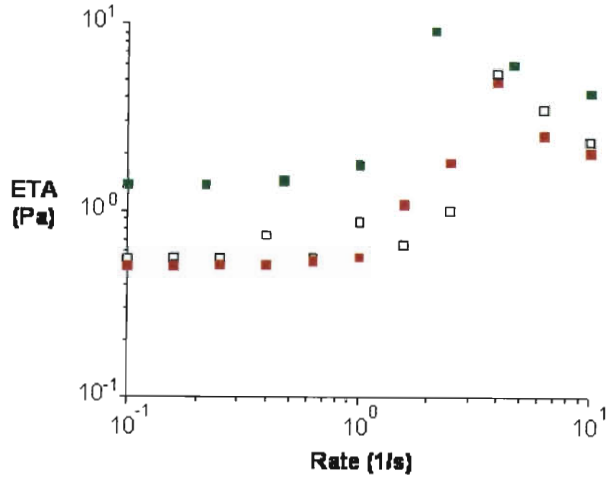


**Figure 2.9.** Viscosity with respect to shear rate at pH 8.6 for boric acid cross-linked guar gel (▫) in comparison with boric acid cross-linked guar gel with 1 wt% of $SiO_2$-VGCF (■) and ODS-$SiO_2$-VGCF (■).

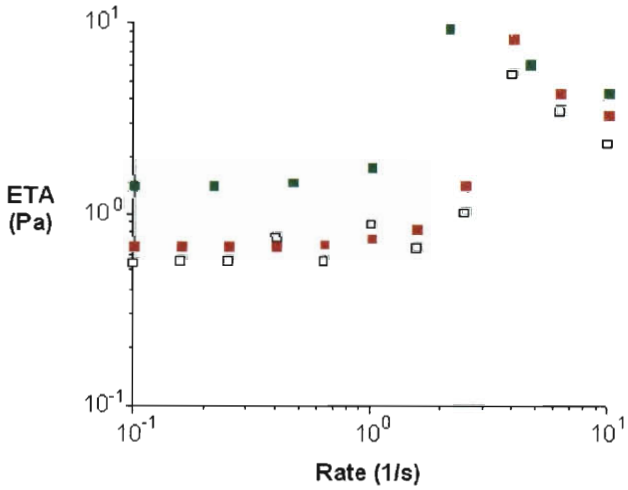


**Figure 2.10.** Viscosity with respect to shear rate at pH 8.6 for boric acid cross-linked guar gel (▫) in comparison with boric acid cross-linked guar gel with 1 wt% of ODS-$SiO_2$-VGCF (■) and 2 wt% ODS-$SiO_2$-VGCF (■).

fibers but only a slight increase in viscosity, it allows one to conclude that the addition of 2 wt.% of ODS-$SiO_2$-VGCF has more of a bundling effect with the guar polymer and a very little, if any, networking effect.[14]

Cross-linking guar polymer in the presence of a base and water creates a guar gel, which (as noted in the Introduction) is then used as a fluid, to both initiate fracture and to carry the proppant. Once the fracture is created underground and the proppant is placed, the guar gels are broken down to a less viscous form and pulled back from the reservoir to the surface. If the cross-linking is inefficient, then it takes a lot more acid to break down the gels which can have adverse effects to the environment and the cost of production.[15] Therefore, it is important to ensure that the presence of any additive or sensor does not alter the cross-linking or the gel structure of the guar. In order to gain insight into any alteration of gel structure or cross-linking, dynamic oscillatory measurements are made on guar gels to better understand their viscous and/or elastic properties. Viscous properties are explained by the loss modulus (G") and the elastic properties are explained by the storage modulus (G'). Figure 2.8 shows the affect of the addition of functionalized fibers on the storage modulus (G') of guar gels at different pH. Generally speaking, gels tend to exhibit a G' which is independent of frequency, while viscoelastic fluids show a G' that is increasing with frequency. Gel point is usually observed when a change in slope of G' versus frequency curve occurs.[16] At pH 8.6 and pH 9.3, the presence of ODS-$SiO_2$-VGCF increases the G' slightly, but maintains the same curves as those exhibited by guar gels without any VGCFs. This shows that the viscoelastic behavior of guar gels is maintained at lower pH. At pH 10.3, the behavior is that of a gel for both guar gels with and without VGCFs. Therefore, the presence of ODS-$SiO_2$-VGCF does not alter the structure and the cross-links of the guar gel.

Studies were also performed to test for any permanent damage that occurs to the gels with the presence of ODS-$SiO_2$-VGCF. For this, the gels were forward and reverse

sheared at different shear rates under static tests. Figure 2.9 exhibits the behavior of gels with and without the presence of $SiO_2$-VGCF and $SiO_2$-ODS-VGCF where there is an increase in viscosity of gels (shear thickening), followed by a decrease in viscosity (shear thinning) with increasing shear rates. Kjoniksen et al.[17] explain this initial increase in viscosity as the shear thickening effect which takes place when there is shear induced reorganization of the polymer association network; the shearing allows for the stretching and the alignment of chains, forming a stronger network association. The shear thinning effect then takes place at higher shear rates, when the networks are breaking faster than their rate of formation. Figure 2.10 shows a slight increase in viscosity with 2 wt.% ODS-$SiO_2$-VGCF at pH 8.3.

For pH 9.3 and 10.3, reverse shear rate studies are also conducted to understand if any permanent damage has occurred to the gels present with ODS-$SiO_2$-VGCF. It was difficult to get accurate results for reverse shear on gels at pH 8.6, as they constantly kept drying. Silicone oil was applied to edges of the parallel plates to prevent the water from evaporation, but the gel continued to dry up during the reverse shear for gels at pH 8.6.

Figure 2.11a clearly shows a slight increase in viscosity with 2 wt.% ODS-$SiO_2$-VGCF at pH 9.3. Reverse shearing of the gels at pH 9.3 shows higher viscosity at low shear rates and similar viscosity at high shear rates. This behavior is similar for gels both with and without the ODS-$SiO_2$-VGCF. Figure 2.11b show gels at pH 10.3 with the presence of ODS-$SiO_2$-VGCF exhibit a slightly higher viscosity than the gels without the tubes. Reverse shearing on these gels also shows a slight increase in the viscosity of the reverse sheared material. This is because during reverse shear, the broken networks are reforming on aligned and stretched chains, thereby increasing the viscosity during reverse shear.[18]

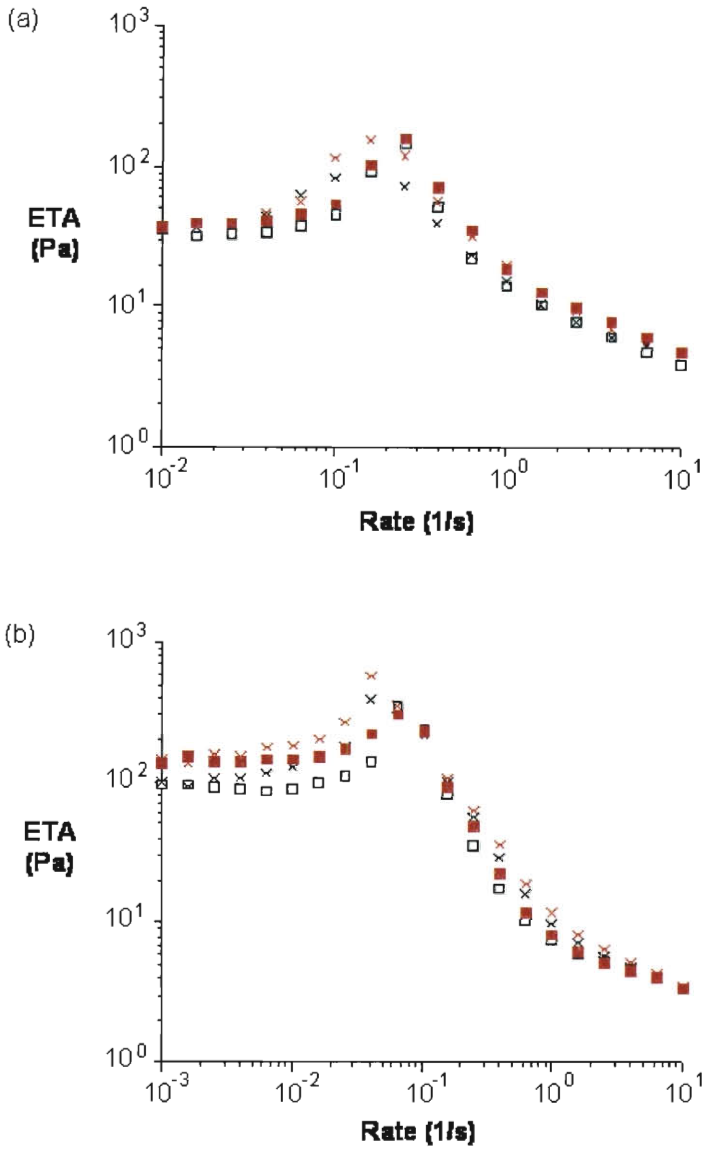


**Figure 2.11.** Viscosity with respect to forward and reverse shear rates at pH 9.3 (a) and 10.3 (b) for boric acid cross-linked guar gel (forward, ▫ and reverse, ×) in comparison with boric acid cross-linked guar gel with 2 wt% of ODS-$SiO_2$-VGCF (forward ■ and reverse ×).

## Conclusions

Our goal of this research was to gain an understanding of whether the addition of a nanomaterial to a fracturing fluid will alter in a predictable manner the properties of the fluid. For a nano-based downhole sensor it is necessary that the sensor be transported in a manner that is compatible with present technologies. In the present study we have shown that in the case of borate cross-linked guar fracturing fluids, any nano material that has the potential for reacting with the boric acid/borate will significantly lower the viscosity of the guar gel. This means that it will be important that any proposed oxide nanoparticles be surface functionalized in order to minimize boric acid/borate absorption.

The addition of the ODS-$SiO_2$-VGCF to the guar gels exhibits an interaction with the gels only at a lower pH than typically used for fracturing fluids. While, the presence of ODS-$SiO_2$-VGCF minimally increases the storage modulus of the guar gels, and under shear-induced conditions, gels which contain ODS $SiO_2$-VGCF behave similarly to the plain guar gels, displaying no permanent damage to the gels under the applied shear. Thus, it can be concluded that with a presence of 2 wt% of ODS-$SiO_2$-VGCF in the guar gels, the behavior of the gels is quite similar to that of the plain guar gels.

In summary, we have shown that as long as the nanostructured material is compatible with a fracturing fluid such as guar it may be used without adverse effects on the main function of the fracturing fluid. This is only one of the two issues that confront the use of nanotechnology downhole. The second is whether the surface chemistry of the nanostructure is compatible with the reservoir mineral, i.e., can the nanostructure be transported without undue adhesion? We are at present investigating this component of the problem, and the results of this study will be presented elsewhere.

## Experimental

VGCFs, fluorosilicic acid ($H_2SiF_6$), fumed silica ($SiO_2$), ethanol, methanol, nitric acid, and Millipore Express PLUS Membranes are obtained from the same sources as Chapter 1. Method to coat VGCFs with silica is the same as Chapter 1.

Octadecyltrichlorosilane (ODS), boric acid, and sodium hydroxide (NaOH, pellets) were obtained commercially (Sigma-Aldrich), and were used without any further purification. Guar gum (Halliburton WG-35) was used without any further purification. Rheological measurements are made using an ARES (Advanced Rheometric Expansion System) strain-controlled rheometer (Rheometric Scientific, now TA Instruments). Data is collected using 50 mm diameter parallel plates for the dynamic and steady tests.

**Synthesis of ODS-$SiO_2$-VGCFs.** The reaction of ODS with $SiO_2$ is a variation from a previously known method.[19] ODS (40 mg, 90% pure) was added to dry toluene (35 mL) in a round bottom flask under inert atmosphere. To this mixture was added $SiO_2$-VGCF (22 mg). The mixture was sonicated for 30 sec. before setting it for reflux for 24 hours.[9] The functionalized $SiO_2$-VGCFs (ODS-$SiO_2$-VGCFs) were filtered using PTFE filters (0.20 μm) and washed with copious amounts of EtOH and acetone. The ODS-$SiO_2$-VGCFs were then allowed to dry overnight in a desiccator.

**Reaction of $SiO_2$-VGCFs with boric acid.** $SiO_2$-VGCFs (6 mg) was added to DI water (100 mL) and was blended in a commercial blender. A solution of NaOH (0.2 M) was added dropwise to adjust to the desired pH to 8.6, 9.3, or 10.3. After the addition of NaOH solution, the mixture in the blender was blended for 90 s, followed by filtration and drying.

**Formation of guar hydrogels.** Guar gum (300 mg) was added to DI water (100 mL) and was blended in commercial blender. To this, boric acid (125 mg) was added and blended. Separately, where appropriate, a sample of $SiO_2$-VGCF or ODS-$SiO_2$-VGCFs (2 wt.% of guar, 6 mg) was added to DI water (25 mL) and was blended. A solution of NaOH (0.2 M) was added drop wise to adjust to the desired pH (8.6, 9.3, or 10.3). After the addition of NaOH solution, the mixture was blended for 90 s to form into a hydrogel. The hydrogel was collected in a plastic cup for rheometric testing.

## References


1. (a) R. J. Powell and J. M Terracina, *Borate Crosslinked Fluids*. Halliburton, Duncan, OK, 1998 (b) R. Schechter. *Oil Well Stimulation*. Prentice-Hall Inc., Englewood Cliffs, NJ, 1992.
2. G. C. Maitland, Oil and gas production. *Curr. Opin. Colloid. Interface. Sci.*, 2000, **5**, 301.
3. A. Tayal, R. M. Kelly, and S. A. Khan, *Macromolecules*, 1999, **32**, 294.
4. J. Gulbis, *Drilling and Pumping J.*, 1988, **7**, 4.
5. *Evaluation of Impacts to Underground Sources of Drinking Water by Hydraulic Fracturing of Coalbed Methane Reservoirs*. Environmental Protection Agency, Washington, DC, June 2004.
6. H. R. Jafry, E. A. Whitsitt, and A. R. Barron, *J. Mater. Sci.*, 2007, **42**, 7381.
7. A. Ulaman, *Adv. Mater.*, 1990, **2**, 573.
8. A. R. Barron, D. J. Flood, and A. A. Guzelian, *US Patent* 7491376 (2009).
9. M. R. Kallury, *Langmuir*, 1992, **8**, 947.
10. E. A. Whitsitt and A. R. Barron, *Nano Lett.*, 2003, **3**, 775.

11. J. F. Moulder, W. F. Stickle, P. E. Sobol, and K. D. Bomben, *Handbook of X-ray Photoelectron Spectroscopy*. Perkin-Elmer Group, Eden Prairie, MN, 1995.

12. S. A. Mirji, *Surf. Interface. Anal.*, 2006, **38**, 158.

13. M. Bishop, N. Shahid, J. Yang, and A. R. Barron, *Dalton Trans.*, 2004, **17**, 2621.

14. P. Potschke, T. D. Fornes, and D. R. Paul, *Polymer*, 2002, **43**, 3247.

15. N. Goel, S. N. Shah, and B. P. Grady, *J. Pet. Sci. Eng.*, 2002, **35**, 59.

16. C. Lei and P. E. Clark, *Society of Petroleum Engineers Conference (SPE Conference)*, 2004, 90840.

17. A. Kjoniksen, N. Beheshti, H. K. Kotlar, K. Zhu, and B. Nystrom, *Eur. Polym. J.* 2008, **44**, 959.

18. N. Beheshti, K. Zhu, A. Kjoniksen, and B. Nystrom, *J. Non-Cryst. Solids*, 2007, **353**, 3906.

19. S. A. Kulkarni, S. A. Mirji, A. B. Mandale, and K. P. Vijayamohanan, *Thin Solid Films*, 2006, **496**, 420.

# Chapter 3

# Role of Silica in Titania Coatings and Photocatalysis

## Introduction

The use of titania ($TiO_2$) in general, and $TiO_2$ nanoparticles in particular, as a photocatalyst is extensively documented,[1,2] and the theory behind their activity is relatively well understood.[3] Recently, interest has been focused upon the use as materials for cleaning up water and air pollutants.[4,5] As such, it is desirable to develop catalysts of greater activity and potentially specificity, and to meet this goal we have undertaken an investigation of composite or hybrid structures.

The highly hydrophobic nature of carbon nanotubes (CNTs) coupled with their nano structure, and the potential for their electronic activity (i.e., as a semiconductor), makes them a potentially important catalyst substrate.[6,7] This idea has prompted several studies into methods for growing or mixing $TiO_2$ with single walled carbon nanotubes (SWNTs), multi walled carbon nanotubes (MWNTs) and graphene,[8,9,10,11] including studies of the photocatalytic activity of the $TiO_2$-CNT hybrid on the degradation of organic dyes and pollutants.[12] Previous work has shown that the presence of SWNTs or MWNTs in a $TiO_2$ matrix helps in increasing surface area of the $TiO_2$ allowing for more organic pollutants to come into contact with the surface of the $TiO_2$ particle and thus increase the rate of reaction. In addition, the presence of the SWNT or MWNT allows for the transfer of the photoexcited electron from the $TiO_2$ to the nanotube, thus slowing down the electron-hole recombination and making photocatalysis more efficient.[5,13]

Given our experience with coating carbon nanotubes (CNTs) with oxides,[14,15,16,17] chalcogenides,[18] and carbonates,[19] we are interested in determining whether single walled carbon nanotubes (SWNTs) can act as a scaffold for the $TiO_2$ particle growth and thus create an intimate hybrid material. In addition, we are interested in whether there is any

synergistic effect between the SWNT and $TiO_2$ with regard to catalytic activity. The first part of this chapter is based upon developing the methodology for growing $TiO_2$-SWNT hybrids, and determining their activity to the photocatalytic degradation of a model dye system: Congo red.

The inadequate treatment of drinking water currently remains as a significant source of pathogen transmission across the globe. In 2004 the WHO estimated that point of use chlorination of drinking water could prevent 39% of the 1.58 million deaths due to diarrhoeal disease attributed to unsafe water supply, sanitation, and poor hygiene.[20] While chlorination has generally proven very effective for virus inactivation in drinking water, it can form dangerous disinfection byproducts, especially in waters with high organic contents. UV disinfection processes have been increasingly utilized due to this, however some viruses are highly resistant and particle associated viruses may be shielded from UV radiation.[21] Advanced oxidation processes, and semiconductor based photocatalysis in particular, are alternative disinfection strategies that may provide adequate treatment while overcoming the problems associated with traditional disinfection methods. Titania is a suitable material for use in water treatment since it is non toxic when ingested and stable under environmental conditions.[22] Previous studies have shown synthesis of $TiO_2$ nanoparticles and thin films using methods such as liquid phase deposition, sol gel synthesis, electro deposition, and chemical vapor deposition.[3] Amongst the various shapes and forms of $TiO_2$ nanoparticles, $TiO_2$(P25) is the standard commercially available material with an approximate diameter of 30 nm and an average surface area of 49 $m^2/g$. The powder consists of 70% anatase phase and 30% rutile phase.[23] Owing to its high surface area and mixed phase, photocatalytic studies have been performed on $TiO_2$(P25), including the decomposition of organic pollutants and materials.[8,24,25]

Upon excitation and charge separation, $TiO_2$ can generate several reactive oxygen species (ROS), the most significant being the hydroxyl radical ($HO^{\cdot}$),[26] which is a

powerful oxidant that is typically responsible for contaminant degradation by catalyzed $TiO_2$. ROS scavengers can be included in reaction systems to elucidate the ROS responsible for degrading a particular contaminant.

One limitation of $TiO_2$ is its high rate of charge recombination, and thus reduced photocatalytic efficiency. Several dopants and supports have been studied for improving the photocatalytic efficiency of $TiO_2$. During a broader study in the effect of carbon nanomaterials on the inactivation of viruses in water systems by $TiO_2$, we discovered that the surface treatment of $TiO_2$(P25) with a range of silica sources allows for the simple enhancement of the activity of $TiO_2$(P25) for the degradation of organic molecules. Therefore, the second part of this chapter focuses on the treatments performed on the $TiO_2$(P25) nanoparticles and its affects on photocatalysis of viruses.

## Results and Discussion

**Growth of $TiO_2$ on SWNTs** Our initial starting point was to replicate the synthesis of Zeng and co-workers[13] in coating SWNTs with $TiO_2$. The formation of $TiO_2$ is based upon the hydrolysis of titanium tetrafluoride (Eq. 3.1).

$$TiF_4 + 2\ H_2O \rightarrow TiO_2 + 4\ HF \qquad (3.1)$$

Unsurfacted purified SWNT were placed in a polypropylene (PP) reaction vessel in DI water with $TiF_4$. However, TEM analysis of $TiO_2$ growth on SWNTs for 21 h. (Figure 3.1a) shows incomplete growth with significant portions of the SWNTs still exposed. This is very different from the growth achieved previously,[13] where they reported complete coverage of the SWNT with $TiO_2$ in only 20 h. In fact, in our hands the reaction needed to proceed for 48 h. in order to obtain complete coverage of the SWNTs by $TiO_2$ (see Figure 3.1b). Upon further investigation, we discovered that while, based upon our

prior experiences with HF generating reactions,[17] we had used a polypropylene reaction vessel, Zeng and co-workers[13] had used a glass beaker. We therefore repeated the reaction using a glass beaker. As may be seen from the TEM images in Figure 3.2, it takes almost half the time to achieve the $TiO_2$ coverage on SWNTs using a glass beaker, compared to that of a polypropylene beaker (i.e., Figure 3.1a versus Figure 3.2a).

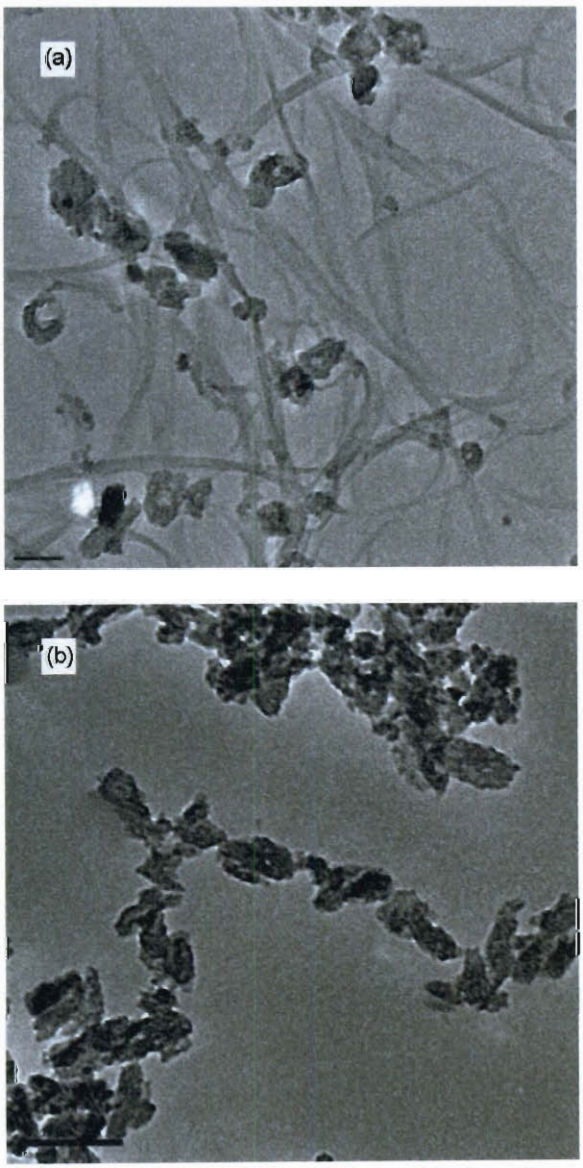


**Figure 3.1.** TEM image of (a) $TiO_2$-SWNT-PP-21 (scale = 50 nm) and (b) $TiO_2$-SWNT-PP-48 (scale = 0.1 μm).

The well-connected growth of $TiO_2$ on the SWNTs was previously attributed to the formation of nanoscopic HF bubbles that were trapped onto the $TiO_2$ crystallites.[13] It was proposed that this solid-gas interface prevented the $TiO_2$ crystallites from growing above a certain size by terminating the supply of $TiF_4$ to the crystal surface. As a consequence new growth must take takes place at any available solid-liquid interface (i.e., the uncoated SWNT surface) resulting in a connected mesocrytalline growth. Based upon our results of growth in a polypropylene beaker this explanation cannot be true, since the same nanoscopic HF bubbles would be present in our system. An alternative explanation must be developed.

XPS analysis (Table 3.1) of the $TiO_2$-SWNT-glass samples shows the presence of detectable amounts of silicon (<1%) not observed in the $TiO_2$-SWNT-PP samples. Since it is well known that HF will etch silicon and silica glass,[27] and based on Eq. 3.1, it is clear that the HF in the $TiO_2$ growth solution could be responsible for the inclusion of silicon into the $TiO_2$-SWNT-glass samples. Previous studies on $TiO_2$ nanoparticles doped by metals or metal oxides have shown a change in the growth of the $TiO_2$ crystals. For example, the addition of niobium to a $TiO_2$ growth solution inhibits the process of nucleation and growth of $TiO_2$ crystallites.[28] Other studies have shown that the presence of $SiO_2$ in the growth solution decreases the size of the $TiO_2$ nanoparticle by reducing the nucleation sites on the grain boundary, thus preventing the $TiO_2$ particles from aggregating and growing too big.[25,29,30] It has also previously been described that the presence of $SiO_2$ in a $TiO_2$ nanoparticle creates Lewis acid sites,[31] which under heat treatment or irradiation form hydroxyl radicals, which slow the growth of the $TiO_2$ grain.[32]

Based upon these results we propose that the formation of well-connected growth of $TiO_2$ on the SWNTs is not a function of "nanoscopic HF bubbles", but the incorporation of small quantities of silica into the $TiO_2$ as a consequence of the etching of

the glass container during the reaction. This silicon is involved in limiting the growth of the $TiO_2$ crystals, and hence promoting the coverage of the SWNT by $TiO_2$.

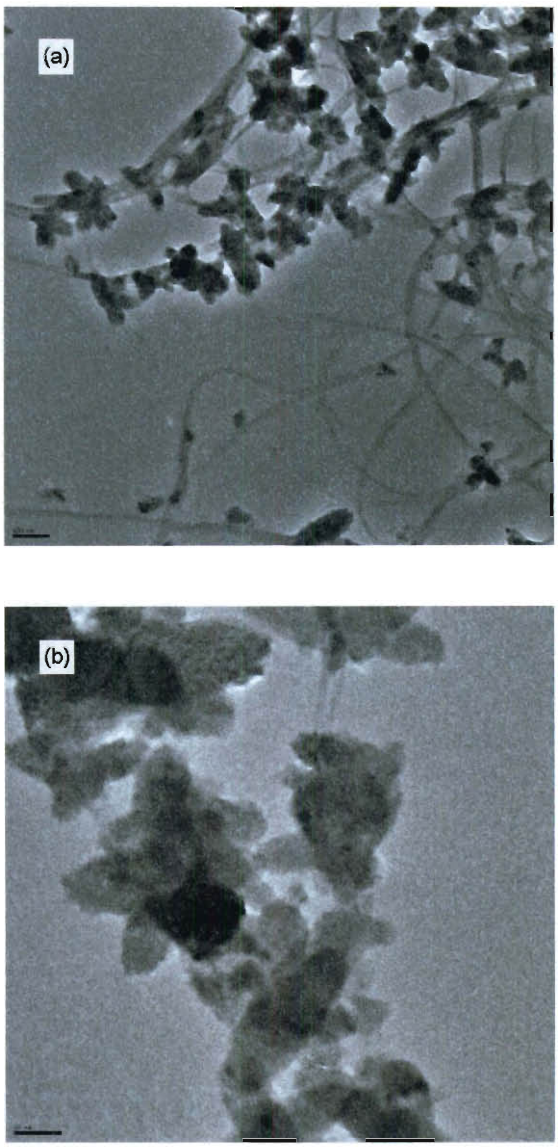


**Figure 3.2.** TEM images of (a) $TiO_2$-SWNT-glass-21 (scale = 100 nm) and (b) $TiO_2$-SWNT-glass-10 (scale = 50 nm).

**Table 3.1** XPS analysis (%) for $TiO_2$-coated SWNTs.

| Sample | C | O | Ti | Si |
|---|---|---|---|---|
| $TiO_2$-SWNT-PP-21 | 79.4 | 15.1 | 5.1 | - |
| $TiO_2$-SWNT-glass-21 | 78.8 | 16.5 | 4.7 | <0.1 |
| $TiO_2$-SWNT-$SiO_2$-21 | 68.4 | 23.7 | 7.7 | 0.2 |

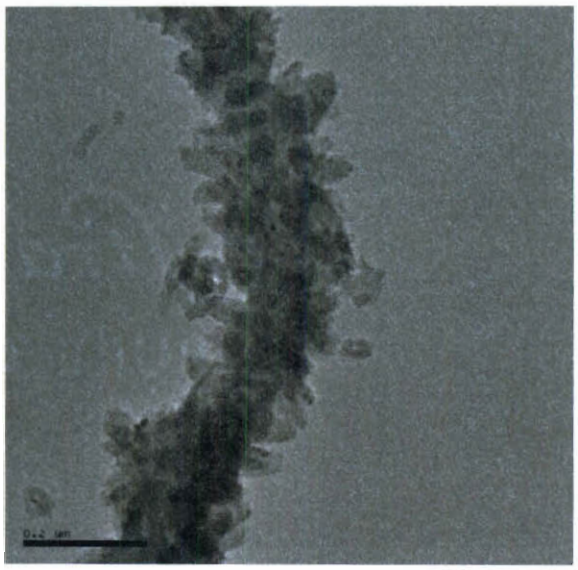

**Figure 3.3.** TEM image of $TiO_2$-SWNT-$SiO_2$-21 (scale = 0.2 μm).

In order to further understand the role of $SiO_2$ in the growth of $TiO_2$ on SWNTs, we added fumed $SiO_2$ into the $TiO_2$ growth solution. The TEM image of the resulting material ($TiO_2$-SWNT-$SiO_2$) is shown in Figure 3.3. As can be observed, the SWNT substrate is covered with smaller but many more $TiO_2$ particles, giving complete coverage of the SWNT. This is in contrast to the image shown in Figure 3.1a. In fact, the

coverage for the reaction with added $SiO_2$ is even greater than an equivalent reaction time in glass. Thus, for any given set of reaction conditions, the greater the silicon content (Table 3.1) the greater the coverage of the SWNT by $TiO_2$. We believe this demonstrates the idea that the silica plays an important part in controlling the relative rates of grain growth and new growth of $TiO_2$ on SWNTs.

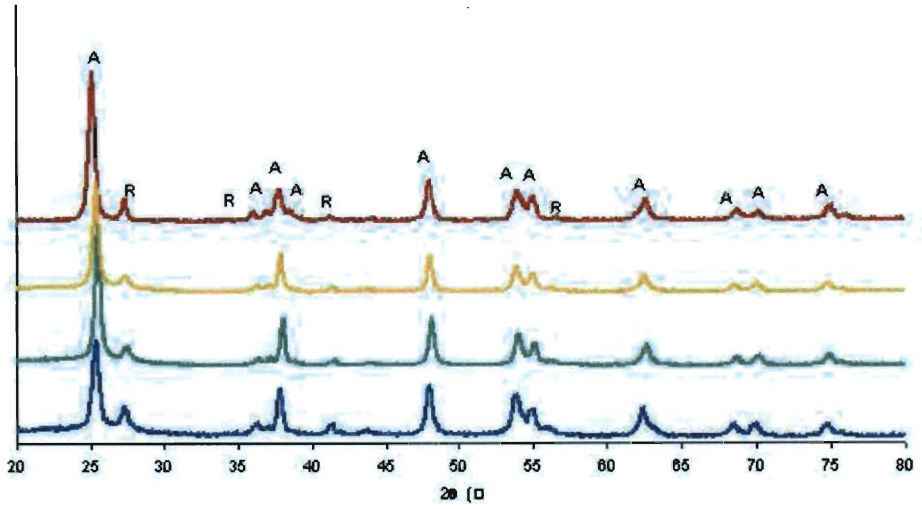


**Figure 3.4.** XRD showing the anatase (A) and rutile (R) phases commercial $TiO_2$(P25) (——) as compared to $TiO_2$-SWNT-PP-21 (——), $TiO_2$-SWNT-glass-21 (——), and $TiO_2$-SWNT-$SiO_2$-21 (——).

Figure 3.4 shows the XRD data for the different phases of $TiO_2$ formed on the $TiO_2$-SWNT-PP, $TiO_2$-SWNT-glass, and $TiO_2$-SWNT-$SiO_2$ as compared to $TiO_2$(P25), a commercially available $TiO_2$ nanoparticle of known high photoreactivity.[24] The XRD data confirms the presence and formation of both anatase and rutile phases for the as grown $TiO_2$. However, it is interesting to note that the anatase:rutile ratio is dependant on

the amount of silica present. The $TiO_2$ for $TiO_2$-SWNT-PP and $TiO_2$-SWNT-glass is slightly richer in anatase than found in $TiO_2$(P25), while $TiO_2$-SWNT-$SiO_2$ has much less anatase than found in $TiO_2$(P25).

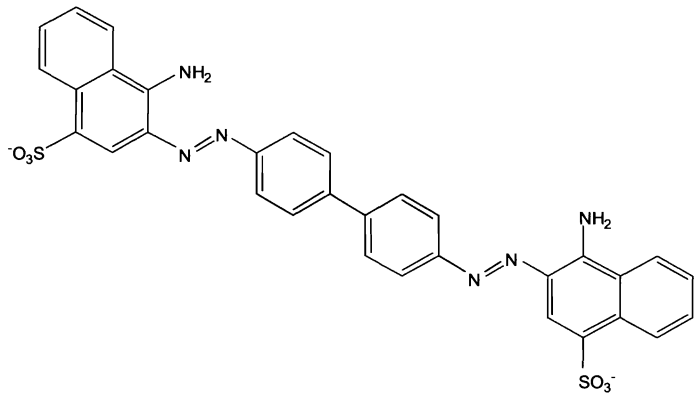


**Figure 3.5.** Chemical structure of Congo red dye.

**Adsorption of Congo red.** Congo red (Figure 3.5) is a polycyclic aromatic hydrocarbon dye that is commonly used as a model for photocatalytic degradation studies. We have previously found that in studying the degradation of Congo red it is important to determine the adsorption in the dark to provide an accurate initial concentration ($C_0$) for the photocatalytic measurements. This is particularly important given that the polycyclic aromatic structure of Congo red promotes strong $\pi$-$\pi$ stacking interaction with SWNTs, giving rise to high adsorptive removal. Thus, the percent removal of Congo red after 1 hour dark stiring was measured using an initial dye concentration 150 mg/L and a catalyst concentration of either 500 mg/L or 250 mg/L.

As is shown in Figure 3.6 $TiO_2$-SWNT-PP-21 and $TiO_2$-SWNT-PP-48 both show significantly greater adsorption as compared to $TiO_2$(P25), with the greatest adsorption being associated with the lower coverage of the SWNT. The low coverage $TiO_2$-SWNT-glass-10 shows almost total adsorption (Figure 3.6) as do unfunctionalized SWNTs. Given the huge adsorption of the dye on $TiO_2$-SWNT-glass-10 sample using 500 mg/L

catalyst, it would be impossible to test for catalysis as all the dye would be adsorbed onto the catalyst, making it difficult to measure the degradation of the dye left in solution. Therefore, a low concentration (250 mg/L) was used for further tests on the $TiO_2$-SWNT-glass samples and the raw SWNTs (Figure. 3.7).

At a 250 mg/L catalyst concentration, the $TiO_2$-SWNT-glass materials still had significant adsorption of Congo red; however, once again the lower adsorption for $TiO_2$-SWNT-glass-48 as compared to $TiO_2$-SWNT-glass-21 indicates that complete coverage with $TiO_2$ can reduce the absorbance capacity.

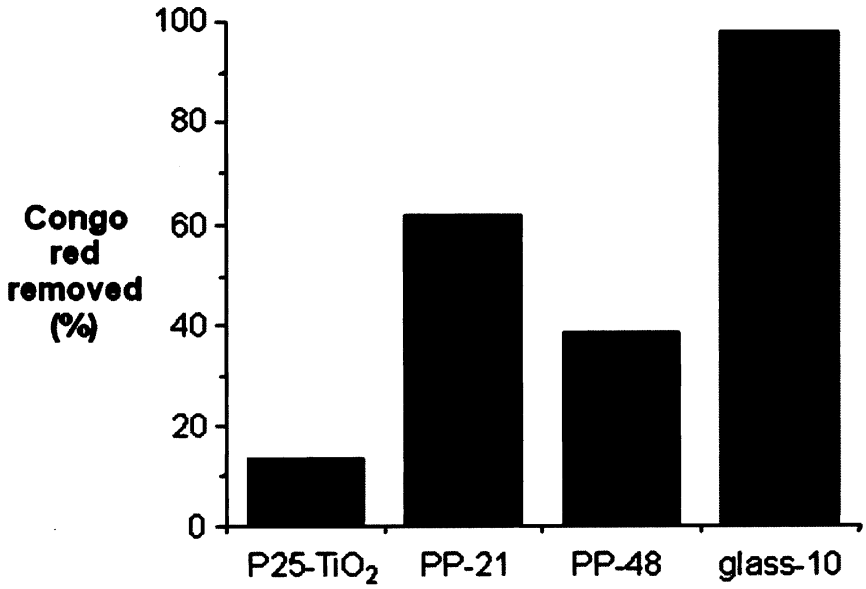


**Figure 3.6.** Percent removal of Congo red after 1 hour dark stiring by $TiO_2$(P25), $TiO_2$-SWNTs-PP-21 (PP-21), $TiO_2$-SWNTs-PP-48 (PP-48), and $TiO_2$-SWNTs-glass-10 (glass-10) with a catalyst concentration of 500 mg/L and an initial dye concentration 250 mg/L.

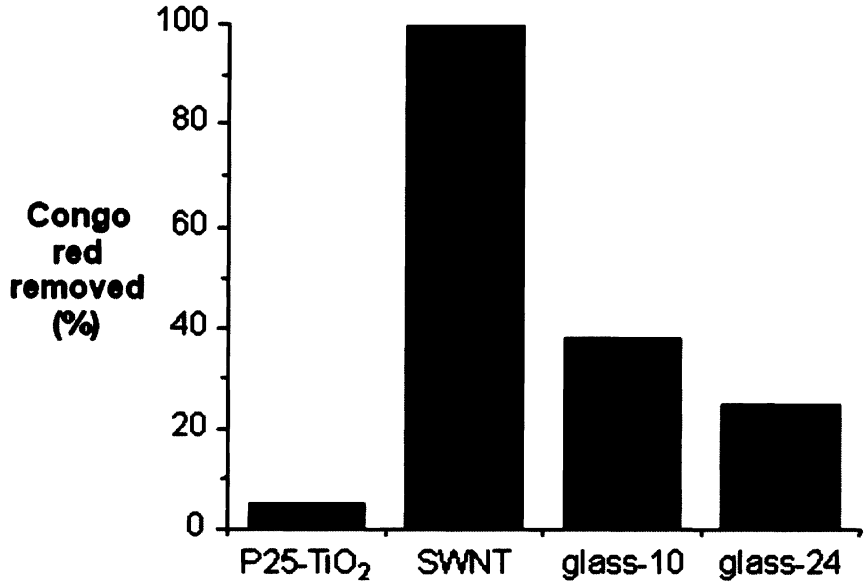


**Figure 3.7.** Percent removal of Congo red after 1 hour dark stiring by $TiO_2$(P25), SWNTs, $TiO_2$-SWNTs-glass-10 (glass-10), and $TiO_2$-SWNTs-glass-21 (glass-21) with a catalyst concentration of 250 mg/L and an initial dye concentration 150 mg/L.

**Photocatalytic decomposition of Congo red.** The photocatalytic decomposition of Congo red was studied for the different hybrid materials in comparison with $TiO_2$(P25). In each case the samples were stirred in the dark (1 hr for $TiO_2$-SWNT-PP samples and 21 hrs for $TiO_2$-SWNT-glass samples), and the initial concentration is defined as $C_0$, which is the concentration after dark stirring. The $C/C_0$ values were determined as a function of irradiation time.

A comparison of the photocatalytic activity of $TiO_2$-SWNT-PP-21 and $TiO_2$-SWNT-PP-48 is shown in Figure. 3.8. The $TiO_2$-SWNT-PP-21 material showed better catalysis than the $TiO_2$-SWNT-PP-48 material, indicating that complete coverage of the tubes by $TiO_2$ does not result in enhanced photocatalysis. For the first 80 min. of the reaction time, the catalytic results for the $TiO_2$-SWNT-PP-21 sample were similar to that of $TiO_2$(P25) nanoparticles tested at the equivalent $TiO_2$ concentration (134 mg/L).

However, after 80 min. the dye degradation by $TiO_2$-SWNT-PP-21 material proceeded faster than the degradation by $TiO_2$(P25), i.e., 82% of the dye was removed from solution after 165 min. of reaction by the $TiO_2$-SWNT-PP-21 versus only 57% removed by $TiO_2$(P25) after 175 min. reaction time. We propose that this increase in activity with time is associated with the strong binding of the Congo red reagent to the exposed SWNT.

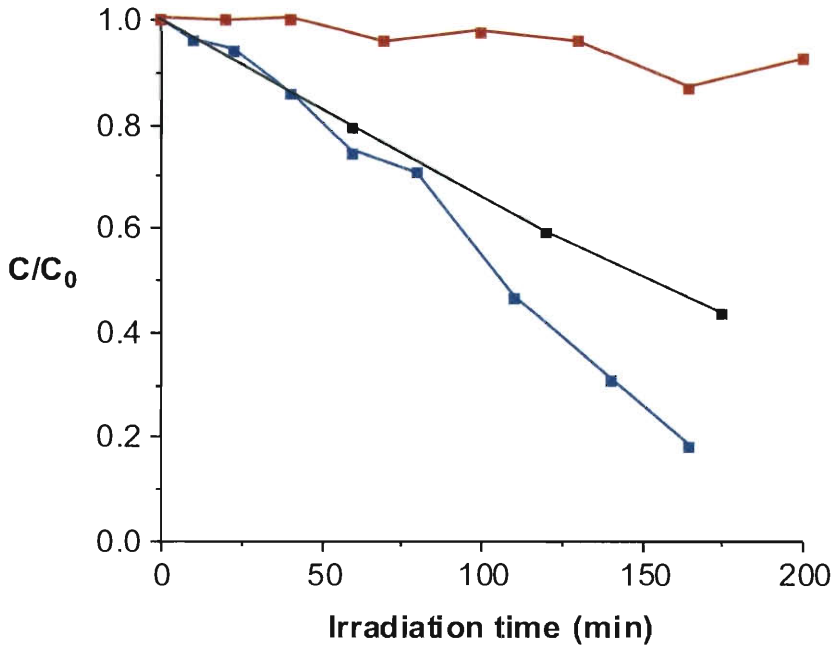


**Figure 3.8.** Normalized photocatalytic degradation of Congo red by $TiO_2$-SWNTs-PP-21 (■), $TiO_2$-SWNTs-PP-48 (■) and $TiO_2$(P25) (■). $C_0$ is the dye concentration after dark stirring.

While the $TiO_2$-SWNT-glass was found to strongly adsorb Congo red from solution, the material possessed limited to no photocatalytic activity for this particular dye (Figure. 3.9), whereas $TiO_2$(P25) tested as a comparison was found to degrade 34% of the dye after 220 min irradiation. It is especially surprising that the materials made in glass demonstrates no photocatalytic activity, especially when XRD analysis (Figure 3.4)

confirms that the $TiO_2$ exists mostly as anatase and rutile, which are both photoactive crystalline phases. This result is especially surprising when considering that several other studies have shown enhanced catalysis by $TiO_2$ when coated onto CNTs.[13,33,34,35] Furthermore, studies have shown that doping $TiO_2$ nanoparticles with silicon or zirconium enhances the photocatalysis.[36] It is possible that, with such strong absorbance to the catalyst, the dye was being degraded on the catalyst surface and not desorbed back into solution. In this way the free dye concentration would not change in solution but the concentration on the particle surface would decrease.

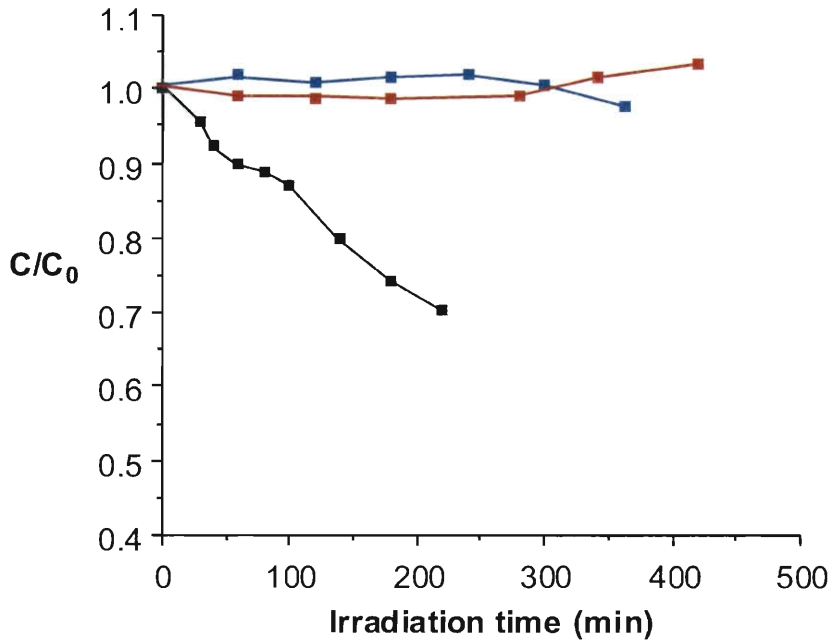


**Figure 3.9.** Normalized photocatalytic degradation of Congo red by $TiO_2$-SWNTs-glass-10 (■), $TiO_2$-SWNTs-glass-21 (■), and $TiO_2$(P25) (■). $C_0$ is the dye concentration after dark stirring.

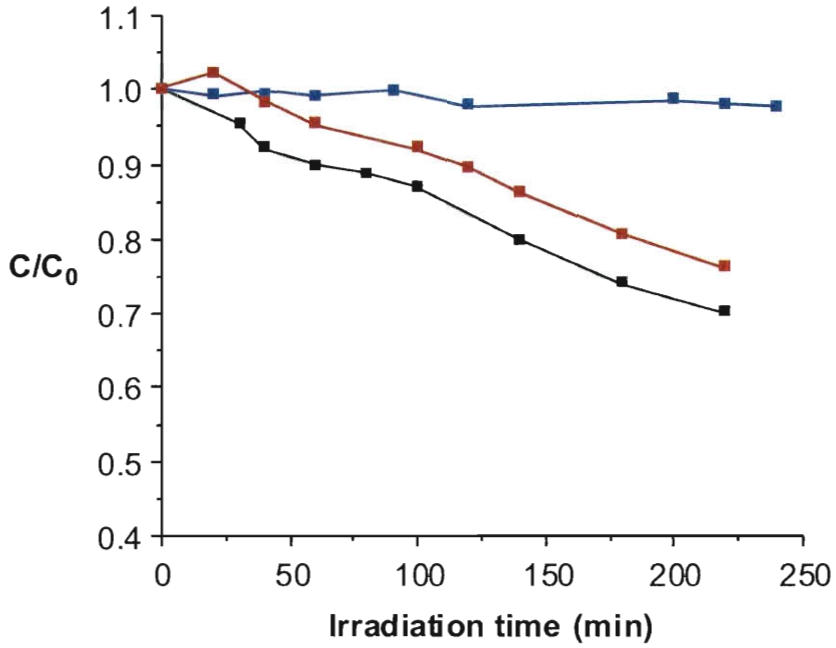


**Figure 3.10.** Normalized photocatalytic degradation of Congo red by a physical mixture of P25-$TiO_2$ with SWNTs (▪) or MWNTs (▪) in comparison with $TiO_2$(P25) (▪). $C_0$ is the dye concentration after dark stirring.

Since the SWNTs appeared to improve $TiO_2$ activity in one case ($TiO_2$-SWNT-PP-21) and decrease the $TiO_2$ activity in all other cases, we decided to investigate whether the presence of SWNTs or MWNTs in solution would hinder or enhance the photocatalytic removal of Congo red from solution by $TiO_2$(P25). As shown in Figure. 3.10, the presence of SWNTs was found to eliminate the photocatalytic activity of $TiO_2$(P25), while the presence of MWNTs slightly slowed the reaction as compared to $TiO_2$(P25) used without any CNTs. The small reduction when MWNTs are used may simply be due to a shielding of the UV radiation by the MWNTs, while the SWNTs likely inhibit $TiO_2$ photocatalysis by some other mechanism since the result is so much worse than with MWNTs.

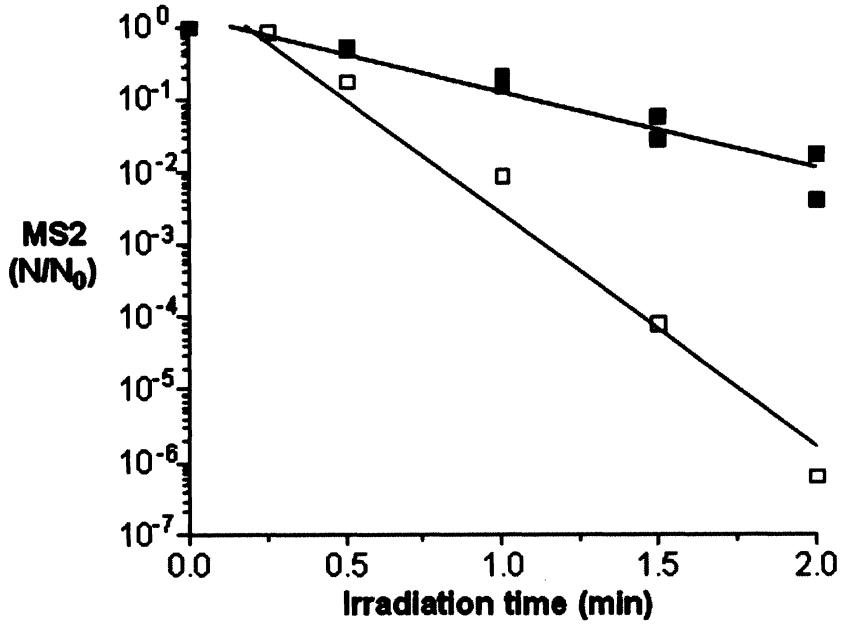


**Figure 3.11.** MS2 inactivation by untreated $TiO_2$(P25) (▪, $R^2$ = 0.935) and treated by refluxing in toluene with silicone grease sealing the glass apparatus (▫, $R^2$ = 0.971).

**Using $TiO_2$(P25) refluxed in toluene for the deactivation of bacteriophage.** As part of our preparation of making $TiO_2$ coated (SWNTs) to test for its role in inactivation of MS2, we made some $TiO_2$ powders as well to compare the catalytic activities of the $TiO_2$ coated SWNTs to the lab made $TiO_2$ powder and $TiO_2$(P25). Surprisingly, as may be seen from Figure 3.11, there is a marked difference in the inactivation of MS2 viruses using as received $TiO_2$(P25) and the sample that had been refluxed in toluene. Our prior experience with the extraction of silica ($SiO_2$) and low molecular weight silicon oxide species from commercial Dow Corning high vacuum silicon grease[37,38,39] suggested that a possible contaminant of silicon could result in the enhanced activity. XPS measurements indicated that any silicon species would be less that the detection limit, and TEM showed no alteration in the morphology of the $TiO_2$(P25) particles (see below). However, repeating the toluene reflux experiment using a non silicone-based grease (Krytox) for the glassware resulted in no significant alteration in the activity of the $TiO_2$(P25) (Figure

3.12). This suggest that the effect is due to the addition of silica (or some silicon-containing species) and not the toluene reflux. Therefore, the mixing of silica from the grease with the P25 powder had pronounced effects on deactivation of viruses.

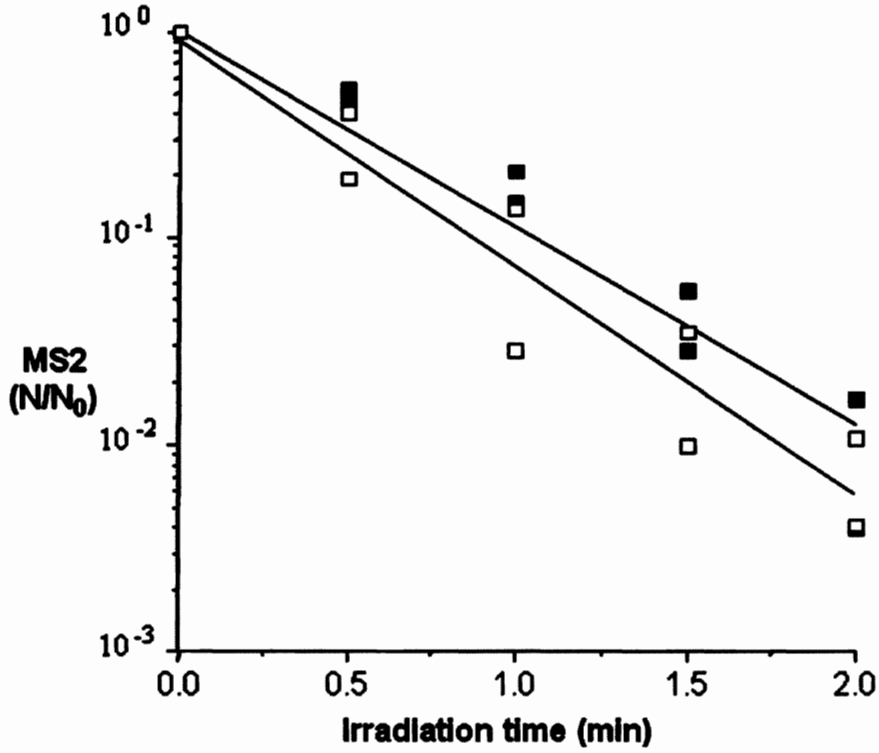


**Figure 3.12.** MS2 inactivation by untreated $TiO_2$(P25) (▪, $R^2$ = 0.935) and treated by refluxing in toluene with non-silicone (hydrocarbon-based) grease sealing the glass apparatus (▫, $R^2$ = 0.917).

As mentioned earlier, doping $TiO_2$ with metal oxides such as silica and zirconia ($ZrO_2$) has been used to enhance some of the properties of titania, such as band gap, photocatalysis, surface hydrophilicity, surface acidity, quantum effects and surface area. Silica doped with $TiO_2$ has many potential applications and the interactions have been studied extensively in the areas of quantum-sized effects on photocatalysis, acid catalysis on the surface, catalytic support materials, and photo induced hydrophilicity.[25,40,41]

Different methods of incorporation of $TiO_2$ doped with silica have been employed which include sol-gel synthesis, hydrosol synthesis, co-precipitation, flame hydrolysis, and physical mixing; however, in each case, the nanoparticles were made in the presence of silica, i.e., an in-situ process. In contrast, the pronounced effects we have observed suggests that the activity of $TiO_2$(P25) can be significantly improved by a simple and scalable surface reaction with a silicon species rather than in situ incorporation during synthesis.

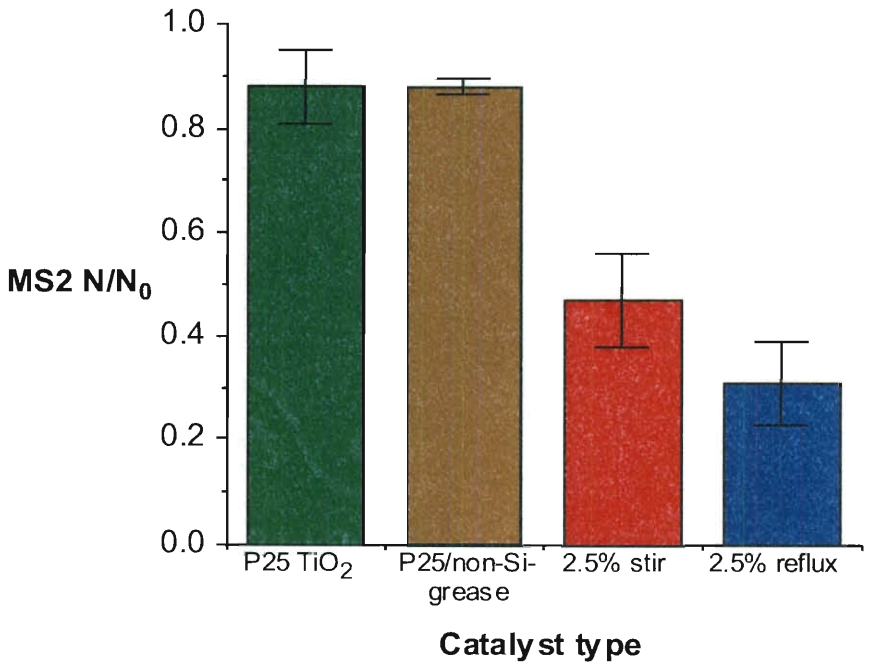


**Figure 3.13.** Adsorptive removal/dark inactivation of MS2 by $TiO_2$(P25) (■), $TiO_2$(P25) refluxing in toluene with non-silicone grease (■), and $TiO_2$(P25)-$SiO_2$ formed by stirring (■) or refluxing (■).

**Using $TiO_2$(P25) mixed with silica.** Given the pronounced effect that the silicone-based grease had on $TiO_2$(P25) (Figure 3.11), we decided to incorporate fumed

silica with $TiO_2$(P25) to test its effects on virus inactivation. Unlike previous studies,[25,31,42,43,44,45] our approach was to physically mix a suitable silica source with as-received $TiO_2$(P25) nanoparticles. Our previous results with silica coating of nanomaterials[14,15,17] suggested that fumed silica would be an appropriate source. Additionally, we were interested in whether there is a perceived difference between chemical reaction or physical coating. Thus, $TiO_2$(P25) was both stirred and refluxed with silica and the resulting materials tested for virus inactivation.

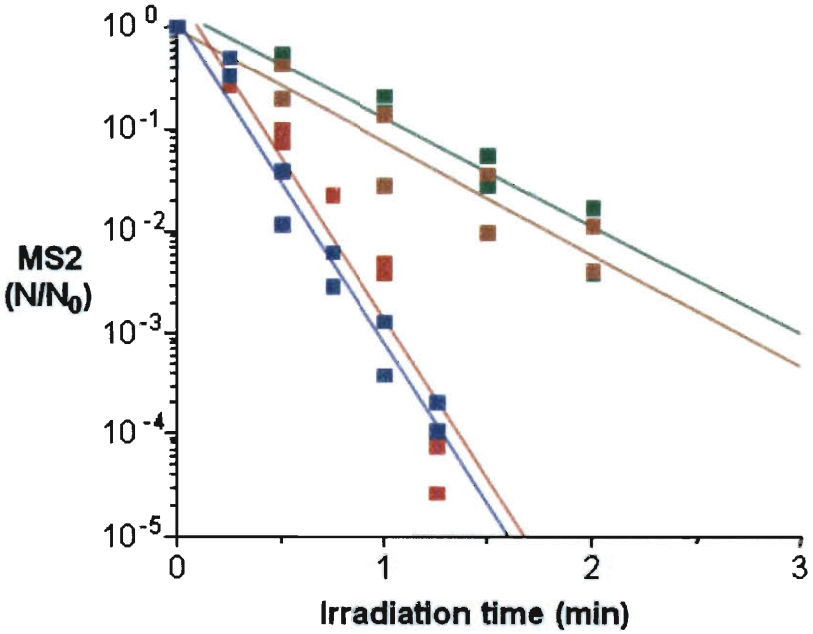


**Figure 3.14.** Photocatalytic inactivation of MS2 by $TiO_2$(P25) (■, $R^2 = 0.935$), $TiO_2$(P25) refluxing in toluene with non-silicone grease (■, $R^2 = 0.917$), and $TiO_2$(P25)-$SiO_2$ formed by stirring (■, $R^2 = 0.907$) or refluxing (■, $R^2 = 0.970$).

Before irradiation, the viruses and catalysts are mixed for 10 minutes in the dark to allow for adsorption to occur. Figure 3.13 shows that the adsorption of MS2 to $TiO_2$(P25)-$SiO_2$ is much greater than to untreated $TiO_2$(P25) or $TiO_2$(P25) refluxed in toluene (non-Si grease). Only 31% and 47% of the MS2 remained infective after the

addition of the refluxed or stirred $TiO_2$(P25)-$SiO_2$, respectively. 88% of the MS2 remained infective after mixing with $TiO_2$(P25) that was either untreated or refluxed in toluene (non-Si grease). This suggests that the addition of silica is responsible for the enhanced adsorption, and that any residual toluene remaining on the catalyst is not effecting adsorption/dark inactivation.

The photo catalytic inactivation of MS2 is also significantly enhanced by the addition of silica to $TiO_2$(P25). Figure 3.14 shows that both stirred and refluxed $TiO_2$(P25)-$SiO_2$ materials outperformed $TiO_2$(P25) powder. The rate constants for the stirred and refluxed $TiO_2$(P25)-$SiO_2$ materials was 2.8 and 3.1 $min^{-1}$, respectively, which are approximately 3 times greater than that for $TiO_2$(P25) which produced a rate constant of only 0.95 $min^{-1}$. The degradation results also show that both $TiO_2$(P25)-$SiO_2$ (stirred), and $TiO_2$(P25)-$SiO_2$ (refluxed) perform similarly in killing the viruses. Rate constants and correlation coefficients are shown for all materials in Table 3.2. UV-A radiation in the absence of catalyst did not inactivate the viruses over the time course of the experiments in this study.

The TEM images of stirred $TiO_2$(P25)-$SiO_2$ (Figure 3.15a) do not appear significantly changed from as-received $TiO_2$(P25) (Figure 3.15b). Nevertheless, XPS analysis performed on these powders confirms the presence of silicon (Table 3.3). The relatively high silicon content as determined by XPS (4.3%) as compared to the amount reacted (2.5 wt%) is consistent with the surface status of the silica. XPS confirmed the formation of chemical Si-O-Ti bond. The O1s spectra of stirred and refluxed $TiO_2$(P25)-$SiO_2$ (Figure 3.16) show additional peaks that may be assigned to Si-O-Si and Si-O-Ti units that are not present in the as-received $TiO_2$(P25). In addition, the $^{29}Si$ MAS NMR spectrum of a $TiO_2$(P25) sample refluxed with 5 wt.% fumed silica shows a broad signal typical of silica (Figure 3.17); however, $^{29}Si$ NMR cannot differentiate Si-O-Si versus Si-O-Ti.

**Table 3.2.** First order rate constants for MS2 inactivation [$Log(N/N_0) = -kt$].

| Material | k ($min^{-1}$) | $r^2$ |
|---|---|---|
| $TiO_2$(P25) | 0.95 | 0.92 |
| $TiO_2$(P25) refluxed with Si grease | 2.4 | 0.93 |
| $TiO_2$(P25) refluxed with non-Si grease | 1.1 | 0.92 |
| $TiO_2$(P25)-$SiO_2$ stirred | 2.8 | 0.89 |
| $TiO_2$(P25)-$SiO_2$ refluxed | 3.1 | 0.97 |

Previous literature studies have attributed the improvement in silica-doped $TiO_2$ photocatalysis to quantum confinement, increase in surface area, increase in surface acid sites, control in the grain boundary growth of the nanoparticles, and enhanced adsorption due to the presence of silica.[25,42-45] In our system, we can rule out any quantum effects as the $TiO_2$(P25) nanoparticles are purchased and not incorporated with silica in situ. In a similar manner we can rule out any increase in the surface area as a result of the reaction with the fumed silica. Table 3.4 shows BET results for as-received $TiO_2$(P25) and the various treated $TiO_2$(P25)-$SiO_2$ samples. It is clear that there is no significant difference in the surface area of $TiO_2$(P25) compared to samples of $TiO_2$(P25)-$SiO_2$. There are two possible alternative explanations for the enhanced photocatalytic inactivation of MS2 virus by the $TiO_2$(P25)-$SiO_2$ used in this study: enhanced adsorption characteristics and/or band gap changes.

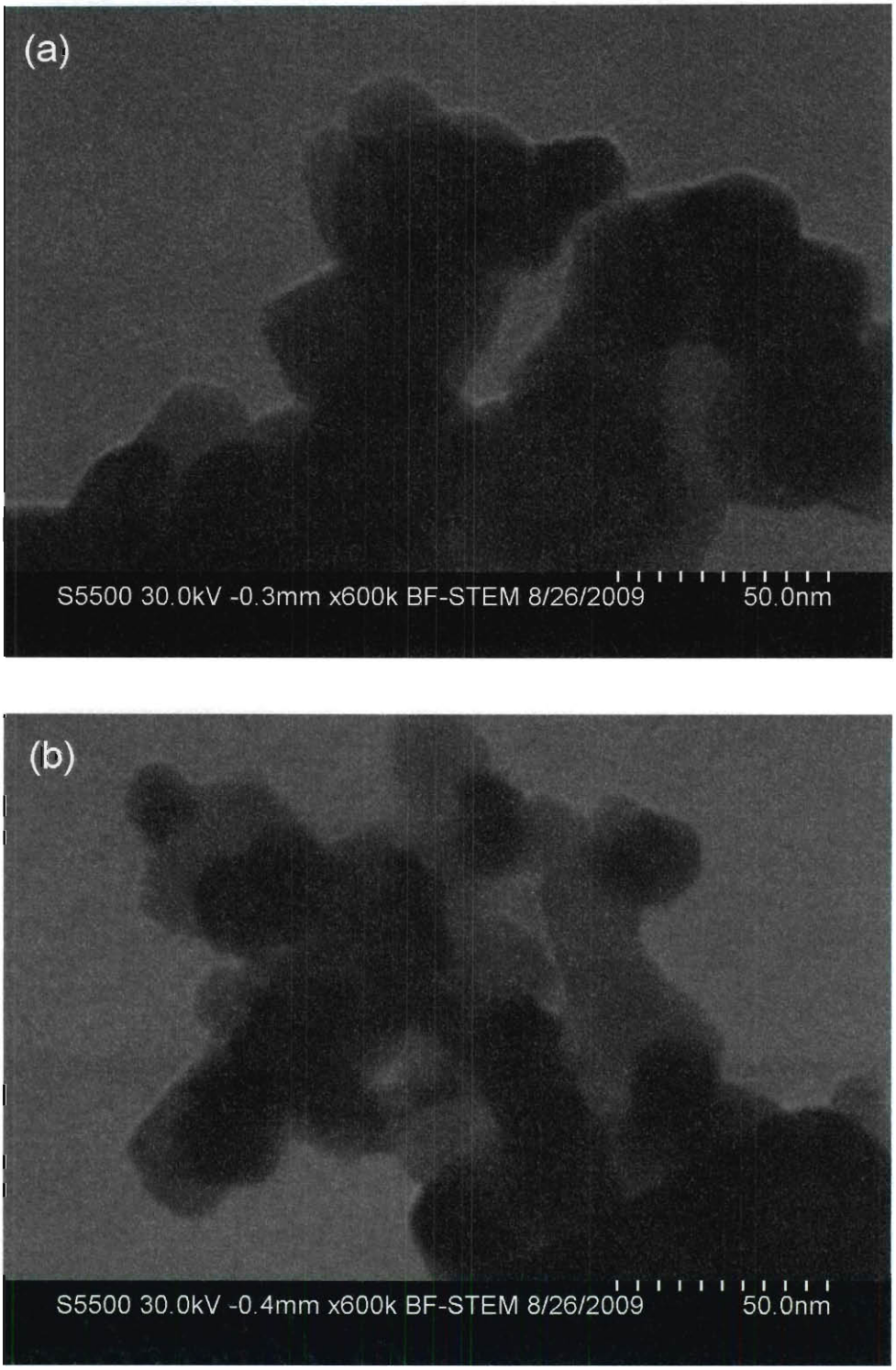


**Figure 3.15.** TEM of $TiO_2$(P25) reacted with fumed silica with (a) stirring in comparison with (b) as-received P25 $TiO_2$.

**Table 3.3.** XPS analysis of $TiO_2$(P25) and $TiO_2$(P25) refluxed and stirred with $SiO_2$.

| Sample | Ti (%) | O (%) | Si (%) |
|---|---|---|---|
| $TiO_2$(P25) | 32.5 | 67.5 | - |
| $TiO_2$(P25)-$SiO_2$(2.5%) stirred | 26.7 | 69.0 | 4.3 |
| $TiO_2$(P25)-$SiO_2$(2.5%) refluxed | 26.0 | 69.7 | 4.3 |

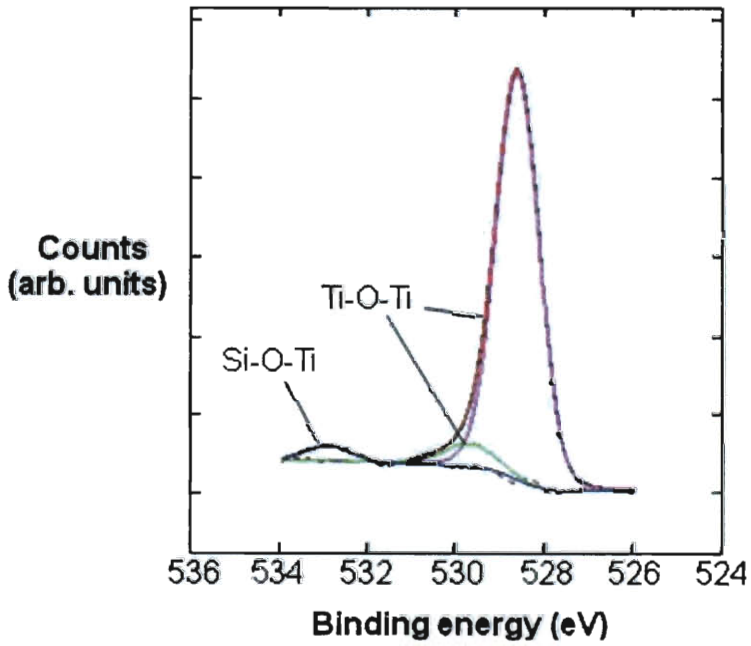


**Figure 3.16.** O1s X-ray photoelectron spectrum for $TiO_2$(P25)-$SiO_2$(2.5%) formed by refluxing $TiO_2$(P25) in toluene in the presence of silica.

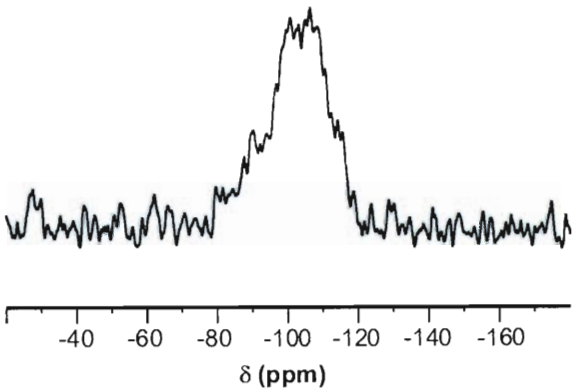


**Figure 3.17.** $^{29}$Si MAS NMR of $TiO_2$(P25)-$SiO_2$(5%). showing the presence of "$SiO_4$" coordination environment.

Previous studies have demonstrated that silicon-induced enhanced adsorption of substrate to $TiO_2$-$SiO_2$ hybrid particles is responsible for the increase in photocatalytic activity.[43,44] In this regard, a similar argument would suggest that the enhanced adsorption that we observe with the $TiO_2$(P25)-$SiO_2$ material is as a result of increased exposure to reactive oxygen species on the catalyst surface. Simple alcohols such as methanol are capable of scavenging hydroxyl free radical,[46] and as such mostly eliminates the virucidal capability of the catalyst. As shown in Figure 3.18 there is a significant difference in the activity of the $TiO_2$(P25)-$SiO_2$ samples in the presence of methanol, confirming that the generated $HO^{\cdot}$ is responsible for the antiviral action of this material. Thus, our $TiO_2$(P25)-$SiO_2$ either produces more $HO^{\cdot}$ than non silica-doped material, or the enhanced adsorption of MS2 to the catalyst results in greater exposure to the $HO^{\cdot}$, or both mechanisms may work in concert.

Silica doping of $TiO_2$ in this study has been found to affect the catalyst band gap. The UV-vis absorption curves for $TiO_2$(P25) and $TiO_2$(P25)-$SiO_2$ formed with differing amounts of fumed silica are shown in Figure 3.19. While it is difficult to see the blue shift between the $TiO_2$(P25) curve and the $TiO_2$(P25)-$SiO_2$(2.5 wt.%) and $TiO_2$(P25)-

$SiO_2$(10 wt.%), Figure 3.19 clearly shows a curve shift for $TiO_2$(P25)-$SiO_2$(20 wt.%). Using the UV-vis spectra, the band gap energies are calculated using Eq. 3.2 and shown in Table 3.5 As explained earlier, it is difficult to see the blue shift between the $TiO_2$(P25) curve and the $TiO_2$(P25)-$SiO_2$(2.5 wt.%) and $TiO_2$(P25)-$SiO_2$(10 wt.%); therefore, the derivative of the spectrum is analyzed, and the $\lambda$ value is defined as the wavelength where the absorption peak is rising most steeply. Anderson and co-workers[43,44] have suggested that the blue shift or increase in band gap energy is attributed to quantum size effects in conjunction with the interface interactions of $TiO_2$ formation in the presence of silica. They suggested that the presence of silica during the formation of the nanoparticles hinders the growth of the $TiO_2$ nanoparticle; thus, this smaller size $TiO_2$ nanoparticle creates a quantum effect and an increase in band gap energy. However, since in our studies the $TiO_2$(P25) is preformed and the particle size is unchanged, the observed effects cannot be due to silica control over titania particle size.

**Table 3.4.** BET surface area measurements.

| Sample | Surface Area ($m^2/g$) |
|---|---|
| $TiO_2$(P25) | 49.08 |
| $SiO_2$ (fumed) | 239.21 |
| $TiO_2$(P25)-$SiO_2$(2.5%) refluxed with Si grease | 37.73 |
| $TiO_2$(P25)-$SiO_2$(2.5%) refluxed without Si grease | 43.94 |
| $TiO_2$(P25)-$SiO_2$(2.5%) stirred | 78.79 |

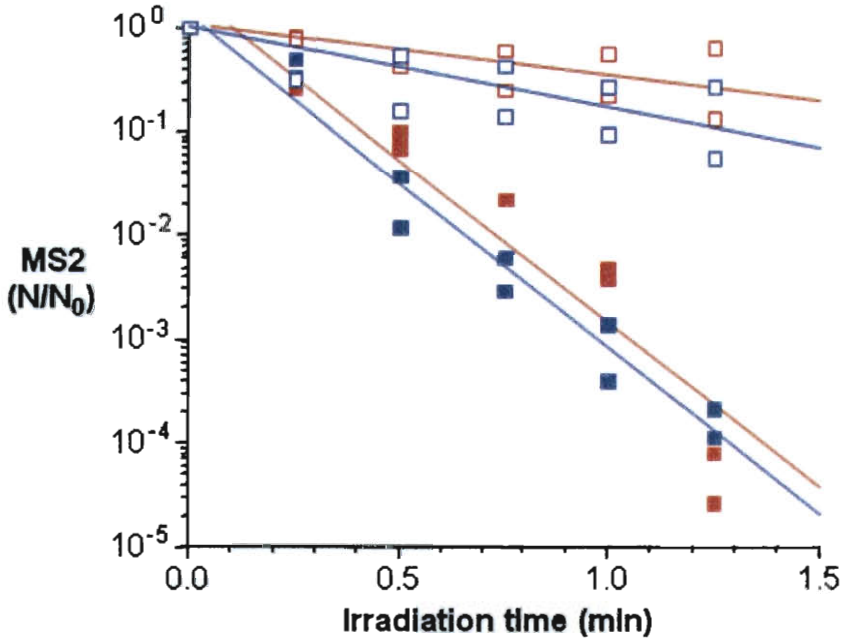


**Figure 3.18.** Photocatalytic inactivation of MS2 by $TiO_2$(P25)-$SiO_2$ formed by stirring (■, $R^2$ = 0.907) or refluxing (■, $R^2$ = 0.970) as compared to the values when run in the presence of methanol, a scavenger for hydroxyl free radical (□, $R^2$ = 0.479 and □, $R^2$ = 0.571, respectively)

An alternative mechanism was suggested by Periyat and co-workers, in which a change in the band gap energy is caused by the lowering of the valence band and a raising of the conduction band.[31] The result would be the reduction of the electron-hole recombination when $TiO_2$ is illuminated with UV light. We note that in these studies the synthesis was also an in-situ doping of silica that was thought to occur when the titania nanoparticle is formed. Irrespectively, in the present case, the band gap energy certainly appears to be changing or slowly increasing, which would reduce the electron-hole recombination. One explanation for this band gap increase may be due to the band bending which can occur at the interface of $TiO_2$(P25)-$SiO_2$. When the $SiO_2$ present on the surface of $TiO_2$(P25) comes into contact with $TiO_2$(P25), a potential is created across

the interface as the Fermi levels of both compounds try to equilibrate; this potential across the interface leads to band bending. This band bending may reduce the electron-hole recombination, thus allowing for efficient catalysis in our system. This effect occurs on pre-formed $TiO_2$(P25) nanoparticles that are subsequently chemically functionalized/coated.[22,47]

Therefore, in this study, we were able to achieve a slowly increasing change in band gap. This slow change in band gap along with other factors mentioned earlier, led to an efficient photocatalysis of viruses, without having to dope $TiO_2$ nanoparticles in situ with silicon.

$$E\ (eV) = 1239.95/\lambda\ (nm) \qquad (3.2)$$

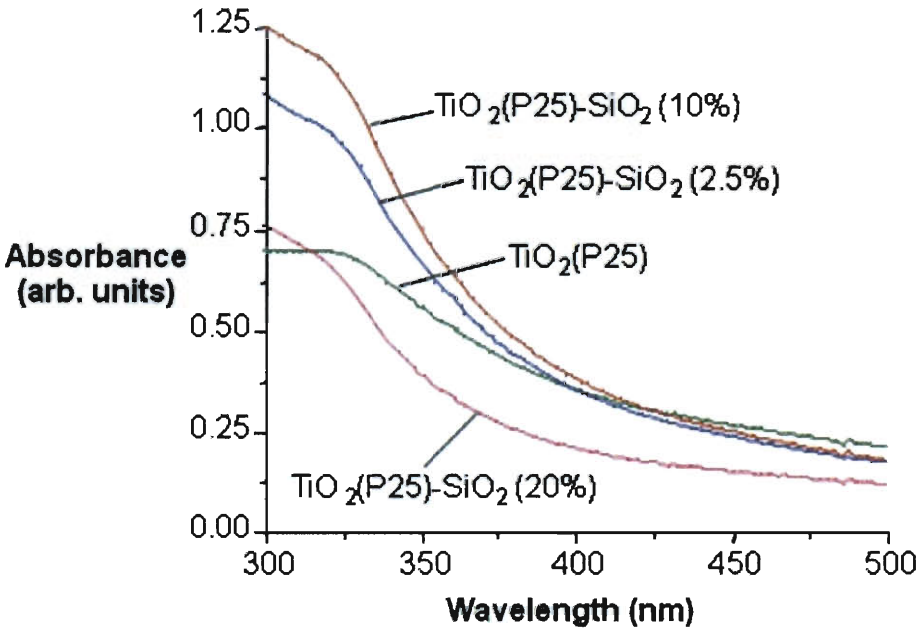


**Figure 3.19.** UV-vis absorbance curves for $TiO_2$(P25) (—) and $TiO_2$(P25)-$SiO_2$ formed with 2.5% (—), 10% (—) and 20% (—) $SiO_2$, respectively.

**Table 3.5.** Band gap calculations based on UV-vis absorbance spectrum.

| Sample | Calculated band gap (eV) |
|---|---|
| $TiO_2$(P25) | 3.42 |
| $TiO_2$(P25)-$SiO_2$(2.5%) | 3.43 |
| $TiO_2$(P25)-$SiO_2$(10%) | 3.45 |
| $TiO_2$(P25)-$SiO_2$(20%) | 3.47 |

## Conclusions

We have shown that SWNTs do act as templates for the growth of $TiO_2$. Unlike previously suggested, the important controlling factor for obtaining good coverage is not "nanoscopic HF bubbles", but rather the presence of silica. The silica is either sourced from the reaction vessel if made from glass or may be added in the form of fumed silica: the greater the silicon content the greater the coverage of the SWNT.

While the addition of silica promotes the complete coating of SWNT with $TiO_2$, the resulting materials show very high absorption of Congo red and essentially no catalytic activity. This is a surprise since $TiO_2$(P25)-$SiO_2$ has been shown to show significantly higher catalytic activity that $TiO_2$(P25) itself. Based upon the adsorption studies we propose a number of requirements in the present system. It is neceassary to have less than 70% initial absorption. Any higher absorption and the reactants and/or product are not desorped and no catalysis occurs. Nevertheless, it also appears necessary that less than full coverage of the SWNTs be attained. It is also worth noting that the highest activity occurs with the small average particle size. We have shown that intamate contact between the SWNT and the $TiO_2$ is needed (rather than a physical mixture) for

any catalysis, presumably since the SWNTs strongly absorb the Congo red and preclude further reaction. However, the electronic properties of the SWNTs (including semiconducting tubes) are clearly important since MWNTs appear to have little effect on altering the photocatalytic activity of $TiO_2$(P25).

The forgoing results indicate that while there is a synergy between $TiO_2$ and SWNTs with regard photocatalysis it is not always positive. In other words, under some conditions the presence of SWNTs inhibits catalysis, and it is only with certain structures (i.e., $TiO_2$-SWNT-PP-21) that the combination of materials shows an enhancement over the constituent parts. We are furthering our studies to determine whether such a dichotamy is a result of the strong hydrophobic interactions with the particular model system (Congo red) or a general feature of the composite structures.

We have demonstrated that improved photo-catalytic efficiency of commercial $TiO_2$(P25) for virus inactivation can be achieved by the addition of fumed silica, making it unnecessary to make $TiO_2$-$SiO_2$ nanoparticles via an in situ process. Secondly, the enhanced photocatalysis observed with the $TiO_2$(P25)-$SiO_2$ in this study is likely due to the greater adsorptive capacity of MS2 to the catalyst and/or changes in the material electronic properties, i.e., increase in band gap. The increased activity of this catalyst for virus inactivation makes it highly attractive alternative for use as a disinfectant. We finally note that our results offer an alternative view of previous "hybrid" $TiO_2$-$SiO_2$ systems.[25,42-45]

## Experimental

$TiO_2$(P25) (Degussa), fumed silica (Sigma-Aldrich), titanium tetrafluoride ($TiF_4$) (Sigma-Aldrich), EtOH (Decon Labs), MeOH (Decon Labs), toluene, acetone, and $Fe(acac)_3$ (Sigma-Aldrich), Congo red dye (MP Biomedicals, 85%), and MWNTs (Nanotech Innovations) were obtained from commercial sources and used without further

purification. HiPco SWNTs were grown at Rice University and were received as purified (96-97% purified, Batch HPR 181.1). PES syringe filters with a 0.45 μM-pore-size (Whatman) were pre-rinsed by filtering with DI water and purging with air. Unless stated all reactions were carried out in Nalgene® polypropylene (PP) labware. $TiO_2$(P25) was used without further purification as previous studies which use $TiO_2$(P25) or have modified $TiO_2$(P25) for enhanced photocatalysis have used no further purification of the as received material.[48] In this regard we wanted to ensure an equivalent comparison.

Branauer Emmett Teller (BET), X-Ray photoelectron spectroscopy (XPS), and transmission electron microscopy (TEM) are performed to test for surface area, chemical make up and structure of the nanopowder.

To indicate the different reaction vessels and reaction times, the following format is used to describe each sample: $TiO_2$-SWNT-glass-21 indicates a material prepared in a glass beaker over a reaction time of 21 h.

**$TiO_2$-SWNT-PP.** SWNTs (200 mg) and a solution of $TiF_4$ (0.04 M in DI $H_2O$) were placed in a polypropylene (PP) beaker. The beaker was covered with Parafilm secured with a rubber band, and a syringe is used to make a few pinholes to allow for any vapor to escape during heating. The beaker was placed in an oil bath and the mixture heated to 60 °C. After the allotted reaction time (21 or 48 h), the reaction mixture was centrifuged for 15 min. at 4400 rpm. After discarding the supernatant, the solid product was washed three times with EtOH:MeOH (90 mL, 4:1). The composition of the $TiO_2$-SWNT-PP reacted for 21 h. (i.e., $TiO_2$-SWNT-PP-21) was determined by XPS (Table 3.1).

**$TiO_2$-SWNT-glass.** Prepared using the same procedure as $TiO_2$-SWNT-PP, except for the use of a glass beaker, and using reaction times of 10 or 21 h. The

composition of the $TiO_2$-SWNT-glass reacted for 21 h. (i.e., $TiO_2$-SWNT-glass-21) was determined by XPS (Table 3.1).

**$TiO_2$-SWNT-$SiO_2$.** SWNTs (200 mg) and a solution of $TiF_4$ (0.04 M in DI $H_2O$) were placed in a polypropylene beaker. To this mixture, fumed silica (13 mg, 1 wt.% of $TiF_4$) was added. The beaker was covered with parafilm secured with a rubber band, and a few pinholes added to allow vapor to escape. The beaker was placed in an oil bath (60 °C) and the reaction mixture was stirred for 21 h. The reaction mixture was centrifuged for 15 min. at 4400 rpm. After discarding the supernatant, the solid product was washed three times with EtOH:MeOH (90 mL, 4:1). The composition of $TiO_2$-SWNT-$SiO_2$-21) was determined by XPS (Table 3.1).

**$TiO_2$(P25) mixed with silica via reflux.** In a typical reaction, $TiO_2$(P25) (100 mg, 1.25 mmol) is placed in a round bottom flask with the appropriate amount of fumed silica [2.5 mg, 0.042 mmol, 2.5 wt.% of $TiO_2$(P25)]. Toluene (40 mL) was added and the powders were bath sonicated for 1 minute, followed by reflux with stirring for 24 hours. After cooling the sample was vacuum filtered and the $TiO_2$(P25)-$SiO_2$ powder collected and dispersed in acetone by bath sonication for 20 minutes. The mixture is vacuum filtered again and washed with copious amounts of acetone. For the purposes of NMR studies a 5 wt.% of fumed silica (20 mg) was added to the $TiO_2$(P25), (400 mg, 5.0 mmol) and refluxed for 24 hours, following work-up, the relaxation agent $Fe(acac)_3$ (4.5 mg, 0.013 mmol) is mixed with acetone (35 mL) and added. The mixture is stirred and then allowed to dry by evaporation. For the purposes of UV-vis spectroscopy two samples of $TiO_2$(P25)-$SiO_2$ are prepared with higher weight percents of silica (10 wt.% and 20 wt.% of $TiO_2$(P25)).

**P25 mixed with silica via stirring.** $TiO_2$(P25) (100 mg, 1.25 mmol) is mixed in a round bottom flask with fumed silica (2.5 mg, 0.042 mmol, 2.5 wt.% of $TiO_2$(P25)). Toluene (40 mL) was added and the powders are bath sonicated for 1 minute, followed by stirring for 24 hours at room temperature, after which the mixture is vacuum filtered. The $TiO_2$(P25)-$SiO_2$ powder is collected and dispersed in acetone by bath sonication for 20 minutes. The mixture is vacuum filtered again and washed with copious amounts of acetone.

**Congo red studies.** Studies performed on $TiO_2$-SWNT-PP, $TiO_2$-SWNT-$SiO_2$ and $TiO_2$-SWNT-glass for Congo red adsorption and degradation, along with XRD testing was done by our research collaborator in the Li lab at Rice University. Experimental for Congo red adsorption and degradation is described elsewhere.[49]

**MS2 bacteriophage studies.** Experiments performed on $TiO_2$(P25), $TiO_2$(P25)-$SiO_2$ to study bacteriophage inactivations was done by our research collaborator in Li lab at Rice University. Experimental for bacteriophage inactivation is described elsewhere.[50]

## References


1. A. Fujishima, T. N. Rao, and D. A. Tryk, *J. Photochem. Photobiol. C*, 2000, **1**, 1.
2. Y. Ao, J. Xu, D. Fu, and C. Yuan, *Electrochem. Commun.*, 2008, **10**, 1812.
3. X. Chen and S. S. Mao, *Chem. Rev.*, 2007, **107**, 2891.
4. H. Choi, A. C. Sofranko, and D. D. Dionysiou, *Adv. Funct. Mater.*, 2006, **16**, 1067.
5. Y. Yao, G. Li, S. Ciston, R. M. Lueptow, and K. A. Gray, *Environ. Sci. Technol.*, 2008, **42**, 4952.

6. J. M. Planeix, N. Coustel, B. Coq, V. Brotons, P. S. Kumbhar, R. Dutartre, P. Geneste, P. Bernier, and P. M. Ajayan, *J. Am. Chem. Soc.*, 1994, **116**, 7935.

7. W. Li, C. Liang, W. Zhou, J. Qiu, Z. Zhou, G. Sun, and Q. Xin, *J. Phys. Chem. B.*, 2003, **107**, 6292.

8. J. Sun, M. Iwasa, L. Gao, and Q. Zhang, *Carbon*, 2004, **42**, 895.

9. M. Pender, L. Sowards, J. D. Hartgerink, M. O. Stone, and R. R. Naik, *Nano Lett.*, 2006, **6**, 40.

10. E. Llobet, E. H. Espinosa, E. Sotter, R. Ionescu, X. Vilanova, J. Torres, A. Felten, J. J. Pireaux, X. Ke, G. V. Tendeloo, F. Renaux, Y. Paint, M. Hecq, and C. Bittencourt, *Nanotechnology*, 2008, **19**, 375501.

11. Y. -J. Liu, Z. –M. Wang, M. Aizawa, W. -Q. Peng, and T. Hirotsu, *Mater. Lett.,* 2009, **63**, 260.

12. K. Woan, G. Pyrgiotakis, and W. Sigmund, *Adv. Mater.*, 2009, **21**, 2233.

13. B. Liu and H. C. Zeng, *Chem. Mater.*, 2008, **20**, 2711.

14. E. A. Whitsitt and A. R. Barron, *Chem. Commun.*, 2003, 1042.

15. E. A. Whitsitt, V. C. Moore, R. E. Smalley, and A. R. Barron, *J. Mater. Chem.*, 2005, **15**, 4678.

16. R. Colorado, Jr. and A. R. Barron, *Chem. Mater.*, 2004, **16**, 2691.

17. H. R. Jafry, E. A. Whitsitt, and A. R. Barron, *J. Mater. Sci.*, 2007, **42**, 7381.

18. R. Loscutova and A. R. Barron, *J. Mater. Chem.*, 2005, **15**, 4346.

19. R. E. Anderson and A. R. Barron, *Main Group Chem.*, 2005, **4**, 279.

20. Water, sanitation, and hygiene links to health; http://www.who.int/water_sanitation_health/publications/facts2004/en/index.html

21. M. V. Yates, J. Malley, P. Rochelle, and R. Hoffman, *Journal American Water Works Association.* 2006, **98**, 93.

# Chapter 4

# Coating Carbon Nanotubes with Lead Sulfide and Bismuth Sulfide

## Introduction

X-rays were discovered in 1895 and since then, its advantages, disadvantages and sources have been studied in great depth.[1] Manmade X-rays are extensively used in the medical and health care industry for therapeutics and diagnostics. In the healthcare industry, 67% of the population in developed countries uses x-rays in some form of diagnostic and therapeutic care. In the underdeveloped and developing countries, 5 - 13% of the population uses X-rays for medical reasons. It is estimated by United Nations that developing and underdeveloped countries will see a surge in the use of X-rays for diagnostics/therapeutics as quality of healthcare is made available to these nations. While X-rays can be beneficial for diagnostics and therapeutics such as X-ray guided minimally invasive surgeries, prolonged and high doses of X-ray radiation are known for its damaging effects to humans and equipment. According to reports by the United Nations, prolonged exposure can lead to detrimental effects for humans such as permanent burns, damage to the DNA and tissue cells, mutation of genes and eventually cancer.[2] Given the severity of the damage from X-rays, standards have been put in place by the government on protection practices for personnel and facilities using X-rays. In order to ensure minimal X-ray radiation penetration, individuals who come in contact with X-rays are required to wear lead-lined protection wear such as aprons, gloves, goggles, and thyroid protection. Three different categories of wearable protection include: total (100%) lead-lined clothing, lead composite clothing, and non-lead clothing. While the total lead lined clothing has the highest protection against high and scattered low energy radiation, it is inflexible, extremely heavy (15.1 lbs/sq yard) and can cause severe back problems for individuals who wear them for many hours. The lead composite clothing (9.1 lbs/sq yard)

and non-lead clothing (similar to lead composite) weighs less than the 100% lead-lined clothing, but does not provide the optimal protection against high and scattered radiation, thus allowing more radiation to penetrate the individual. Therefore, customers have a tough choice of choosing between clothing which is inflexible, heavy and can cause severe back problems, yet provides higher radiation protection, or a light weight clothing with less protection from radiation, potentially resulting in cancer. Given the problem at hand, we wanted to see if nanomaterials could be developed which could both absorb X-rays and weigh less than the traditional 100% lead lined gowns. These X-ray absorbing nanomaterials could then be incorporated within different radiation protection wearable products, providing protection and comfort. Therefore, in this study we focus on making nanoparticles and coatings of lead and bismuth compounds, as both lead and bismuth are known to absorb X-rays.

One of the attractions of carbon nanotubes (CNTs) is its use as vessels which can contain materials at the nanoscale. It has been suggested that properties of CNTs can be modified by introducing foreign materials such as metals or metal salts into them.[3] Two general methods have been followed by scientists to introduce metal salts and metals inside CNTs, namely capillary fillings using molten media, and wet chemistry techniques.[4] Capillary fillings are made by mixing metal or metal salts with CNTs, and transferring it into a vacuum sealed tube for heating until the metal is molten; once molten, it is drawn into the CNT via capillary action.[4,5] Another methodology is to open the caps of the tubes first, and then use capillary action to add molten metal inside the CNTs. This is achieved by heating the tubes under oxygen and lead metal, or carbon dioxide which will oxidize the caps of the tubes, opening them for the filling of metals and metal salts.[3,6] This technique produces a higher percentage of tubes with open caps; however, it does not necessarily result in a high yield of tubes being filled. Wet chemistry techniques have also been used where the CNTs are treated with an acid and a metal salt

for the opening and filling of the tubes. The opening and filling of tubes can be done *in situ* using a one step process,[7] or using a two step process. In a one step process, the tubes are etched with acid and simultaneously filled with metal salts dissolved in aqueous solutions; in a two step process, the tubes are first etched and washed, followed by treating with aqueous solutions of metal salts.[8] In the first part of this chapter, we explore the different techniques used to fill vapor grown carbon fibers (VGCFs) and multi walled carbon nanotubes (MWNTs) with Pb salts, and try to understand if the CNTs filled with lead salts and its compounds are able to absorb X-rays.

Lead sulfide (PbS) is an important IV-VI group semiconductor, and has attracted considerable attention given its small direct band gap (0.41 eV) and a large excitation Bohr radius of 18 nm, which gives it a strong quantum confinement of electrons and holes. The making of various forms of PbS nanoparticles, such as nano spheres, nanorods and nanowires have been of great interest given their potential applications in the fields of light-emitting diodes, fast switching IR detectors, solar absorbers, and photography.[9,10] Similarly, bismuth sulfide ($Bi_2S_3$) is a chalcogenide V-VI group semiconductor, and nanomaterials of $Bi_2S_3$ have also been of great interest because of its large photoconductivity, absorption coefficients, direct band gap (1.2 - 1.7 eV), and high thermoelectric power. Potential applications of $Bi_2S_3$ lie in the fields of photodetectors, liquid-junction solar cells, thermoelectric coolers, hydrogen sensors, and X-ray computed tomography (CT) imaging agents.[11,12]

Various methodologies have been employed for making different sizes and types of nanoparticles and film coatings of metal sulfide, in particular PbS and $Bi_2S_3$. Some of these techniques include using surfactants which act as structure directing and capping agents, polymer compounds for templates, substrates which contain hydroxyl groups for the deposition of metal sulfide nanoparticles, and in some cases using no surfactant.[9,10,13,14,15,16] To the best of our knowledge, while there are many published

articles on making various sizes and forms of PbS and $Bi_2S_3$ nanoparticles and thin films, there is no research which shows PbS and $Bi_2S_3$ coatings on CNTs. Therefore, in the second half of this chapter, we explore different reaction conditions to test if coatings of PbS and $Bi_2S_3$ can be employed on CNTs. A general mechanism from literature[9,17] which is used to make copper sulfide (CuS) and PbS nanoparticles is as follows:

$$Pb(NH_3)_4^{2+} \rightarrow Pb^{2+} + 4\ NH_3 \quad (4.1)$$

$$NH_3 + H_2O \rightarrow NH_4^+ + OH^- \quad (4.2)$$

$$(NH_2)_2CS + 2\ OH^- \rightarrow S^{2-} + 2\ H_2O + H_2CN_2 \quad (4.3)$$

$$Pb^{2+} + S^{2-} \rightarrow PbS \quad (4.4)$$

In the reaction, the role of ammonium hydroxide is two fold. It forms a basic of lead acetate and thereby, controls the rate of reaction by limiting the availability of free $Pb^{2+}$ ions; it also creates an alkaline environment for the hydrolysis of thiourea. Previously, a similar reaction mechanism is followed by our lab in coating SWNTs with cadmium sulfide.[18] We use a similar preparation to coat CNTs with PbS and $Bi_2S_3$.

## Results and Discussion

**Filling of CNTs with lead.** As mentioned in the Introduction, previous tries have been made to add lead inside CNTs. Two different methods, *in situ* and a two step method have been tried on VGCFs and MWNTs.

Both VGCFs and MWNTs have been used for an *in situ* addition of lead inside the tubes. Figure 4.1 shows the TEM images of both plain and treated VGCFs. While it seems that the tips of the VGCFs have been opened or etched, there seems to be very little addition of lead inside the VGCFs. Figure 4.1c shows either etched off carboneous material or lead salts on the openings of the VGCFs. Figure 4.1d shows some

particles/spheres around the VGCFs, but not inside it. A simple X-ray test as seen in Figure 4.2a reveals that there is significant absorption of the X-rays by the treated VGCFs, while the untreated plain VGCFs have no absorption (Figure 4.2c). The X-ray absorption result did not seem to be consistent with the TEM image which showed no addition of lead inside the tubes. SEM was performed on these samples (Figure 4.3), and the image reveals that there are spheres present on the outside of the VGCFs, which may have accumulated during the reflux/calcination process of lead salts with VGCFs.

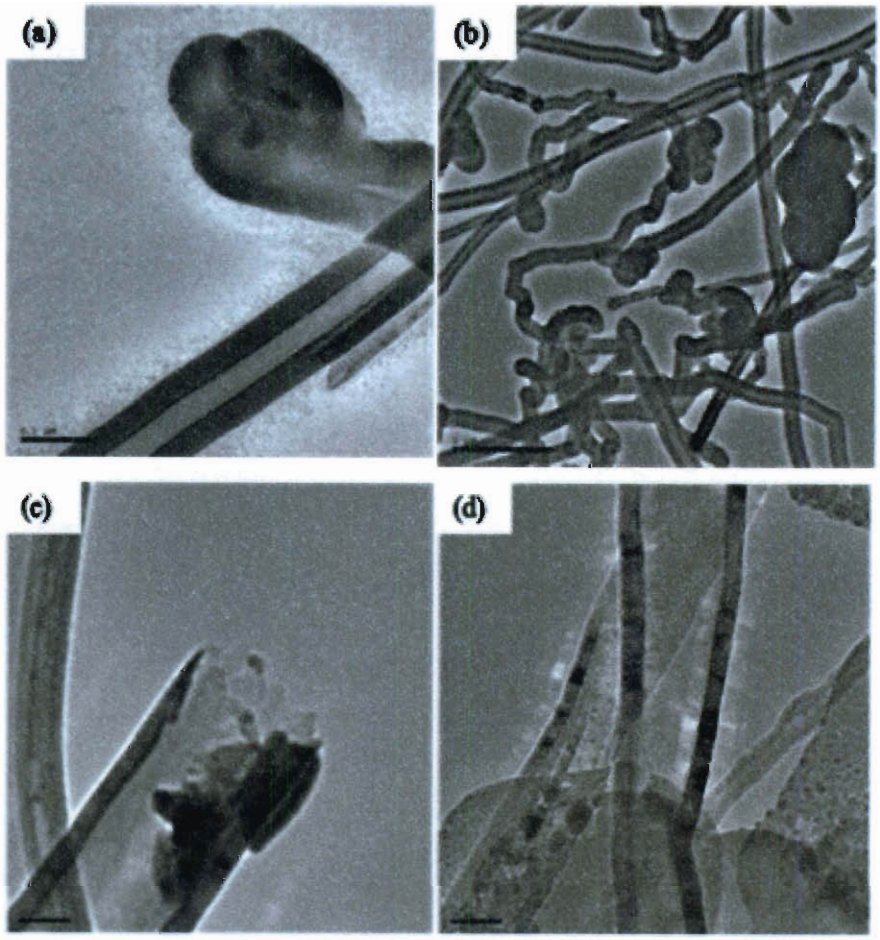


**Figure 4.1.** TEM images of plain VGCFs (a) and (b), and VGCFs treated with *in situ* method for the addition of Pb salts (c) and (d).

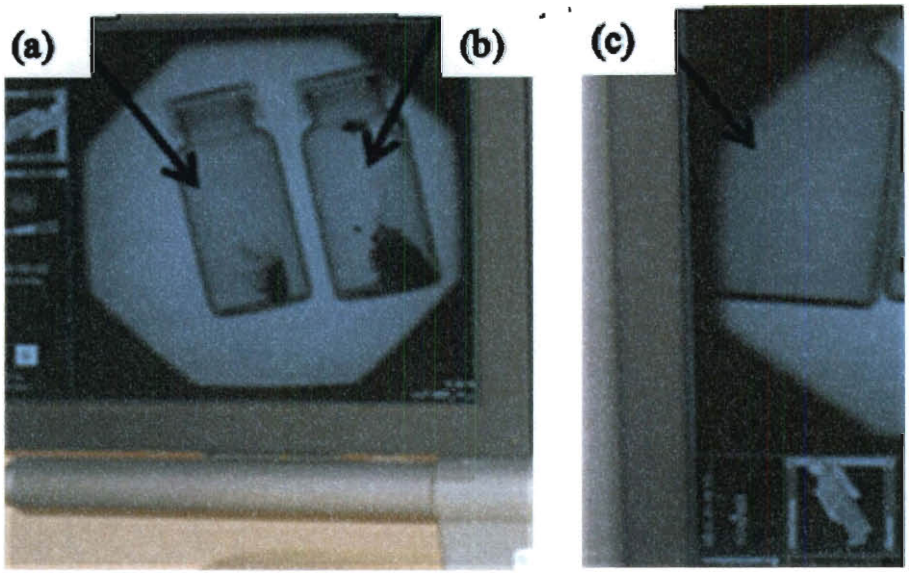


**Figure 4.2.** X-ray absorption by (a) VGCF treated with *in situ* method of adding Pb salts (b) lead nitrate salts and (c) plain VGCFs.

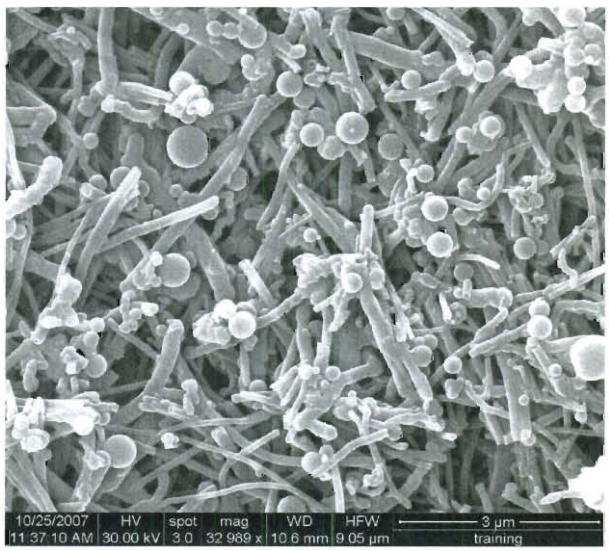


**Figure 4.3.** SEM image showing spheres present on the outside of the VGCFs treated with *in situ* method for the addition of Pb salts.

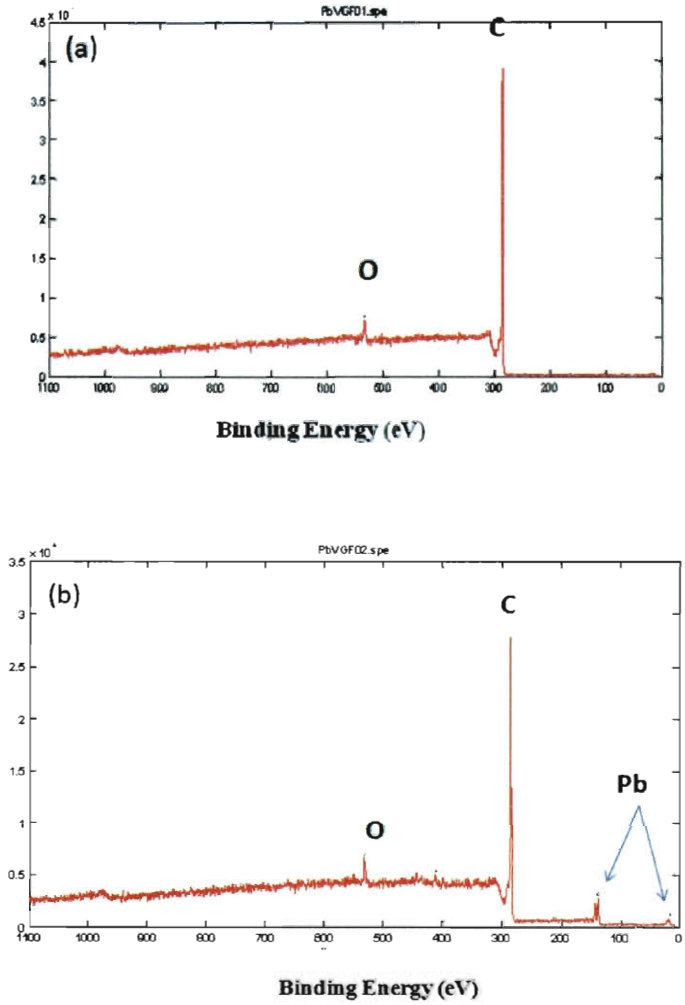


**Figure 4.4.** XPS showing (a) plain VGCFs and (b) VGCFs treated with *in situ* method of adding Pb salts.

XPS results (Figure 4.4b) confirm the presence of lead on the surface of the VGCFs. The absorption of X-rays takes place by the presence of lead and lead salts present on the outside of the VGCFs and there is none that is present on the inside of the VGCF. In a similar fashion, MWNTs are also used to fill with lead, as shown in Figure 4.5. Again, the presence of small spheres are visible on the outside, with no visible amounts of lead present on the inside. The X-ray absorption pictures shown in Figure 4.6

reveal some absorption by the treated MWNTs, though only because of the presence of the lead salt present on the outside of the tubes.

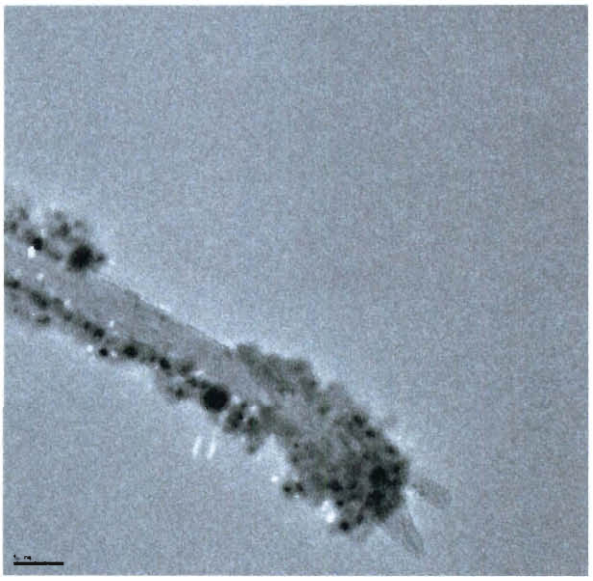

**Figure 4.5.** TEM image showing the presence of Pb salts on the outside walls of the MWNT.

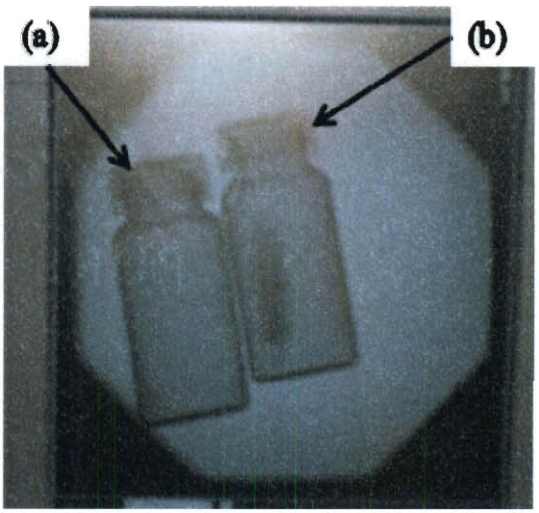


**Figure 4.6.** X-ray absorption by (a) plain MWNTs and (b) MWNTs treated with *in situ* method for the addition of Pb salts.

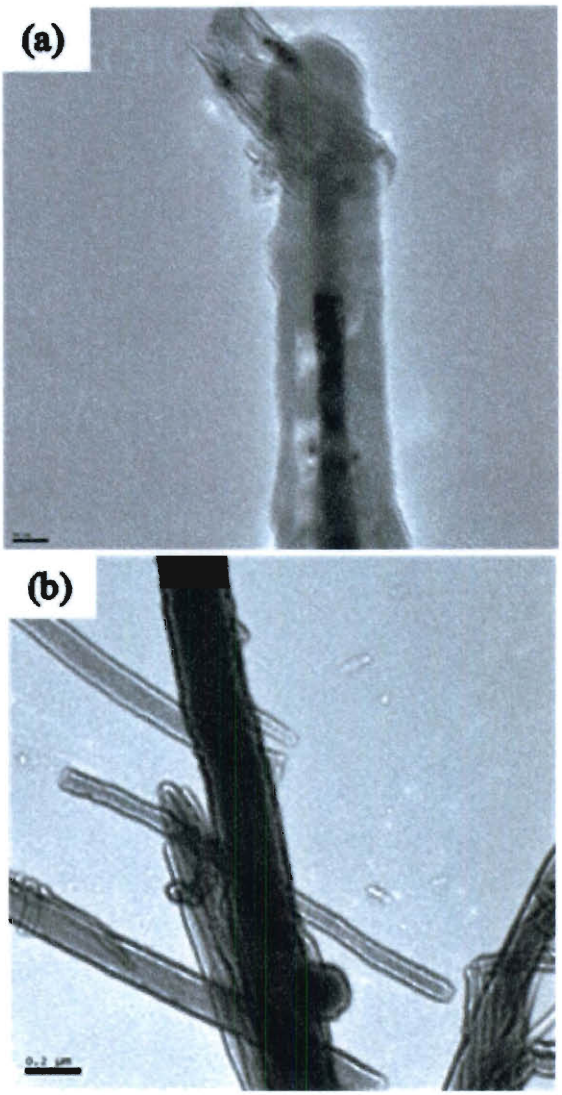


**Figure 4.7.** TEM images showing the presence of Pb salts inside the VGCFs via the two step method.

For the two step process, the VGCFs showed some promising results when it came to the filling of the tubes. As shown in Figure 4.7, the presence of lead can be seen inside the VGCFs. Unfortunately, even with the lead compound fillings, there was no X-ray absorption of tubes. The MWNTs prepared using the two step method show (Figure 4.8) mostly etching of the sidewalls and the presence of some specs of lead. While the filling of the MWNTs is quite unlike the fillings obtained with the VGCFs, neither the

treated VGCFs nor the MWNTs absorbed any X-rays. Given the above results, it seemed that x-rays can be absorbed if there is presence of lead on the surface of the tubes. We use a variety of LPD methods to grow lead compounds on the surface of the CNTs.

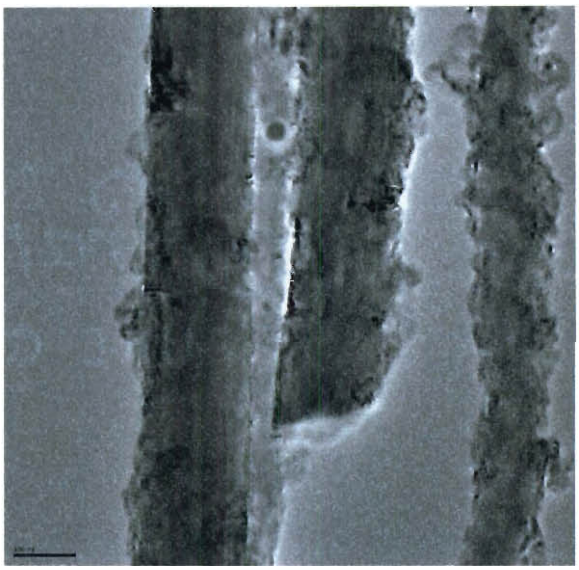

**Figure 4.8.** TEM image of MWNT treated using two step method, showing the etching of the sidewalls and miniscule (if any) presence of Pb salts.

**Coating CNTs using surfactants.** Sodium dodecyl sulfacte (SDS) is used to coat MWNTs with PbS compounds. A similar method for CdS LPD on single walled carbon nanotubes (SWNTs) with the aid of surfactants has been previously reported by our lab.[18] As it can be seen in Figure 4.9, the coatings are quite uneven and seems as if there is a "fused flower petal" like growth of PbS compounds in between the MWNTs. The EDX elemental analysis in Figure 4.10 confirms the presence of lead and sulfur. Previously, the presence of surfactants in LPD growth solutions have shown colloidal growth along the nanotube surface as deposition takes place around the micelles.[19] A similar reaction to make PbS nanocrystallites has been reported by Dong and co-workers.[9] According to

their report, the concentration of the surfactant played a huge role in determining the types of nanostructures of PbS formed.

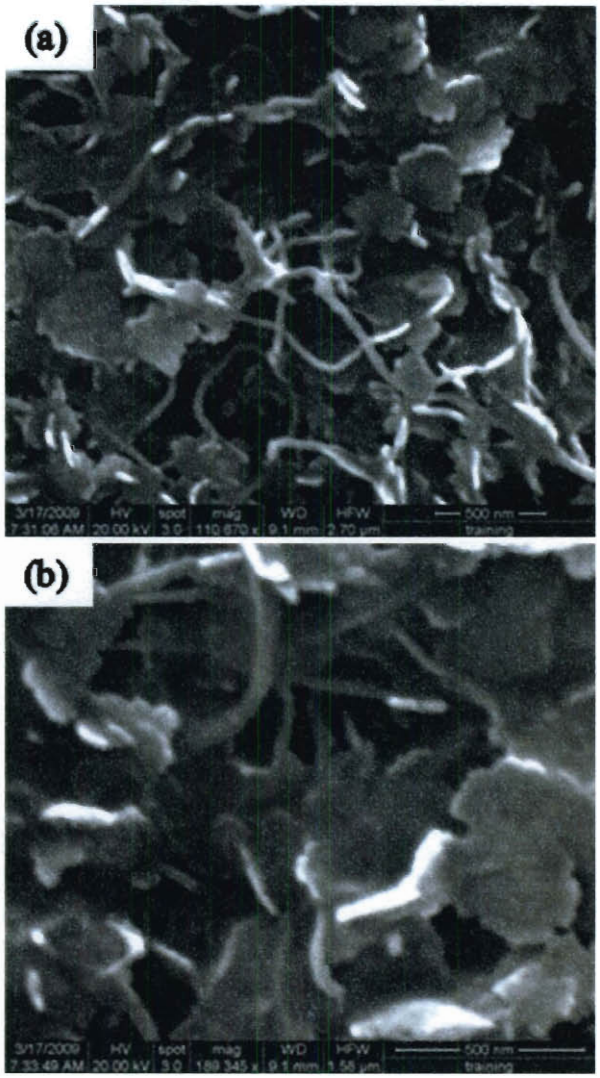


**Figure 4.9.** SEM image showing PbS coatings of MWNTs obtained using SDS. A "petal like" fused structure in between the MWNTs.

The surfactant acts as a capping and structure directing agent by adsorbing to certain facets of the crystal structure, controlling the direction of the crystal growth. When they increased their surfactant concentrations, they got "downy-velvet flower" like

structures, which are quite similar to those observed in Figure 4.9. Given the huge "fused flower petals" within the tubes, it seems that in our case, the deposition is more of a composite nature than coating of individual MWNTs. It is possible that changing the concentration of the surfactant would yield different growths on the CNTs.

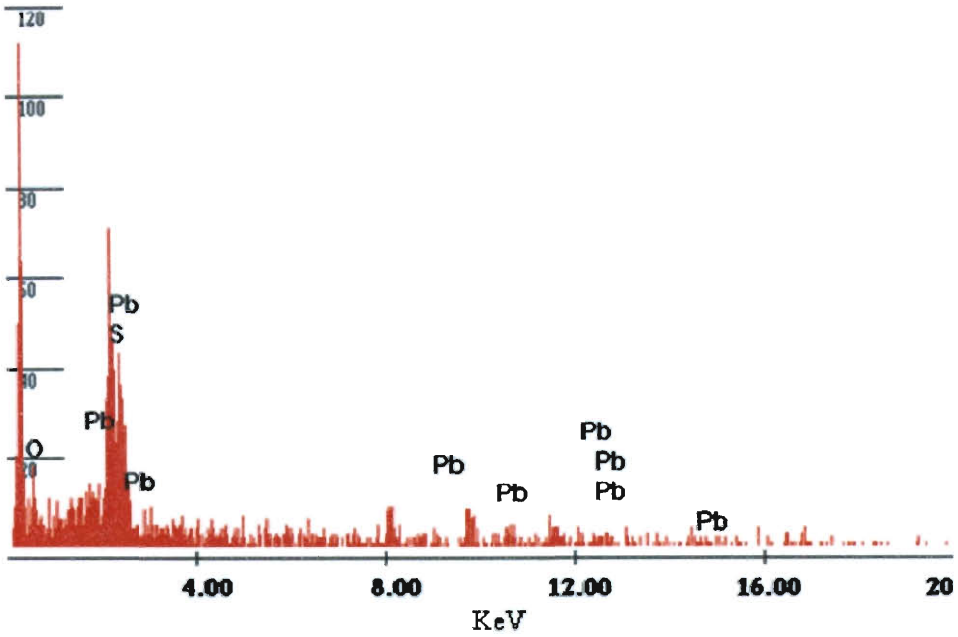


**Figure 4.10.** EDX showing the presence of Pb and S on MWNTs coated using SDS.

Cetyl trimethylammonium bromide (CTAB) is also used to coat SWNTs with PbS. As can be seen in figure 4.11, the SWNTs seem to be bundled and there are huge "boulders" of Pb compounds present within the SWNTs-PbS matrix. Previously in our lab, it has been shown that in order to coat CNTs in an acidic medium, it is best to use dodecyl trimethylammonium bromide (DTAB) or CTAB as surfactants, while SDS and dodecylbenzenesulfonic acid (SDBS) work best in basic mediums.[20,21] Using SDS or SDBS to coat SWNTs in acidic mediums have led to the coating of SWNT bundles,

rather than individual tubes. However, it has been previously reported in literature of the formation of PbS crystallites under similar reaction conditions in the presence of CTAB.[9]

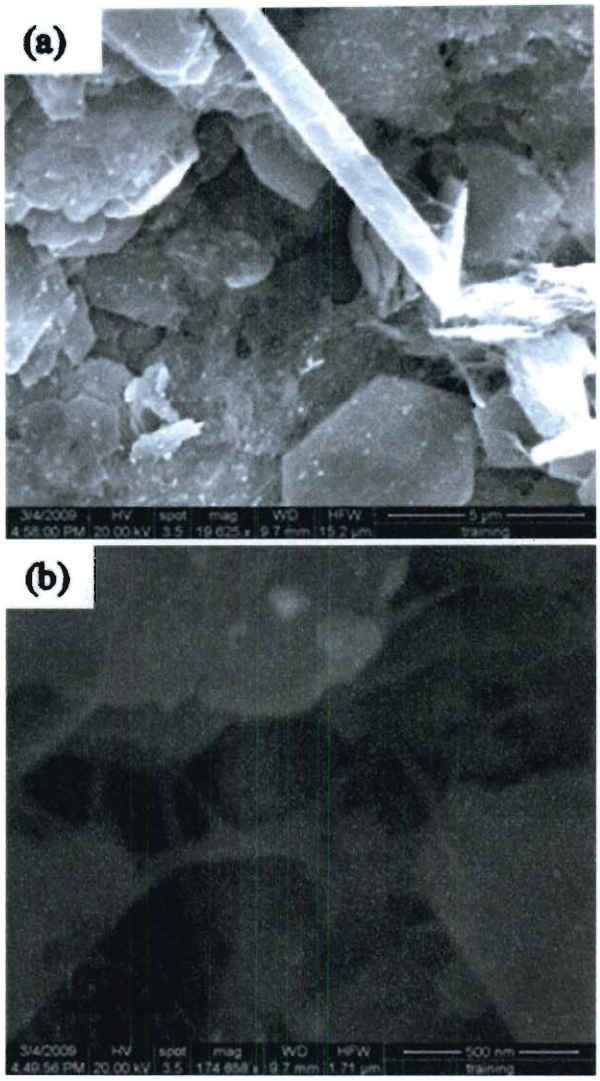


**Figure 4.11.** SEM image of SWNTs coated with PbS compounds with the aid of CTAB.

We believe that these boulders could be produced as a consequence of either a higher concentration of reactants and/or the presence of CTAB in a basic medium. An X-ray absorption study shows good absorption on this material (Figure 4.12); however, it is

due to the presence of boulders of Pb or Pb compounds, and not the coatings, if any, on the SWNTs.

**Coating acid treated VGCFs with PbS.** Given our previous experience in pre-treating CNTs (as explained in previous chapters), we wanted to find out if we could use acid treated tubes to get an even coatings of PbS on tubes, as opposed to the ones we were getting using surfactants. To the best of our knowledge, this is the first time CNTs are coated with PbS. As shown by Figure 4.13 and 4.14, the outer coatings of the VGCFs are colloidal yet even, and XPS results (Figure 4.15) reveal the presence of PbS and other Pb compounds. The amount of colloids present on the surface of the VGCF is dependent on the concentrations of reactants present. The higher the concentration of reactants, the more colloidal the growth; however, looking at the SEM image of the coated VGCFs from the lower reactant concentration, there is a presence of very minute and small colloids (Figure 4.13c). This is because the acid treated VGCFs have a presence of hydroxyl and carboxyl groups (Chapter 1, Table 1.3).

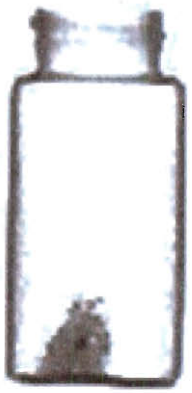

**Figure 4.12.** X-ray absorption by SWNTs in 2-step method using CTAB for coating with PbS.

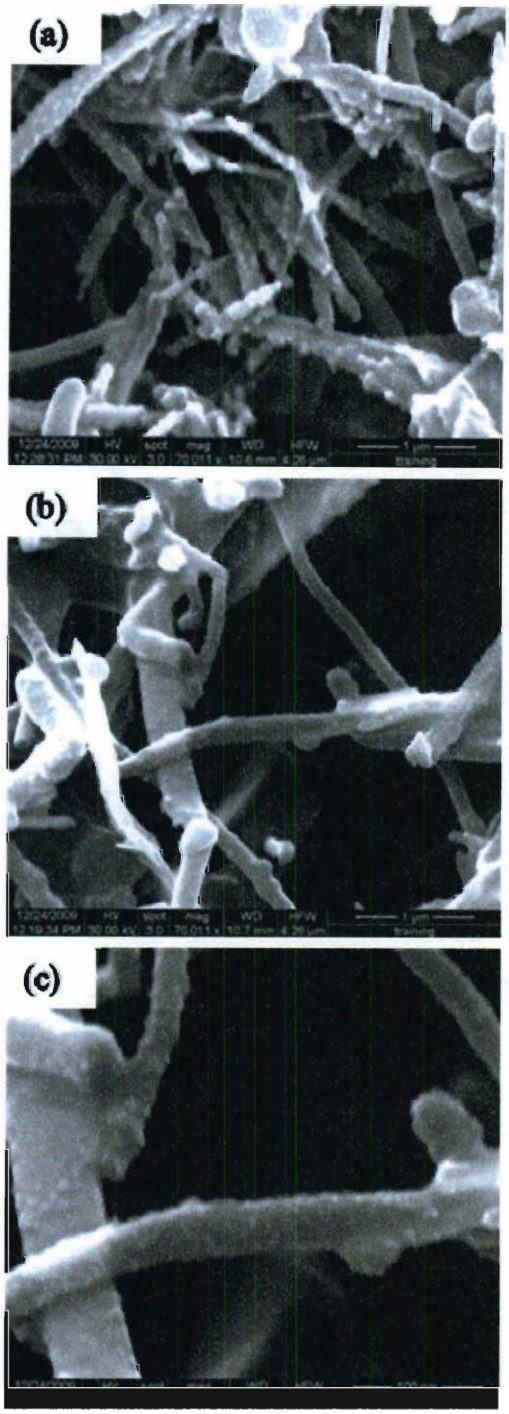


**Figure 4.13.** SEM image of acid treated VGCFs coated with PbS compounds: 2 hour reaction with high concentration of reactants (a), and 2 hour reaction with low concentration of reactants (b) and (c).

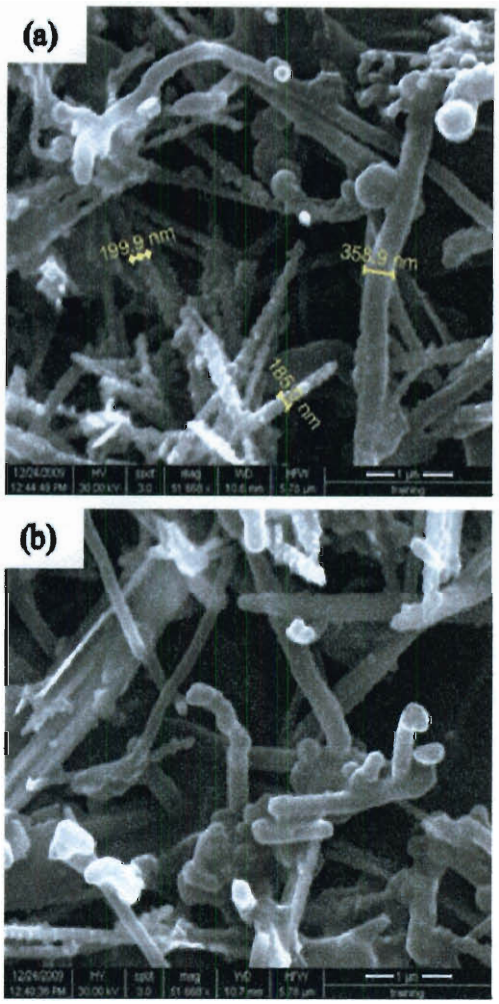


**Figure 4.14.** SEM image of acid treated VGCFs coated with PbS compounds: (a) 4 hour reaction with high concentration of reactants and (b) 4 hour reaction with low concentration of reactants.

Previously in literature, it has been described that for thin film coatings of CdS on substrates, the presence of OH groups on substrates or solution made a significant different in the type of coatings achieved.[16] It has been reported that substrates with the presence of $Cd(OH)_2$ groups allowed for the nucleation and growth of CdS; the formation of CdS occurred by the adsorption of thiourea on $Cd(OH)_2$ followed by the decomposition of $Cd(OH)_2$-thiourea complex. However, substrates which had no

presence of OH groups showed films of poor surface coverage that were less adherent to the substrate. The coatings on acid treated VGCFs are quite a contrast to the coating obtained by surfactants. It is possible that there is good adhesion of PbS and other Pb compounds (Figure 4.15) due to the initial presence of OH groups. X-ray absorption tests on these materials are work in progress.

**Coating of VGCFs with $Bi_2S_3$ using SDS surfactant.** SDS is used as a surfactant to disperse VGCFs in order to coat them with $Bi_2S_3$ compounds. As can be seen by Figure 4.16, while there is growth on the surface on the VGCFs, there is also a small presence of colloids. The surfactant micelles present in solution and around the VGCFs act as templates around which deposition takes place forming colloids. This is also observed in Chapter 1 (Figure 1.3). XPS results confirm the presence of $Bi^{3+}$ and $S^{2-}$ as shown in Figure 4.17. There is however, an overlap of Bi4f and S2p peaks.

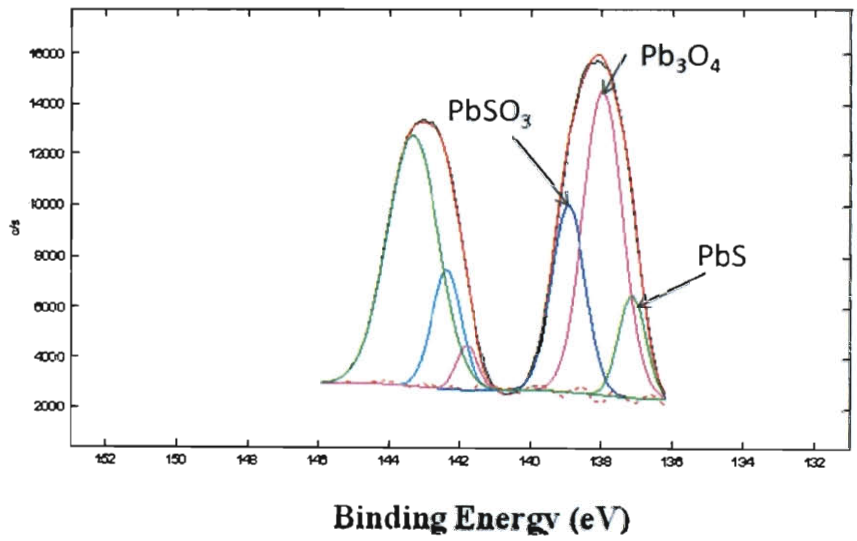


**Figure 4.15.** XPS of acid treated VGCFs coated with Pb compounds for a sample with 2 hour reaction time with low concentration of reactants.

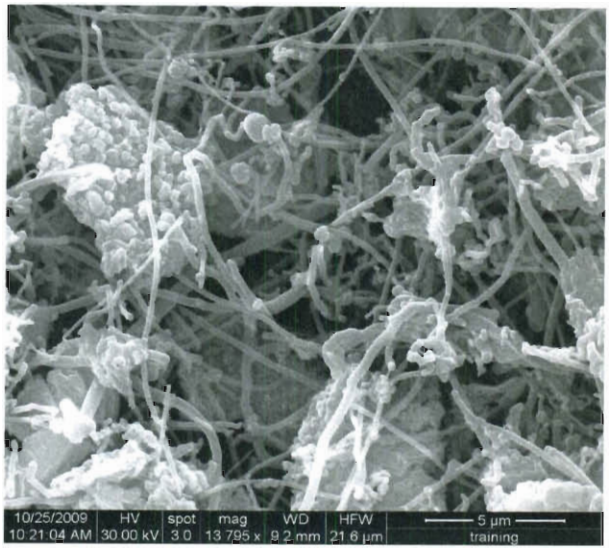


**Figure 4.16.** SEM image showing the coatings of VGCFs with $Bi_2S_3$ in the presence of SDS.

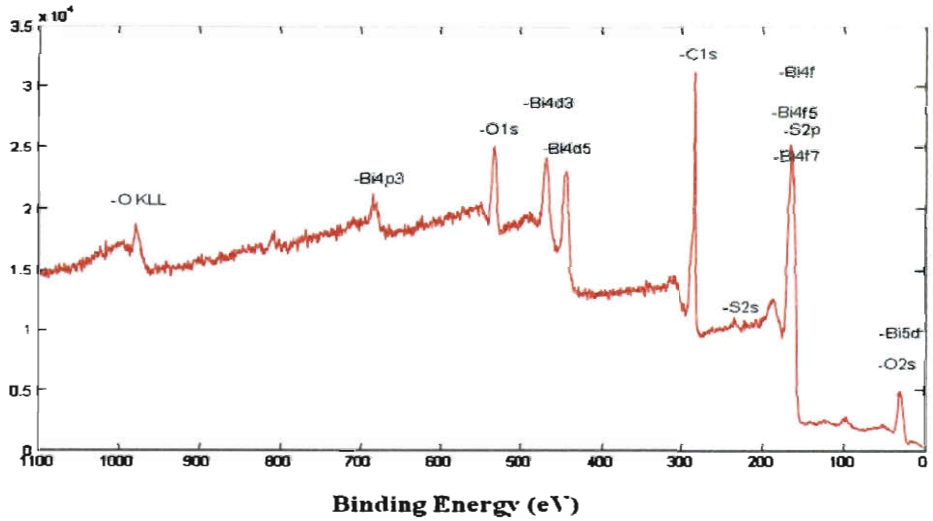


**Figure 4.17.** XPS of VGCFs coated with $Bi_2S_3$ using SDS, Bi4f and S2p peaks.

**Coating of acid treated VGCF with $Bi_2S_3$.** In addition to coating VGCFs with $Bi_2S_3$ using surfactants, we also wanted to try coatings of $Bi_2S_3$ on acid treated VGCFs in order to investigate if there are any differences in the coatings between the surfacted

versus acid treated tubes. Figure 4.18 shows the coatings of acid treated VGCFs with $Bi_2S_3$ compounds, confirmed by the XPS (Figure 4.19). The VGCFs coated in the presence of SDS seem to have an uneven growth, while the acid treated VGCFs have a more even growth of $Bi_2S_3$. Work in progress includes testing for X-ray absorption of the coated fibers.

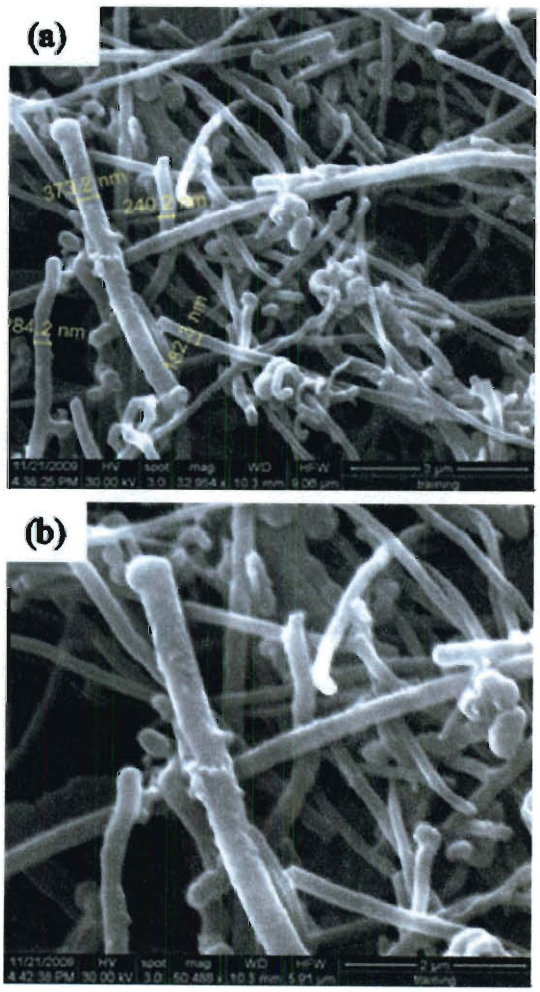


**Figure 4.18.** SEM image of acid treated VGCFs coated with $Bi_2S_3$.

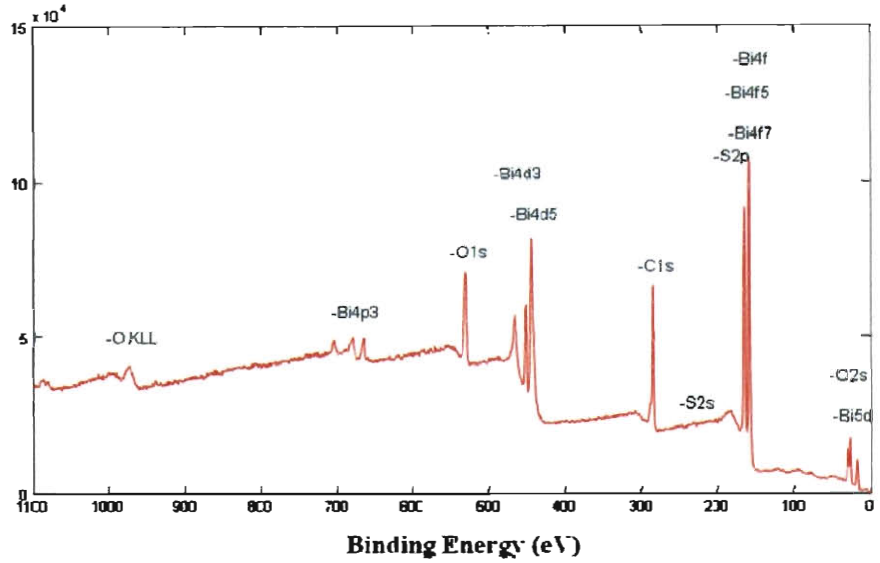


**Figure 4.19.** XPS of acid treated VGCF coated with $Bi_2S_3$ with overlapping Bi4f and S2p peaks.

## Conclusions

We have investigated the fillings of CNTs with $Pb^{2+}$ salts using two different methods. In the first *in situ* method, we found that there was no filling of CNTs with metal or metal salts, and the X-ray absorption we got was based on metal salts present on the outside of the CNTs. Using a two step process, we were successful in filling VGCFs with metal/metal salts, but not MWNTs; nonetheless, there was no X-ray absorption from tubes filled using a two step process. In the second half of this chapter, we investigated different methodologies of coating CNTs with PbS and $Bi_2S_3$ compounds using the aid of surfactants and acid treated tubes. It turns out that the acid treated tubes give a more even growth of the metal sulfide nanoparticles compared to the surfacted tubes. Also, the "type of colloidal" coating present on the acid treated VGCFs is dependent on the concentration of reactants. The ability for the acid treated and coated VGCFs to absorb x-rays is currently under investigation.

## Experimental

VGCFs, nitric acid, ethanol, methanol, and Cole Palmer PTFE filters are the same as described in Chapter One. SWNTs are the same as used in Chapter Three. MWNTs (Cheap Tubes, >95wt.%, 8 - 15 nm outer diameter), lead acetate ( $Pb(NO_3)_2$, Sigma-Aldrich), lead acetate ($Pb(CH_3CO_2)_4$, Sigma-Aldrich), thiourea (Sigma-Aldrich), ammonium hydroxide (29 wt.%, Fisher), sodium dodecyl sulfate (SDS, Sigma-Aldrich), cetyl trimethylammonium bromide (DTAB, Sigma-Aldrich), cetyl trimethylammonium bromide (CTAB) (Sigma-Aldrich), and chloroform (Sigma-Aldrich) is used as received without any further purification.

**Pb fillings of VGCFs and MWNTs (*in situ*/one step).** VGCF or MWNTs (100 mg) is added to a round bottom flask containing concentrated nitric acid (69 - 71 wt.%, 11 mL) and lead nitrate (500 mg). The mixture is set to reflux while stirring in an oil bath at 140 °C for 4.5 hours. After the allotted reaction time, the nitric acid is evaporated, followed by the drying of the fibers in a furnace at 100 °C overnight. The fibers are calcined in a furnace under the following conditions: VGCFs or MWNTs are heated under argon at 10 °C $min^{-1}$ to 100 °C for 1 hour, following by ramping the temperature to 580 °C at 10 °C $min^{-1}$ for 5 hours. The samples are then cooled down to 470 °C at 10 °C $min^{-1}$ and the gas is switched to hydrogen. The samples are kept under hydrogen for 2 - 14 hours.

**Pb fillings of VGCFs and MWNTs (two-step).** VGCF or MWNTs (100 mg) is added to a round bottom flask containing concentrated nitric acid (69 - 71 wt.%, 22 mL). The mixture is set to reflux while stirring for allotted amounts of time (4.5 hours, 12 hours). After reflux, the fibers are filtered and washed off with copious amounts of

acetone and DI $H_2O$, followed by chloroform. The tubes are then dried off overnight at 100 °C in a furnace.

Acid treated VGCFs (25 mg) or MWNTs (15 mg) is added to a solution of lead nitrate in DI $H_2O$ (53.8 M, 100 - 125 mg in 5 - 7mL DI $H_2O$), and refluxed while stirring for an allotted time (4 hours, 12 hours). After reflux, the mixture is allowed to cool to room temperature, followed by centrifuging for 5 minutes at 4400 rpm. The supernatant is discarded and the VGCFs are dried in a furnace at 100 °C overnight. A similar calcination procedure is followed for the *in situ* process described above.

**Coating MWNTs with PbS using SDS surfactant.** MWNTs (30 mg) is probe sonicated in a SDS solution (1 wt.%, 150 mL) for 10 minutes, followed by centrifugation for 10 minutes at 4400 rpm; the supernatant is saved and the process of centrifugation is repeated 3 times. The supernatant is separated for further experiments. MWNT-SDS solution (3 mL) is mixed with ammonium hydroxide (1.15 M, 0.6 mL), thiourea (0.080 M, 0.6 mL), and lead acetate (0.080 mL, 0.6 mL). The mixture is set to stir for 4 hours at room temperature. After the allotted reaction time, the mixture is added to EtOH (35 mL) centrifuged for 10 minutes at 4400 rpm. The decant is discarded and centrifugation/discarding process is repeated 5 more times using EtOH.

**Coating SWNTs with PbS using CTAB surfactant.** SWNTs (10 mg) is probe sonicated in a CTAB solution (1 wt.%, 80 mL) for 10 minutes, followed by centrifugation for 10 minutes at 4400 rpm; the supernatant is saved and the process of centrifugation is repeated 3 times. The supernatant is separated for further experiments. SWNT-CTAB solution (80 mL) is added to a plastic bottle and is set on stirring. To this, $CS_2$ (0.06 mL) is added and stirred for 5 minutes, followed by the addition of ammonium hydroxide (0.89 mL) and lead acetate (0.1 M, 9.6 mL). The bottle is lightly capped and

stirred in an oil bath at 40 C for 24 hours. Afterwards, 20 mL aliquots of the mixture are added to EtOH:MeOH (4:1, 25 mL), and centrifuged for 10 minutes at 4400 rpm. The decant is trashed and the coated SWNTs are washed with DI $H_2O$ (30 mL) 2 - 3 times using centrifugation/discarding of the decant. The SWNTs are dried at 100 °C in a furnace overnight, followed by calicination under hydrogen for 2 hours at 455 °C.

**Coating acid treated VGCF with PbS.** VGCFs (150 mg) is added to concentrated nitric acid (69 - 71 wt.%, 50 mL) and is stirred in a pyrex beaker in open air at 40 °C for 5 days, until the nitric acid is evaporated. The acid treated VGCFs are filtered and washed with copious amounts of acetone and DI $H_2O$, followed by chloroform. A stock solution of acid treated VGCF-$H_2O$ is prepared by adding VGCF (30 mg) to DI $H_2O$ (35 mL). An aliquot from this stock solution of acid treated VGCF-$H_2O$ (3mL) is mixed with DI $H_2O$ (4.8 mL), ammonium hydroxide (1.15 M, 0.6 mL), thiourea (0.080 M, 0.6 mL), and lead acetate (0.080 mL, 0.6 mL). The mixture is set to stir for 2 hours at room temperature. After the allotted reaction time, the mixture is added to EtOH (35 mL) centrifuged for 10 minutes at 4400 rpm. The decant is discarded and centrifugation/discarding process is repeated 5 more times using EtOH.

**Coating VGCFs with $Bi_2S_3$ using SDS surfactant.** VGCFs (30 mg) is probe sonicated in a SDS solution (1 wt.%, 150 mL) for 10 minutes, followed by centrifugation for 10 minutes at 4400 rpm; the supernatant is saved and the process of centrifugation is repeated 3 times. The supernatant is separated for further experiments. VGCF-SDS solution (50 mL) is mixed with bismuth nitrate (0.00004 mol, 19.4 mg) and thiourea (0.00008 mol, 6 mg) and is stirred for 2 hours at 45 °C. After the allotted reaction time 20 mL aliquots of the mixture are added to EtOH (25 mL), and centrifuged for 10

minutes at 4400 rpm. The decant is discarded and the centrifugation/dispersion process is repeated 5 times.

**Coating acid treated VGCFs with $Bi_2S_3$.** VGCFs (150 mg) is added to concentrated nitric acid (69-71 wt.%, 50 mL) and is stirred in a pyrex beaker in open air at 40 °C for 5 days, until the nitric acid is evaporated. The acid treated VGCFs are filtered and washed with copious amounts of acetone and DI $H_2O$, followed by chloroform. Acid treated VGCFs (8 mg) is sonicated with DI $H_2O$ (50 mL). To this, bismuth nitrate (0.00004 mol, 19.4 mg) and thiourea (0.00008 mol, 6 mg) are added and sonicated for a minute, followed by stirring at 45 C for 4 hours. After the allotted reaction time 20 mL aliquots of the mixture are added to EtOH (25 mL), and centrifuged for 10 minutes at 4400 rpm. The decant is discarded and the centrifugation/dispersion process is repeated 5 times.

## References


1. W. C. Roentgen. *Nature*, 1896, **53**, 274.
2. *Sources and Effects of Ionizing Radiation*, United Nations Scientific Committee on the Effects of Atomic Radiation (UNSCEAR), 2000.
3. S. C. Tsang, P. J. F. Harris, and M. L. H. Green. *Nature*, 1993, **362**, 520.
4. Y. Huh, L. Shao, G. Tobias, and M. L. H. Green. *J. Nanosci Nanotechnol.*, 2006, **6**, 3360.
5. M. Hulman, H. Kuzmany, P. M. F. J. Costa, S. Friedrichs, and M. L. H. Green. *Appl. Phys. Lett.*, 2004, **85**, 2068.
6. P. M. Ajayan, T. W. Ebbesen, T. Ichihashi, S. Iijima, K. Tanigaki, and H. Hiura. *Nature*, 1993, **362**, 522.

7. S. C. Tsang, Y. K. Chen, P. J. F. Harris, and M. L. H. Green. *Nature*, 1994, **372**, 159.

8. J. Sloan, J. Cook, J. R. Heesom, M. L. H. Green, and J. L. Hutchison. *J. Cryst. Growth*, 1997, **173**, 81.

9. L. Dong, Y. Chu, Y. Liu, M. Li, F. Yang, and L. Li. *J. Colloid Interface Sci.*, 2006, **301**, 503.

10. D. Kumar, G. Agarwal, B. Tripathi, D. Vyas, and V. Kulshrestha. *J. Alloys Compd.*, 2009, **484**, 463.

11. J. H. Kim, H. Park, C. Hsu, and J. Xu. *J. Phys. Chem.*, 2010, **114**, 9634-9639.

12. O. Rabin, J. M. Perez, J. Grimm, G. Wojtkiewicz, and R. Weissleder. *Nat. Mater.*, 2006, **5**, 118.

13. M. Orphanou, E. Leontidis, T. Kyprianidou-Leodidou, W. Caseri, F. Krumeich, and K. C. Kyriacou. *J. Colloid Interface Sci.*, 2006, **302**, 170.

14. A. K. Dutta, T. Ho, L. Zhang, and P. Stroeve. *Chem. Mater.*, 2000, **12**, 1042.

15. G. Xing, Z. Feng, G. Chen, W. Yao, and X. Song. *Mater. Lett.*, 2003, **57**, 4555-4559.

16. S. Gorer, and G. Hodes. *J. Phys. Chem.*, 1994, **98**, 5338.

17. S. K. Haram, A. R. Mahadeshwar, and S. G. Dixit. *J. Phys. Chem.*, 1996, **100**, 5868.

18. R. Loscutova and A. R. Barron. *J. Mater. Chem.*, 2005, **15**, 4346.

19. E. A. Whitsitt, *Liquid Phase Deposition of Silica: Thin Films, Colloids, and Fullerenes*, Ph.D., Rice University, Houston, TX, 2005.

20. E. A. Whitsitt and A.R. Barron, *Nano Lett.*, 2003, **3**, 775.

21. R. Colorado, Jr. and A.R. Barron, *Main Group Chem.*, 2005, **4**, 279.

## Overall Conclusions

While all the chapters in this thesis demonstrate different coatings on carbon nanotubes (CNTs) or vapor grown carbon fibers (VGCFs), there are certain general conclusions that can be drawn for coating carbon nanotubes and fibers. For $SiO_2$, PbS, and $Bi_2S_3$ coatings on VGCFs and multi walled carbon nanotubes (MWNTs), the best heterogeneous or even coatings achieved were for the VGCFs pre-treated with nitric acid. The use of surfactants in coating VGCFs and MWNTs with the above mentioned materials simply led to either a homogenous growth or a composite growth, thereby, demonstrating that the individual fiber/tube coatings, or a heterogeneous growth could not be achieved with the aid of surfactants. This is a striking contrast to the heterogeneous coatings of $SiO_2$, CdSe, and CdS achieved on single walled carbon nanotubes (SWNTs) previously in our lab with the aid of surfactants.[1,2] We believe this is possibly because it takes a larger volume of surfactant solution to individually disperse the VGCFs or the MWNTs, than it takes to disperse SWNTs. This higher volume of surfactant solution contains more micelles; as noted in previous chapters, during deposition, there is a competition of the metal compounds to deposit either around micelles in solution or to deposit on the surfacted VGCFs/MWNTs. From our observations, it seems that in the case of surfacted VGCFs and MWNTs, it is more favorable for the metal compounds to deposit around the micelles in solution, forming a composite or homogeneous growth around the VGCFs and fibers.

A second overall conclusion that can be drawn is the effect of time and concentration of reactants on the growth of $SiO_2$, $TiO_2$, PbS, and $Bi_2S_3$ around the carbon nanotubes (CNTs) in the absence of surfactants. An increase in either one of these variables can give a thicker, and in some cases a more colloidal growth around the CNT.

Therefore, in order to get a coating type and thickness of choice, the variable of time and reactant concentration can be tweaked.

Finally, for any coatings to take place along the CNT, it is important for some nucleating sites to be present. In each case of $SiO_2$, PbS, and $Bi_2S_3$, the nitric acid treatment formed hydroxyl groups on the surface of the VGCFs, which helped in nucleation and growth. In the case of $TiO_2$, while there was no pretreatment done on the SWNTs, the initial nucleation occurred due to sidewall defects present on the SWNT allowing for nucleation to take place. Therefore the presence of nucleating sites is an important factor in the type of growth that occurs on the CNTs.

## References

1. E. A Whitsitt and A. R. Barron, *Nano Lett.,* 2003, **3**, 775.

2. R. Loscutova and A. R. Barron. *J. Mater. Chem.*, 2005, **15**, 4346.

## Appendix A

## List of Publications

1. Silica coated vapor grown carbon fibers. H. R. Jafry, E. A. Whitsitt, and A. R. Barron, *J. Mater. Sci.*, 2007, **42**, 7381.
2. Effect of functionalozed nanomaterials on the rheology of borate cross-linked guar gum. H. R. Jafry, M. P. Pasquali, and A. R. Barron, *Ind. Eng. Chem. Res.*, 2010, submitted.
3. A simple route to enhanced photocatalytic activity of P25 titanium dioxide nanoparticles by silica addition. H. R. Jafry, M. V. Liga, Q. Li, and A. R. Barron, *Environ. Sci. Technol.*, 2010, in press.
4. Single Walled Carbon Nanotubes (SWNTs) as templates for the growth of $TiO_2$: the effect of silicon in coverage and the positive and negative synergies for the photocatalytic degradation of Congo red dye. H. R. Jafry, M. V. Liga, Q. Li, and A. R. Barron, *New J. Chem.*, 2010, in press.